Title	Evaluation of the frequency dependence of the complex conductivity of a resistive chamber by comparing theoretical and measured S-matrices
Author(s)	Shobuda Yoshihiro
Citation	Progress of Theoretical and Experimental Physics,2018(12),p. 123G01_1 - 123G01_52
Text Version	Published Journal Article
URL	https://jopss.jaea.go.jp/search/servlet/search?5064058
DOI	https://doi.org/10.1093/ptep/pty124
Right	© The Author(s) 2018. Published by Oxford University Press on behalf of the Physical Society of Japan.This is an Open Access article distributed under the terms of the Creative Commons Attribution License (http://creativecommons.org/licenses/by/4.0/), which permits unrestricted reuse, distribution, and reproduction in any medium, provided the original work is properly cited.

PTEP

Prog. Theor. Exp. Phys. **2018**, 123G01 (52 pages)
DOI: 10.1093/ptep/pty124

Evaluation of the frequency dependence of the complex conductivity of a resistive chamber by comparing theoretical and measured *S*-matrices

Yoshihiro Shobuda*

J-PARC Center, JAEA&KEK, 2-4 Shirakata, Tokaimura, Nakagun, Ibaraki 319-1195, Japan
*E-mail: yoshihiro.shobuda@j-parc.jp

Received July 9, 2018; Revised October 18, 2018; Accepted October 25, 2018; Published December 28, 2018

For an accurate calculation of the resistive-wall impedance of a resistive chamber, we must know the conductivity of the resistive material. The conductivity of the material at a given frequency can be evaluated by measuring the *S*-matrix of a propagation mode in a waveguide. However, in most cases, only the absolute value of the *S*-matrix is used for evaluation under the assumption that the conductivity is pure real, although both the *S*-matrix and the conductivity are complex numbers in general. To evaluate complex conductivity from a measured complex *S*-matrix, we derive new theoretical formulae for the *S*-matrix for the TE_{11} and TM_{01} modes of a waveguide and for the quasi-TEM_{00} (quasi-transverse electromagnetic) mode of a coaxial waveguide, where complex conductivity is assumed. In a reverse way, we can determine the conductivity of a material by using it as a fitting parameter in a comparison of a measured *S*-matrix with those obtained using theoretical formulae. The three independent methods facilitate triple-checking of the accuracy of the measured conductivity.

Subject Index G12

1. Introduction

In recent years, non-evaporable getter (NEG) coatings on vacuum chambers have been successfully used to achieve ultra-high vacuum in many accelerators such as CERN LHC and ESRF [1,2]. One drawback of the NEG coating is its effect on resistive-wall impedance [3]. An NEG coating comprises a TiZrV ternary alloy (such as 30% titanium, 30% zirconium, and 40% vanadium) and its resistivity is typically higher than that of the chamber material by a factor of ~ 50. If a large proportion of the beam chamber surface is coated with NEG, it may increase the resistive-wall impedance of the machine significantly [4]. In synchrotron light sources [5,6], the bunch length varies from less than 1 mm to a few cm and we need to investigate the behavior of impedance over a wide range of frequencies, even beyond 1 THz.

For accurately estimating the resistive-wall impedance of a resistive waveguide, we must determine the conductivity of the resistive material and its frequency dependence. A common method to evaluate the frequency dependence of conductivity involves measuring the scattering matrices of a waveguide mode at various frequencies and comparing their absolute values with simulation results, assuming that the conductivity is pure real (called the "waveguide method" hereinafter) [7,8]. However, since conductivity is generally complex at high frequencies, we must use the complex scattering matrix.

Another measurement method to determine the complex dielectric constant (conductivity) is measuring the propagation constant of TE_{10} mode in rectangular waveguides [9]. The measured scattering matrix is converted to a diagonal T-matrix by implicitly assuming that the characteristic impedance of cables connected to the waveguide is identical to that of the waveguide.

Consequently, new theoretical formulae are necessary to fill in the blanks between the complex conductivity and the scattering matrix by solving the Maxwell equations for both transverse electric (TE) and transverse magnetic (TM) modes.

In Sect. 2, we present formulae for computing the scattering matrix for the TE and TM modes in the waveguide method measurement setup. Once the scattering matrices of the TE and TM modes are measured at various frequencies using this setup, we can evaluate the frequency dependence of conductivity by using it as a fitting parameter so that the theoretical and measured scattering matrices agree with each other.

The frequency dependence of conductivity can also be evaluated by measuring the scattering matrix of a quasi-transverse electromagnetic (quasi-TEM) mode in a coaxial waveguide (called the "wire method" hereinafter) [10]. In the wire method, a single wire is stretched out at the center of the resistive chamber sandwiched by two perfectly conductive chambers (mostly made of aluminum) at both ends. Recently, the authors have developed a general theory to calculate the beam coupling impedance of a ceramic break [11], sandwiched by two perfectly conductive chambers at both ends. In Sect. 3, we present a rigorous theoretical formula for determining the scattering matrix of the quasi-TEM mode with the wire method by generalizing this theory. This method can serve as an extra layer of checking on the accuracy of the conductivity obtained using the waveguide method.

The wire method is often used to estimate the resistive-wall beam coupling impedances from scattering matrices using the standard log-formula [12]. The question is how accurately the method can reproduce the resistive-wall impedance of a beam (called the "resistive-wall beam impedance" hereinafter) [13]. Many theories, including ours, are available for analytical calculation of the resistive-wall beam impedance [4,14–27]. In Sect. 4, we compare the theoretical resistive-wall beam impedance with the value obtained using the wire method by applying the standard log-formula to simulated scattering matrices.

In Sect. 5, we discuss some intrinsic errors of the measurement setup of the wire method, and the effects on the measurements at high frequency. The paper is concluded in Sect. 6.

2. Formulae for determining the scattering matrix using the waveguide method

Let us consider a 2D cylindrical chamber made of a resistive material with conductivity σ_c, whose inner and outer radii are d and a, respectively. We adopt cylindrical coordinates (ρ, θ, z) for this description. In this section, we present formulae for determining the scattering matrix of the waveguide modes. To ensure that the derived formulae reproduce the conventional formulae at the infinitesimal σ_c extreme [28], we assume that the outer surface of the resistive chamber is surrounded by a perfectly conductive layer. This approximation is valid in the frequency region in which the skin depth is smaller than the chamber width $(a - d)$. In the following formulation, we assume that all fields are proportional to $e^{j\omega t - j\Gamma z}$, where j is the imaginary unit and ω is the angular frequency. The parameter Γ depends on the waveguide mode (TE or TM).

2.1. Scattering matrix for the TE_{11} mode in a cylindrical waveguide

In this subsection, we present new formulae for determining the scattering matrix $((S_{11}, S_{12}), (S_{21}, S_{22}))$ for the TE_{11} mode, including the conductivity of the resistive material.

Derivations of the following formulae are given in Appendix A.1. They are expressed as follows:

$$S_{11} = S_{22} = \frac{\frac{1}{Z_{50}^2} - \frac{1}{Z_{\mathrm{TE}_{1,1}}^2}}{\frac{1}{Z_{50}^2} + \frac{1}{Z_{\mathrm{TE}_{1,1}}^2} + \frac{2}{jZ_{50}Z_{\mathrm{TE}_{1,1}} \tan \Gamma_{1,1}^{\mathrm{TE}} g}}, \tag{1}$$

and

$$S_{21} = S_{12} = \frac{\frac{2}{jZ_{50}Z_{\mathrm{TE}_{1,1}} \sin \Gamma_{1,1}^{\mathrm{TE}} g}}{\frac{1}{Z_{50}^2} + \frac{1}{Z_{\mathrm{TE}_{1,1}}^2} + \frac{2}{jZ_{50}Z_{\mathrm{TE}_{1,1}} \tan \Gamma_{1,1}^{\mathrm{TE}} g}}, \tag{2}$$

where the waveguide impedance is

$$Z_{\mathrm{TE}_{1,1}} = \frac{\omega Z_0}{c\Gamma_{1,1}^{\mathrm{TE}}}, \tag{3}$$

c is the velocity of light, $Z_0 = 120\pi\ \Omega$ is the impedance of free space, g is the total length of the waveguide chamber, and both ends of the waveguide are connected to cables with the characteristic impedance Z_{50} (which is typically 50 Ω). The factor $\Gamma_{1,1}^{\mathrm{TE}}$ is the first non-trivial solution of

$$\frac{[I_1(\kappa d) - \frac{I_1'(\kappa a)}{K_1'(\kappa a)} K_1(\kappa d)] J_1'(\Lambda d)}{\sqrt{\frac{\omega^2}{c^2} - \Gamma^2}} + \frac{1}{\kappa}\left[I_1'(\kappa d) - \frac{I_1'(\kappa a)}{K_1'(\kappa a)} K_1'(\kappa d)\right] J_1(\Lambda d) = 0, \tag{4}$$

for a given frequency, where

$$\kappa = \sqrt{\Gamma^2 - \frac{\omega^2}{c^2} + j\omega\mu_0\sigma_c}, \tag{5}$$

$$\Lambda = \sqrt{\frac{\omega^2}{c^2} - \Gamma^2}, \tag{6}$$

and μ_0 is the permeability of vacuum. The functions $J_n(z)$ and $I_n(z)$, $K_n(z)$ are the Bessel and modified Bessel functions, respectively [29]. The prime of the functions denotes the differential with respect to their arguments.

Especially when $\sigma_c = 0$ S/m, Eq. (4) reproduces the conventional eigenvalue condition:

$$J_1'(\Lambda a) = 0, \tag{7}$$

which is equivalent to

$$\Gamma_{n,1} = \sqrt{\frac{\omega^2}{c^2} - \frac{j_{1,n}'^2}{a^2}}, \tag{8}$$

which describes the eigenmode of a purely perfectly conductive waveguide chamber with the inner radius a [28]. Here $j_{1,n}'$ is the nth zero of $J_1'(z)$.

Note that formulae (1) and (2) are general and can reproduce the conventional formulae for the scattering matrix of a perfectly conductive material, i.e., $\sigma_c = 0$ S/m, because Γ is identical to Eq. (8) in that case. It should be noted that Eq. (3) is identical to the conventional definition of waveguide

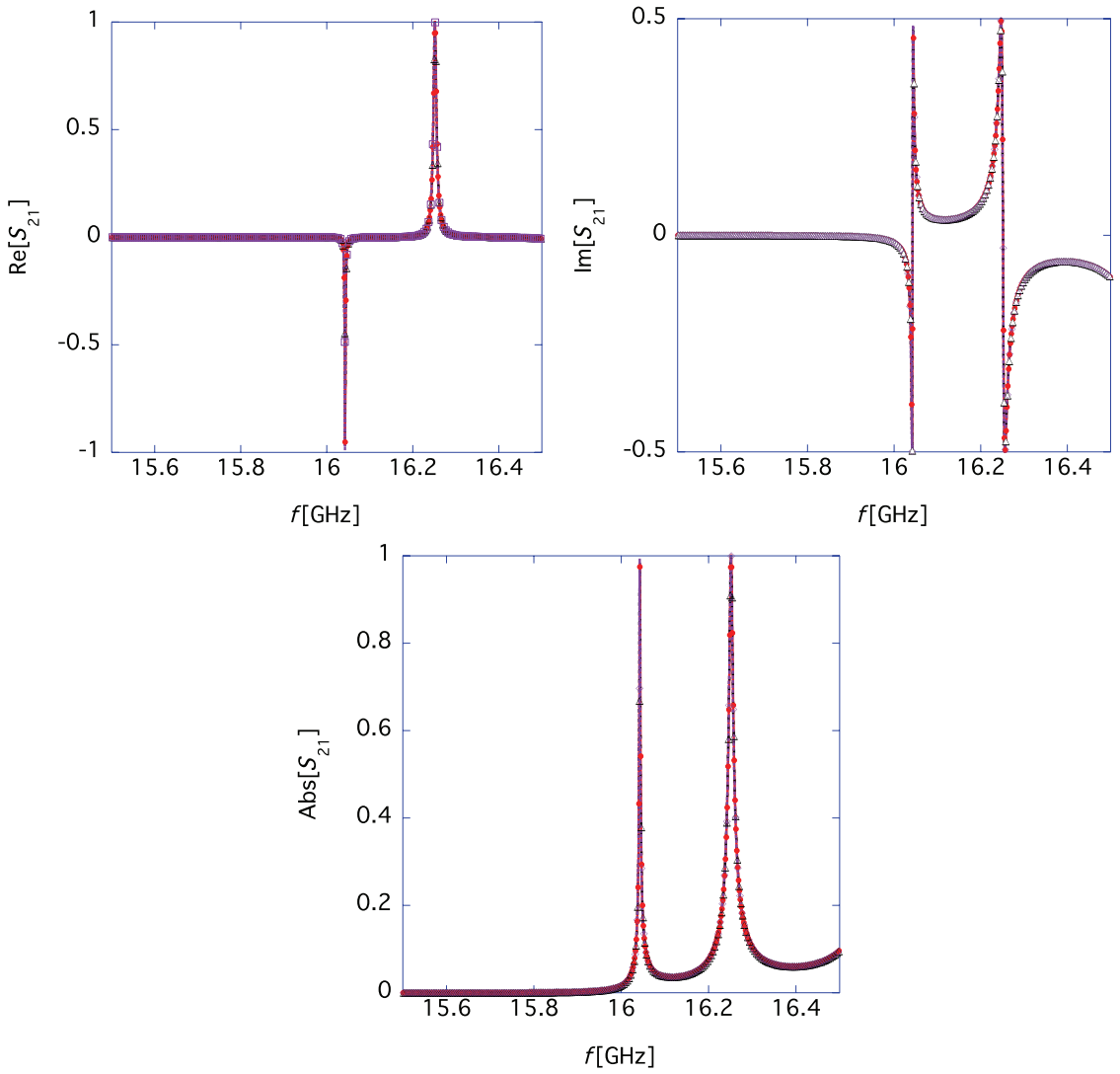

Fig. 1. Dependence of S_{21} on mesh number N_{mesh} from 15.5 GHz to 16.5 GHz for a chamber with $\sigma_c = 0$ S/m, $g = 100$ mm, $a = 5.5$ mm, and $d = 4.5$ mm, which is surrounded by a perfectly conductive layer. The upper-left, upper-right, and lower-left panels show the real part, imaginary part, and absolute value of S_{21}, respectively. The red •, black △, and purple □ lines represent the results for $N_{\mathrm{mesh}} = 25\,000$, 27 000, and 34 000, respectively.

impedance in the $\mathrm{TE}_{1,1}$ mode [28], when the waveguide is made solely of a perfectly conductive material.

Next, let us compare the theoretical results of S_{21} with the simulated ones for cases of $\sigma_c = 0$ S/m and $\sigma_c = 0.1$ S/m. We assume that the chamber length g is 100 mm long. The simulations are performed using the frequency domain solver (F-Solver) of Microwave-Studio in CST Studio Suite 2018 [30], where the resistive waveguide is sandwiched between two waveguide ports at both ends. The time domain solver (T-Solver) of Microwave-Studio cannot calculate the scattering matrix of a waveguide made of resistive material. T-Solver is applicable only to a perfectly conductive waveguide in the case of the waveguide method.

The mesh-number N_{mesh} dependence of simulated S_{21} is shown in Fig. 1, which represents the results for $\sigma_c = 0$ S/m, $g = 100$ mm, $a = 5.5$ mm, and $d = 4.5$ mm. The upper-left, upper-right, and

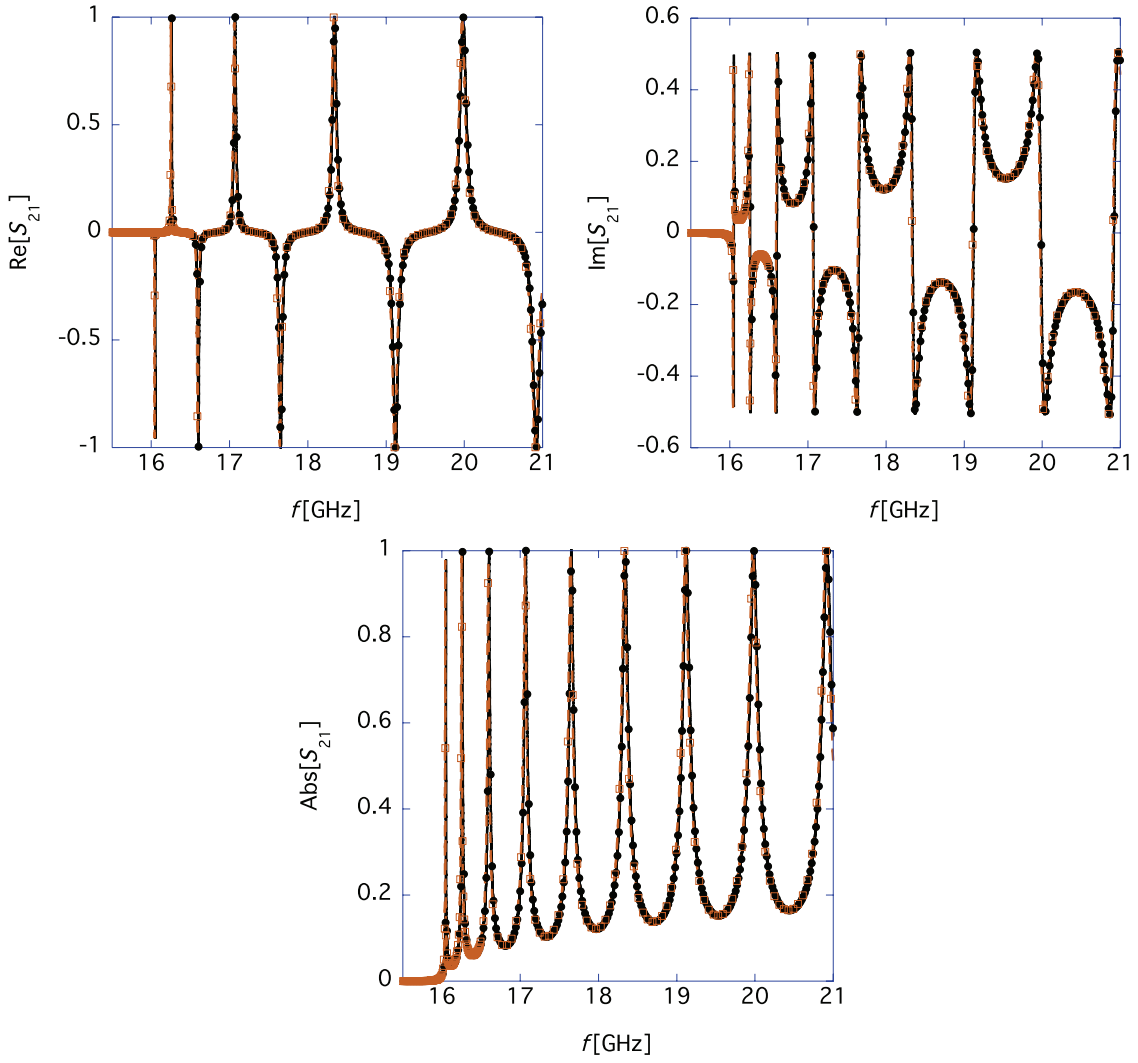

Fig. 2. Theoretical (black •) and simulation (brown □) results of S_{21} for $\sigma_c = 0$ S/m, $g = 100$ mm, $a = 5.5$ mm, and $d = 4.5$ mm (this is the case of a perfectly conductive chamber with an inner radius of 5.5 mm.). The upper-left, upper-right, and lower-left panels show the real part, imaginary part, and absolute value of S_{21}, respectively.

lower-left panels show the real part, imaginary part, and absolute value of the scattering matrices, respectively. The red •, black △, and purple □ lines in Fig. 1 show the results for $N_{\text{mesh}} = 25\,000$, 27 000, and 34 000, respectively. They demonstrate that the simulation results are saturated with these mesh numbers. In all CST calculations of this paper, we checked the convergence of the results in this way.

First, let us compare the theoretical results (obtained using formulae (1) and (2)) with the simulated ones for $\sigma_c = 0$ S/m. Their agreement should be perfect, because this is the simple perfectly conductive waveguide case [28]. Figure 2 shows the theoretical S_{21} matrices (black •) and the simulated ones (brown □). They are indeed in good agreement.

Next, let us compare the theoretical S_{21} matrices with the simulated ones for a finitely conductive waveguide with $\sigma_c = 0.1$ S/m. This highly resistive case provides a test to check whether simulations can reproduce the theoretical values when physical phenomena (such as skin depth effects) inside the waveguide can be accurately expressed using a sufficiently small mesh size. The results are

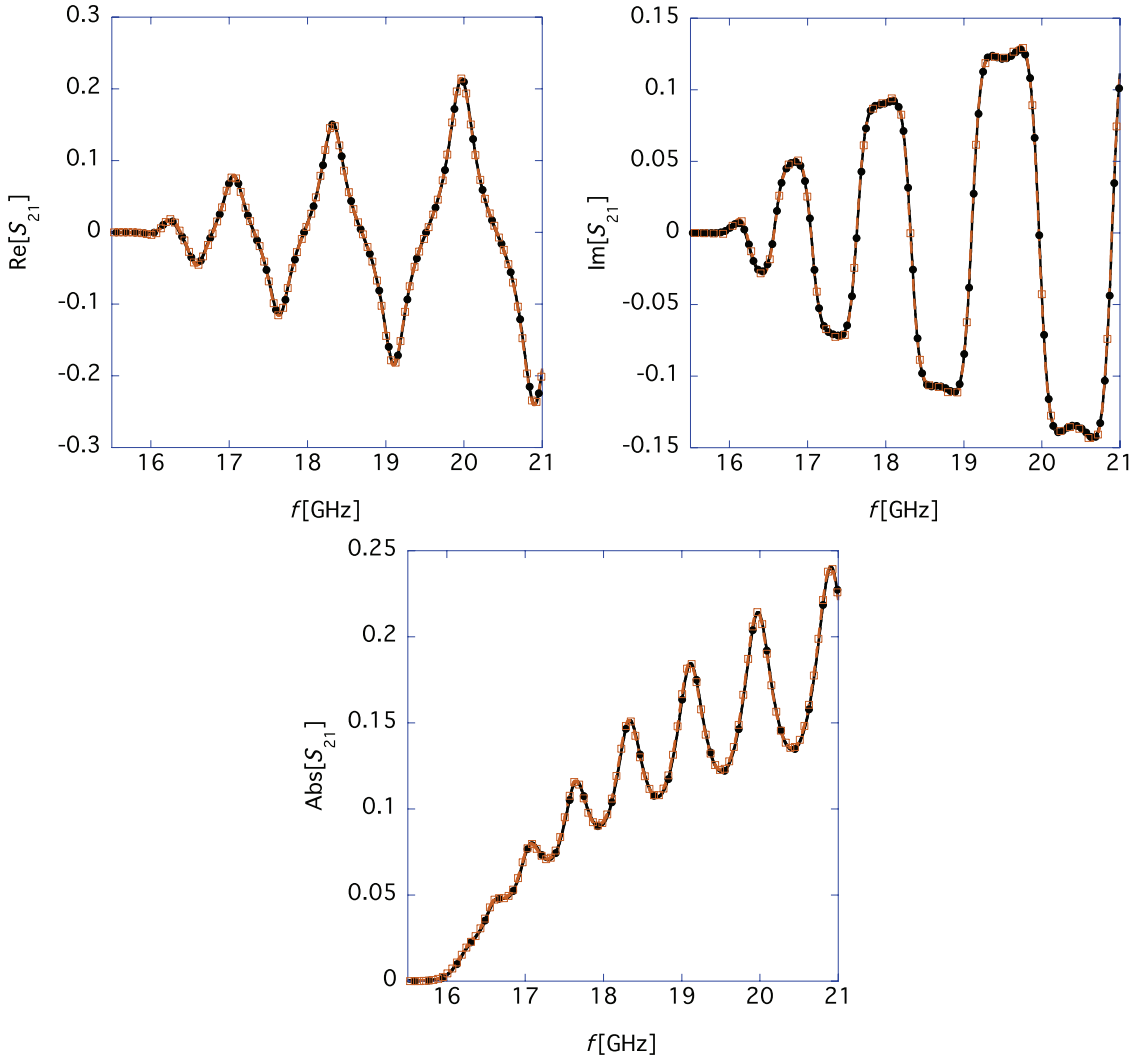

Fig. 3. Theoretical (black •) and simulation (brown □) results of S_{21} for $\sigma_c = 0.1$ S/m, $g = 100$ mm, $a = 5.5$ mm, and $d = 4.5$ mm. The upper-left, upper-right, and lower-left panels show the real part, imaginary part, and absolute value of S_{21}, respectively.

shown in Fig. 3, where the black • and brown □ lines denote the theoretical and simulation results, respectively. They are in good agreement again. Now the validity of the generalized theoretical formulae (1) and (2) for the TE_{11} mode based on the waveguide method has been proved for two different conductivities.

2.2. *Scattering matrix for the TM_{01} mode by the waveguide method*

In this subsection, we present new formulae for determining the scattering matrix $((S_{11}, S_{12}), (S_{21}, S_{22}))$ for the TM_{01} mode, including the conductivity σ_c of the resistive material. The derivation of the following formulae is described in Appendix A.2. They are expressed as follows:

$$S_{11} = S_{22} = \frac{\left(\frac{1}{Z_{50}^2} - \frac{C_I^2}{C_V^2}\right)}{\frac{1}{Z_{50}^2} + \frac{C_I^2}{C_V^2} + \frac{2C_I}{C_V Z_{50} j \tan \Gamma_{1,0}^{TM} g}}, \tag{9}$$

and

$$S_{21} = S_{12} = \frac{\frac{2C_I}{C_V Z_{50} j \sin \Gamma_{1,0}^{\mathrm{TM}} g}}{\frac{1}{Z_{50}^2} + \frac{C_I^2}{C_V^2} + \frac{2C_I}{C_V Z_{50} j \tan \Gamma_{1,0}^{\mathrm{TM}} g}}, \tag{10}$$

where $\Gamma_{1,0}^{\mathrm{TM}}$ is the lowest root of

$$\frac{\omega\epsilon_0[I_0(\kappa d) - \frac{I_0(\kappa a)}{K_0(\kappa a)}K_0(\kappa d)]J_1(\Lambda d)}{j\Lambda} + \frac{(\sigma_c + j\omega\epsilon_0)J_0(\Lambda d)[I_1(\kappa d) + \frac{I_0(\kappa a)}{K_0(\kappa a)}K_1(\kappa d)]}{\sqrt{\Gamma^2 - \frac{\omega^2}{c^2} + j\omega\mu_0\sigma_c}} = 0, \tag{11}$$

with Eqs. (5) and (6):

$$\begin{aligned}
Z_c' = \frac{2j_{0,1}^2 c^2 Z_0^2}{\omega \Gamma_{1,0}^{\mathrm{TM}} a^4 J_1^2(j_{0,1})} \Bigg\{ & -\frac{\Im[\Lambda_{\mathrm{TM}} d J_0(\Lambda_{\mathrm{TM}}^* d) J_1(\Lambda_{\mathrm{TM}} d)]}{c Z_0 \Im[\Lambda_{\mathrm{TM}}^2]} + \frac{\omega^2 \Im[\Lambda_{\mathrm{TM}}^* d J_0(\Lambda_{\mathrm{TM}}^* d) J_1(\Lambda_{\mathrm{TM}} d)]}{c^3 Z_0 |\Lambda_{\mathrm{TM}}|^2 \Im[\Lambda_{\mathrm{TM}}^2]} \\
& - \left(\epsilon_0 + \frac{j\sigma_c^*}{\omega}\right) \frac{|J_0(\Lambda_{\mathrm{TM}} d)|^2}{|I_0(\kappa_{1,0} d) - \frac{I_0(\kappa_{1,0} a)}{K_0(\kappa_{1,0} a)} K_0(\kappa_{1,0} d)|^2} \\
& \times \Bigg\{ \frac{\Im[\kappa_{1,0} a I_0(\kappa_{1,0}^* a) I_1(\kappa_{1,0} a) - \kappa_{1,0} d I_0(\kappa_{1,0}^* d) I_1(\kappa_{1,0} d)]}{\Im[\kappa_{1,0}^2]} \\
& -2\Re\left[\frac{I_0(\kappa_{1,0} a)}{K_0(\kappa_{1,0} a)}\left(-\frac{a(\kappa_{1,0}^* I_1(\kappa_{1,0}^* a) K_0(\kappa_{1,0} a) + \kappa_{1,0} I_0(\kappa_{1,0}^* a) K_1(\kappa_{1,0} a))}{(\kappa_{1,0}^2 - \kappa_{1,0}^{*2})}\right.\right. \\
& \left.\left. + \frac{d(\kappa_{1,0}^* I_1(\kappa_{1,0}^* d) K_0(\kappa_{1,0} d) + \kappa_{1,0} I_0(\kappa_{1,0}^* d) K_1(\kappa_{1,0} d))}{(\kappa_{1,0}^2 - \kappa_{1,0}^{*2})}\right)\right] \\
& - \frac{|I_0(\kappa_{1,0} a)|^2 \Im[\kappa_{1,0}(a K_0(\kappa_{1,0}^* a) K_1(\kappa_{1,0} a) - d K_0(\kappa_{1,0}^* d) K_1(\kappa_{1,0} d))]}{|K_0(\kappa_{1,0} a)|^2 \Im[\kappa_{1,0}^2]} \Bigg\} \\
& + \frac{\omega^2 |J_1(\Lambda_{\mathrm{TM}} d)|^2}{c^3 Z_0 |\Lambda_{\mathrm{TM}}|^2 |I_1(\kappa_{1,0} d) + \frac{I_0(\kappa_{1,0} a)}{K_0(\kappa_{1,0} a)} K_1(\kappa_{1,0} d)|^2} \\
& \times \Bigg\{ \frac{\Im[\kappa_{1,0} a I_1(\kappa_{1,0}^* a) I_2(\kappa_{1,0} a) - \kappa_{1,0} d I_1(\kappa_{1,0}^* d) I_2(\kappa_{1,0} d)]}{\Im[\kappa_{1,0}^2]} \\
& +2\Re\left[\frac{I_0(\kappa_{1,0} a)}{K_0(\kappa_{1,0} a)}\left(-\frac{a(\kappa_{1,0}^* I_2(\kappa_{1,0}^* a) K_1(\kappa_{1,0} a) + \kappa_{1,0} I_1(\kappa_{1,0}^* a) K_2(\kappa_{1,0} a))}{(\kappa_{1,0}^2 - \kappa_{1,0}^{*2})}\right.\right. \\
& \left.\left. + \frac{d(\kappa_{1,0}^* I_2(\kappa_{1,0}^* d) K_1(\kappa_{1,0} d) + \kappa_{1,0} I_1(\kappa_{1,0}^* d) K_2(\kappa_{1,0} d))}{(\kappa_{1,0}^2 - \kappa_{1,0}^{*2})}\right)\right] \\
& + \frac{|I_0(\kappa_{1,0} a)|^2 \Im[\kappa_{1,0}^*(a K_0(\kappa_{1,0}^* a) K_1(\kappa_{1,0} a) - d K_0(\kappa_{1,0}^* d) K_1(\kappa_{1,0} d))]}{|K_0(\kappa_{1,0} a)|^2 \Im[\kappa_{1,0}^2]} \Bigg\} \Bigg\},
\end{aligned} \tag{12}$$

$$
\begin{aligned}
C_I = \frac{2j_{0,1}^2\tilde{B}}{\omega\Gamma_{1,0}^{\mathrm{TM}*}Z_c'^{*}a^4J_1^2(j_{0,1})}\Bigg\{ & -\frac{cZ_0(\Im[\Lambda_{\mathrm{TM}}dJ_0(\Lambda_{\mathrm{TM}}^*d)J_1(\Lambda_{\mathrm{TM}}d)] - \frac{\omega^2\Im[\Lambda_{\mathrm{TM}}^*dJ_0(\Lambda_{\mathrm{TM}}^*d)J_1(\Lambda_{\mathrm{TM}}d)]}{c^2|\Lambda_{\mathrm{TM}}|^2})}{\Im[\Lambda_{\mathrm{TM}}^2]} \\
& - \frac{|J_1(\Lambda_{\mathrm{TM}}d)|^2}{(\epsilon_0 - \frac{\sigma_c^*}{j\omega})|I_1(\kappa_{1,0}d) + \frac{I_0(\kappa_{1,0}a)}{K_0(\kappa_{1,0}a)}K_1(\kappa_{1,0}d)|^2} \\
& \times \Bigg(\frac{\Im[\kappa_{1,0}aI_0(\kappa_{1,0}^*a)I_1(\kappa_{1,0}a) - \kappa_{1,0}dI_0(\kappa_{1,0}^*d)I_1(\kappa_{1,0}d)]}{\Im[\kappa_{1,0}^2]} \\
& - 2\Re\Bigg[\frac{\frac{I_0(\kappa_{1,0}^*a)}{K_0(\kappa_{1,0}^*a)}(\kappa_{1,0}aI_1(\kappa_{1,0}a)K_0(\kappa_{1,0}^*a) + \kappa_{1,0}^*aI_0(\kappa_{1,0}a)K_1(\kappa_{1,0}^*a))}{(\kappa_{1,0}^2 - \kappa_{1,0}^{*2})} \\
& - \frac{\frac{I_0(\kappa_{1,0}^*a)}{K_0(\kappa_{1,0}^*a)}(\kappa_{1,0}dI_1(\kappa_{1,0}d)K_0(\kappa_{1,0}^*d) + \kappa_{1,0}^*dI_0(\kappa_{1,0}d)K_1(\kappa_{1,0}^*d))}{(\kappa_{1,0}^2 - \kappa_{1,0}^{*2})}\Bigg] \\
& - \frac{|I_0(\kappa_{1,0}a)|^2\Im[\kappa_{1,0}aK_0(\kappa_{1,0}^*a)K_1(\kappa_{1,0}a) - \kappa_{1,0}dK_0(\kappa_{1,0}^*d)K_1(\kappa_{1,0}d)]}{|K_0(\kappa_{1,0}a)|^2\Im[\kappa_{1,0}^2]}\Bigg) \\
& + \frac{\omega^2Z_0|J_1(\Lambda_{\mathrm{TM}}d)|^2}{c|\Lambda_{\mathrm{TM}}|^2|I_1(\kappa_{1,0}d) + \frac{I_0(\kappa_{1,0}a)}{K_0(\kappa_{1,0}a)}K_1(\kappa_{1,0}d)|^2} \\
& \times \Bigg(\frac{\Im[\kappa_{1,0}aI_1(\kappa_{1,0}^*a)I_2(\kappa_{1,0}a) - \kappa_{1,0}dI_1(\kappa_{1,0}^*d)I_2(\kappa_{1,0}d)]}{\Im[\kappa_{1,0}^2]} \\
& + 2\Re\Bigg[\frac{\frac{I_0(\kappa_{1,0}^*a)}{K_0(\kappa_{1,0}^*a)}(\kappa_{1,0}aI_2(\kappa_{1,0}a)K_1(\kappa_{1,0}^*a) + \kappa_{1,0}^*aI_1(\kappa_{1,0}a)K_2(\kappa_{1,0}^*a))}{(\kappa_{1,0}^2 - \kappa_{1,0}^{*2})} \\
& - \frac{\frac{I_0(\kappa_{1,0}^*a)}{K_0(\kappa_{1,0}^*a)}(\kappa_{1,0}dI_2(\kappa_{1,0}d)K_1(\kappa_{1,0}^*d) + \kappa_{1,0}^*dI_1(\kappa_{1,0}d)K_2(\kappa_{1,0}^*d))}{(\kappa_{1,0}^2 - \kappa_{1,0}^{*2})}\Bigg] \\
& + \frac{|I_0(\kappa_{1,0}a)|^2\Im[\kappa_{1,0}^*(aK_0(\kappa_{1,0}^*a)K_1(\kappa_{1,0}a) - dK_0(\kappa_{1,0}^*d)K_1(\kappa_{1,0}d)])}{|K_0(\kappa_{1,0}a)|^2\Im[\kappa_{1,0}^2]}\Bigg)\Bigg\}, \qquad (13)
\end{aligned}
$$

$$
\begin{aligned}
C_V = & \tilde{B}\frac{2j_{0,1}^2|\Gamma_{1,0}^{\mathrm{TM}}|^2}{a^4J_1^2(j_{0,1})\Gamma_{1,0}^{*TM}|\Lambda_{\mathrm{TM}}|^2}\Bigg[\frac{cZ_0\Im[\Lambda_{\mathrm{TM}}^*dJ_0(\Lambda_{\mathrm{TM}}^*d)J_1(\Lambda_{\mathrm{TM}}d)]}{\omega\Im[\Lambda_{\mathrm{TM}}^2]} \\
& + \frac{\omega(\epsilon_0 - \frac{\sigma_c^*}{j\omega})|J_1(\Lambda_{\mathrm{TM}}d)|^2}{|\sigma_c + j\omega\epsilon_0|^2|I_1(\kappa_{1,0}d) + \frac{I_0(\kappa_{1,0}a)}{K_0(\kappa_{1,0}a)}K_1(\kappa_{1,0}d)|^2} \\
& \times \Bigg\{ \frac{\Im[\kappa_{1,0}aI_1(\kappa_{1,0}^*a)I_2(\kappa_{1,0}a) - \kappa_{1,0}dI_1(\kappa_{1,0}^*d)I_2(\kappa_{1,0}d)]}{\Im[\kappa_{1,0}^2]} \\
& - 2\Re\Bigg[\frac{a\frac{I_0(\kappa_{1,0}a)}{K_0(\kappa_{1,0}a)}(\kappa_{1,0}^*I_2(\kappa_{1,0}^*a)K_1(\kappa_{1,0}a) + \kappa_{1,0}I_1(\kappa_{1,0}^*a)K_2(\kappa_{1,0}a))}{(\kappa_{1,0}^2 - \kappa_{1,0}^{*2})}
\end{aligned}
$$

$$-\frac{d\frac{I_0(\kappa_{1,0}a)}{K_0(\kappa_{1,0}a)}(\kappa^*_{1,0}I_2(\kappa^*_{1,0}d)K_1(\kappa_{1,0}d)+\kappa_{1,0}I_1(\kappa^*_{1,0}d)K_2(\kappa_{1,0}d))}{(\kappa^2_{1,0}-\kappa^{*2}_{1,0})}\Bigg]$$

$$+\frac{|I_0(\kappa_{1,0}a)|^2\Im[\kappa^*_{1,0}(aK_0(\kappa^*_{1,0}a)K_1(\kappa_{1,0}a)-dK_0(\kappa^*_{1,0}d)K_1(\kappa_{1,0}d))]}{|K_0(\kappa_{1,0}a)|^2\Im[\kappa^2_{1,0}]}\Bigg\}\Bigg], \tag{14}$$

$$\kappa_{1,0}=\sqrt{(\Gamma^{\mathrm{TM}}_{1,0})^2-\frac{\omega^2}{c^2}+j\omega\mu_0\sigma_c}, \tag{15}$$

$$\Lambda_{\mathrm{TM}}=\left(\frac{\omega^2}{c^2}-(\Gamma^{\mathrm{TM}}_{1,0})^2\right)^{\frac{1}{2}}, \tag{16}$$

where ϵ_0 is the dielectric constant of vacuum, $j_{0,1}$ is the first zero of the Bessel function $J_0(z)$, $\tilde{B}$ is an arbitrary coefficient, and "*" denotes a complex conjugate.

Here, let us focus on the conventional case of the perfectly conductive waveguide, where the perfectly conductive wall exists only at $\rho = a$ in vacuum, i.e., $\sigma_c = 0$ S/m. In this case, Eqs. (12), (13), and (14) are simplified as

$$Z'_c=\frac{cZ_0\Gamma^1_{\mathrm{wall},a}}{\omega}, \tag{17}$$

$$C_I=\frac{cZ_0(\Gamma^1_{\mathrm{wall},a})^2\tilde{B}}{\omega\Gamma^{1*}_{\mathrm{wall},a}Z'^*_c}, \tag{18}$$

$$C_V=\tilde{B}\frac{cZ_0|\Gamma^1_{\mathrm{wall},a}|^2}{\omega\Gamma^{1*}_{\mathrm{wall},a}}, \tag{19}$$

where

$$\Gamma^1_{\mathrm{wall},a}=\sqrt{\frac{\omega^2}{c^2}-\frac{j^2_{0,1}}{a^2}}. \tag{20}$$

We can confirm that Eqs. (9) and (10) reproduce the conventional formulae for the scattering matrix because C_V/C_I becomes

$$\frac{C_V}{C_I}=\frac{cZ_0\Gamma^1_{\mathrm{wall},a}}{\omega}, \tag{21}$$

which is identical to the waveguide impedance of the TM_{01} mode for this case [28].

Now let us compare the theoretical S_{21} with the simulated ones for $\sigma_c = 0$ S/m and $\sigma_c = 0.1$ S/m, as done for the case of the TE_{11} mode. The longitudinal length of the waveguide, g, is 100 mm. The simulations were performed using the F-Solver module in Microwave-Studio. The simulated scattering matrix S_{21} is compared to the theoretical result.

In Fig. 4, the theoretical (black •) and simulation (brown □) results are compared for $\sigma_c = 0$ S/m, which corresponds to the conventional perfectly conductive chamber case [28]. The overall behaviors in the theoretical and simulation results are in good agreement.

Now let us move to the resistive waveguide case to investigate the accuracy of the theoretical formulae (Eqs. (9) and (10)) for the scattering matrix. Figure 5 compares the theoretical results

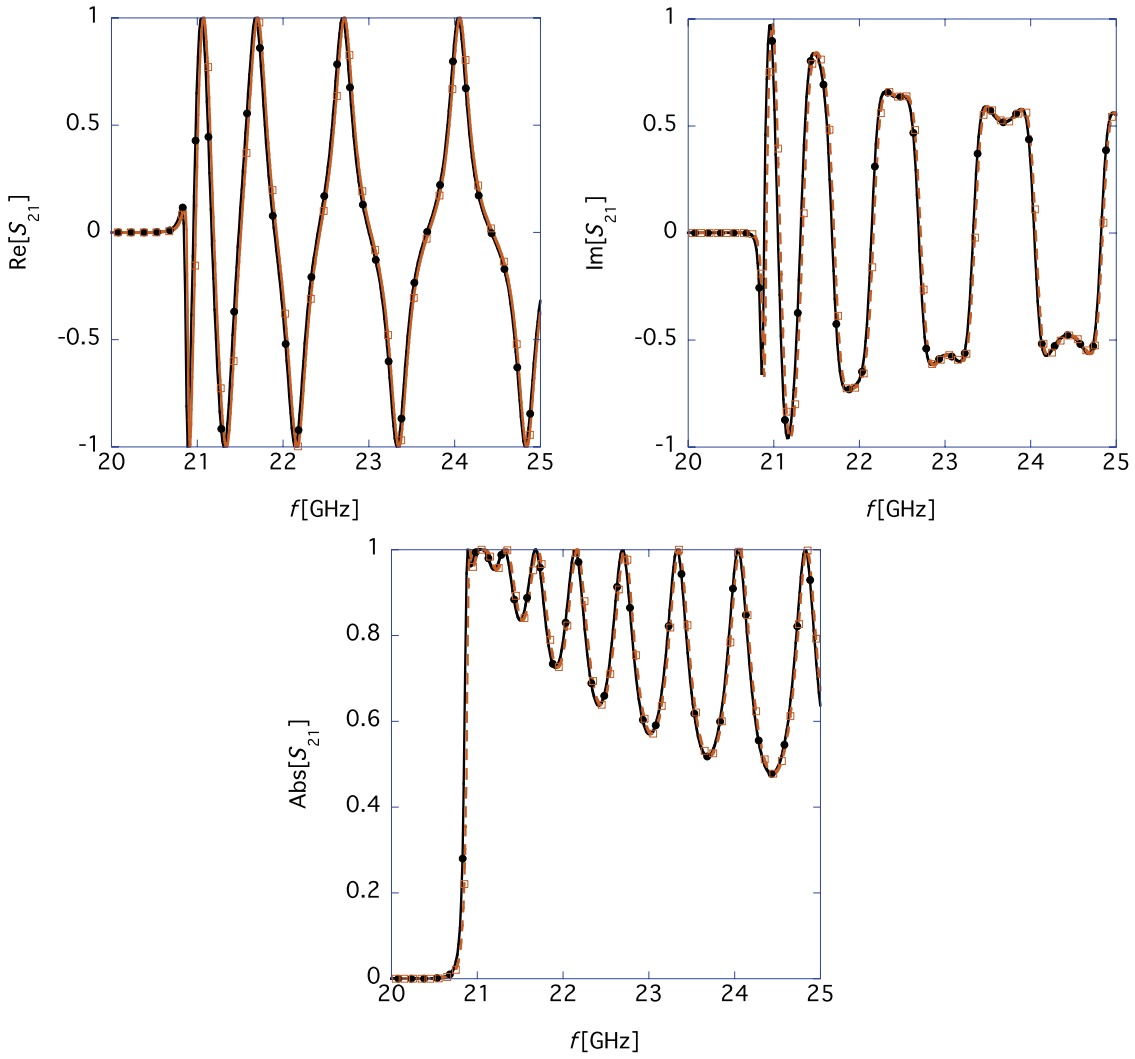

Fig. 4. Theoretical (black •) and simulation (brown □) results of S_{21} for $\sigma_c = 0$ S/m, $g = 100$ mm, $a = 5.5$ mm, and $d = 4.5$ mm. The upper-left, upper-right, and lower-left panels show the real part, imaginary part, and absolute value of S_{21}, respectively.

(black •) with the simulation results (brown □) for $\sigma_c = 0.1$ S/m. As in the TE_{11} mode case, we obtained good agreement between the theoretical results and the simulation results. This demonstrates the numerical validity of the theoretical formulae for determining the scattering matrix for the TM_{01} mode based on the waveguide method.

2.3. TE_{11} and TM_{01} modes in a cylindrical waveguide made of a material with complex conductivity

In this subsection, we examine a few examples of a cylindrical waveguide made of a resistive material with complex conductivity. In terms of the frequency dependence of conductivity, we consider the Drude model [31,32] as a somewhat realistic model:

$$\sigma_{\mathrm{D}}(\omega) = \frac{\sigma_0}{1 + j\omega\tau} = \epsilon_0 \frac{\omega_p^2}{\tau(\omega^2 + 1/\tau^2)} - j\epsilon_0 \frac{\omega\omega_p^2}{\omega^2 + 1/\tau^2}, \tag{22}$$

where $\sigma_0 = \omega_p^2 \tau \epsilon_0$ is DC conductivity, ω_p is plasma frequency, and τ is relaxation time.

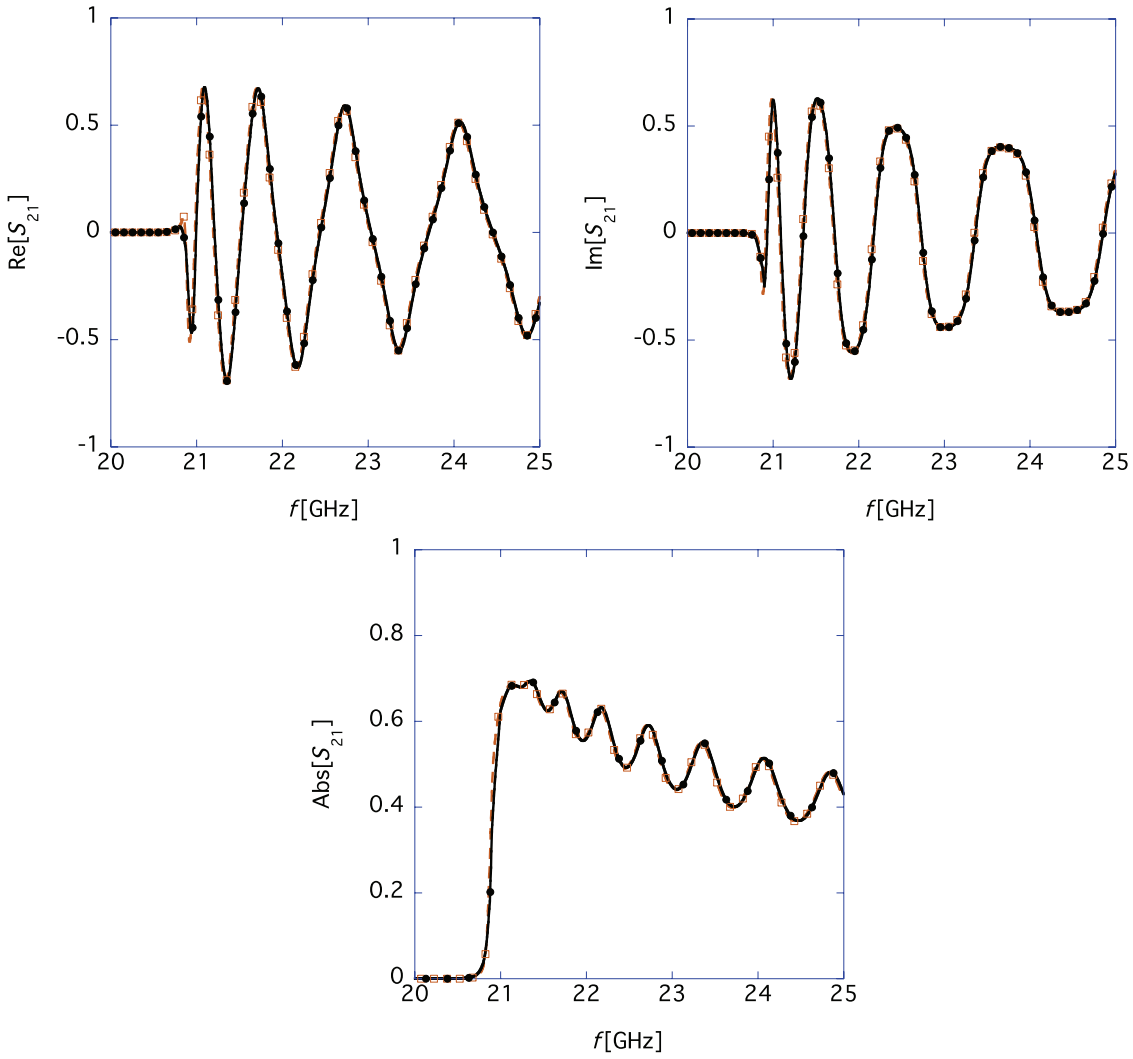

Fig. 5. Theoretical (black •) and simulation (brown □) results of S_{21} for $\sigma_c = 0.1$ S/m, $g = 100$ mm, $a = 5.5$ mm, and $d = 4.5$ mm. The upper-left, upper-right, and lower-left panels show the real part, imaginary part, and absolute value of S_{21}, respectively.

In CST Studio Suite 2018, the Drude model is implemented to cope with a resistive material of complex conductivity. We assume that the parameters are $\tau = 21.35$ ps, $\omega_p = 72.8$ THz, $d = 44$ μm, $a = 45$ μm, and $g = 300$ μm. They constitute the THz region of the scattering matrix in a resistive waveguide. It is noticeable that the inner diameter of the waveguide ($2d = 88$ μm) is around the same order of magnitude or less as the height (191 μm) of the rectangular waveguide utilized in the measurement of the conductivity of NEG at 500–750 GHz in Ref. [8].

Given that the skin depth decreases at high frequency, it is generally difficult to adopt a sufficiently small mesh size comparable to the skin depth in the THz region in simulations. However, if we set the waveguide radius d such that the cutoff frequency f_c,

$$f_c = \frac{cj'_{1,1}}{2\pi d} \sim \frac{cj_{01}}{2\pi d}, \tag{23}$$

becomes around 2 THz, the waveguide radius is around 50 μm. Because of the small dimension of the waveguide, the mesh size does not hinder the simulation study.

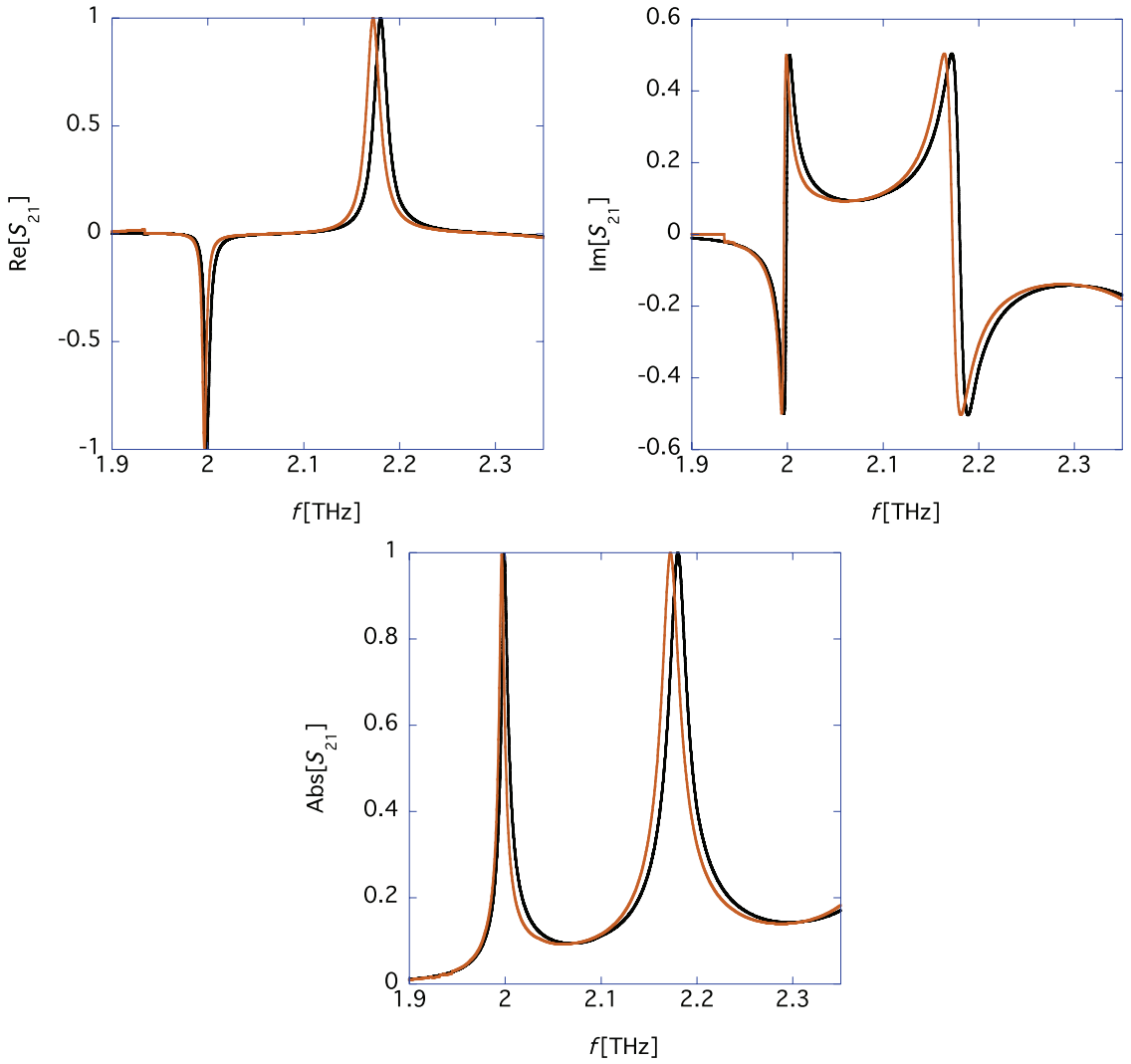

Fig. 6. Theoretical (black) and simulation (brown) results in $TE_{1,1}$ mode for σ_D (see Eq. (22)) with $\tau = 21.35$ ps, $\omega_p = 72.8$ THz, $d = 44$ μm, and $a = 45$ μm. The upper-left, upper-right, and lower-left panels represent the real part, imaginary part, and absolute value of S_{21}, respectively.

Let us simulate the scattering matrix for this small waveguide with complex conductivity. Figures 6 and 7 show the scattering matrices in the THz region for the TE_{11} and TM_{01} modes, respectively. The theoretical and simulation results with adequately large mesh numbers for convergence are shown by the black and brown lines, respectively. Figures 6 and 7 show a good agreement between the theoretical and simulation results for the TE_{11} and TM_{01} modes, respectively, in the case of the resistive waveguide with complex conductivity. This indicates that the theoretical formulae (Eqs. (1) and (2) for the TE_{11} mode, and Eqs. (9) and (10) for the TM_{01} mode) describe the frequency dependence of the conductivity of the scattering matrix sufficiently well. Although we are yet to find a cause for the slight difference between the theoretical and simulation results, the discrepancy will impose no significant accuracy problem in determining the frequency dependence of complex conductivity in measurements.

In the final part of this section, we briefly discuss how we can determine the frequency dependence of the material's conductivity σ_c from the measurement results. We obtained the analytical formulae

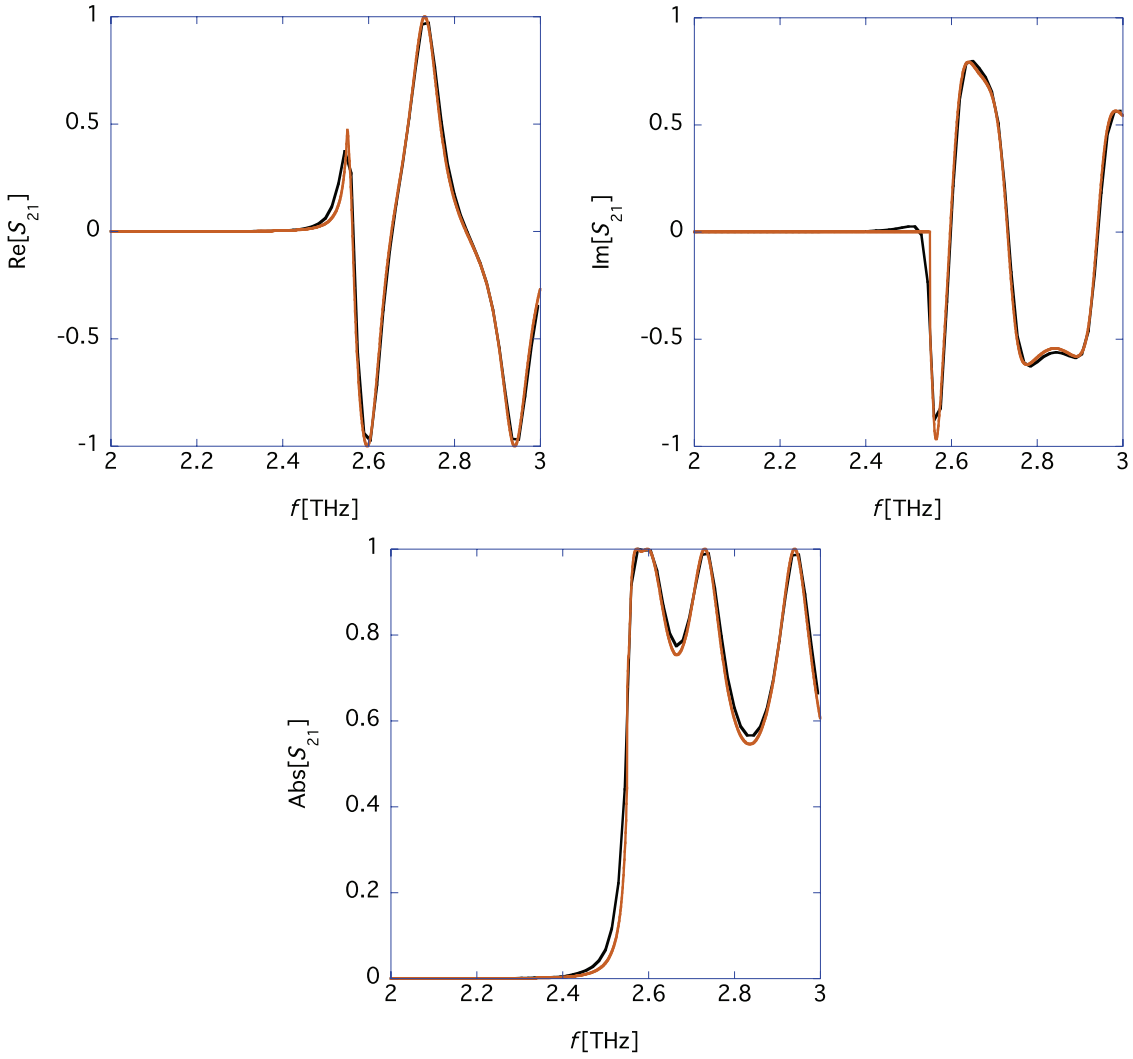

Fig. 7. Theoretical (black) and simulation (brown) results in $TM_{0,1}$ mode for σ_D (see Eq. (22)) with $\tau = 21.35$ ps, $\omega_p = 72.8$ THz, $d = 44$ μm, and $a = 45$ μm. The upper-left, upper-right, and lower-left panels represent the real part, imaginary part, and absolute value of S_{21}, respectively.

for the scattering matrices, Eqs. (1) and (2), in combination with Eqs. (3) and (4) for the TE_{11} mode, and Eqs. (9) and (10), in combination with Eqs. (11), (12), (13), and (14) for the TM_{01} mode. Given that both formulae reproduce the simulation results well, the conductivity dependence of the scattering matrix expressed in these formulae is proven.

The procedure is as follows.

(1) Measure S-matrices by using the waveguide method for either (both) the TE_{11} or (and) the TM_{01} mode(s) at various frequencies.
(2) Use the complex conductivity (real and imaginary parts) as a fitting parameter so that the theoretical complex S-matrix agrees with the measured one at each measured frequency point.

The complex dielectric constant (conductivity) has to respect the Kramers–Kronig relations, which associate their real part with the imaginary one. Then, unless we assume any analytical formula satisfying the relation in the fitting process of the conductivity, the application of the relation to

the measured data in a wide range of frequencies enables us to check the self-consistency of the observations.

It is noticeable that the roughness of the surfaces of the chambers can contribute to the scattering matrix as well, beyond frequencies of tens of GHz [8]. In this sense, the conductivity obtained by the fitting process is the zeroth-order approximation at the frequency. However, when the structure of the surface roughness is given, a simulation technique can eliminate the effect by calculating the response matrix for the variation of components of the scattering matrix to that of the complex conductivity. Concretely, by inversely utilizing the response matrix to obtain the variation of complex conductivity, we can minimize the difference between the simulation results including the effect of surface roughness and the measured ones. Hence, we can effectively determine the conductivity by making maximum use of both the analytical and simulation approaches, even when the surface roughness contributes to the scattering matrix.

3. Formulae for the scattering matrix (transmission coefficient S_{21}^w) using the wire method

The frequency dependence of the conductivity of a resistive chamber can be evaluated using the scattering matrix (transmission coefficient S_{21}^w) of a coaxial waveguide as well. In this, the so-called wire method, a single wire is stretched at the center of the resistive chamber sandwiched by perfectly conductive chambers (aluminum chambers mostly) from both sides. In this section, we present new formulae (see Eqs. (24) and (25)) for the transmission coefficient S_{21}^w of a quasi-transverse electromagnetic (quasi-TEM$_{00}$) mode in the wire method. Derivations of these formulae are given in Appendix B. The simulation results obtained using the wire method will be compared with the analytical results of S_{21}^w.

3.1. Formulae for the transmission coefficient S_{21}^w using the wire method

Figure 8 shows a schematic of the wire method setup. A perfectly conductive single wire of radius ρ_w is stretched out at the center of the chamber with inner radius d, and the current I_0 is driven through the wire. The device under test (the resistive chamber with σ_c, or the reference perfectly conductive chamber) with length $2w(= g)$ is sandwiched between perfectively conductive chambers on both sides [11,33]. The thickness of the chambers is $a - d$. We assume that the perfectly conductive wall covers the outer surface ($\rho = a$) of the chambers, as in the waveguide method.

The formulae for the ratio of the transmission coefficients $S_{21}^w/S_{21}^{w(\mathrm{ref})}$ are given as follows:

$$\frac{S_{21}^w}{S_{21}^{w(\mathrm{ref})}} = \frac{\frac{V_1 \sin kw}{2kw} - j\sum_{m=1}^{\infty} \frac{V_1^{(m)}((-1)^m e^{jkw} - e^{-jkw})k}{2w(k^2 - \frac{m^2\pi^2}{4w^2})} + I_0 Z_c}{Z_c I_0}, \tag{24}$$

for $(k \neq \tilde{n}\pi/2w) \cap (k < i_1/d)$, and

$$\frac{S_{21}^w}{S_{21}^{w(\mathrm{ref})}} = \frac{\frac{V_1 \sin kw}{2kw} - j\sum_{m=1, m\neq\tilde{n}}^{\infty} \frac{V_1^{(m)}((-1)^m e^{jkw} - e^{-jkw})k}{2w(\frac{\tilde{n}^2\pi^2}{4w^2} - \frac{m^2\pi^2}{4w^2})} + \frac{V_1^{(\tilde{n})}[(-1)^{\tilde{n}} e^{j\frac{\tilde{n}\pi}{2}} + e^{-j\frac{\tilde{n}\pi}{2}}]}{4} + I_0 Z_c}{Z_c I_0}, \tag{25}$$

for $(k = \tilde{n}\pi/2w) \cap (k < i_1/d)$, where

$$k = \frac{\omega}{c}, \tag{26}$$

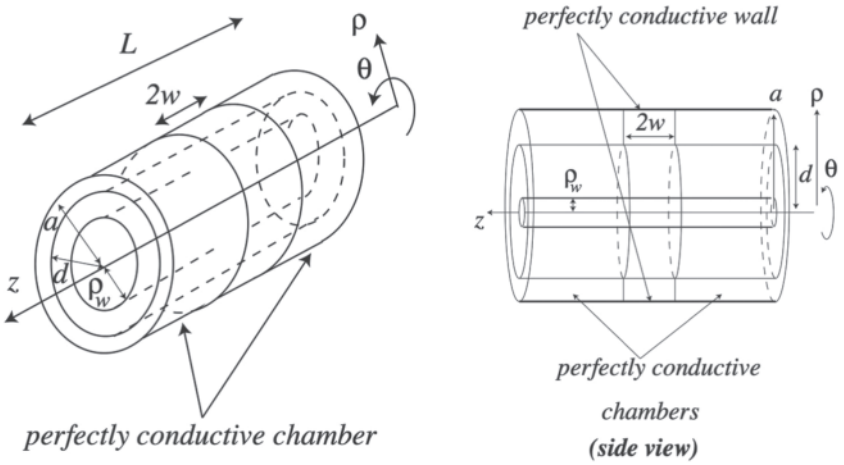

Fig. 8. A schematic picture of the setup of the wire method.

$$Z_c = \frac{Z_0}{2\pi}\log\frac{d}{\rho_w}, \tag{27}$$

i_l is the lth zero of the function $Y_0(x) - Y_0(x\rho_w/d)/J_0(x\rho_w/d)J_0(x)$, $\tilde{n}$ is a positive integer, and S_{21}^{w} and $S_{21}^{w(\mathrm{ref})}$ are the transmission coefficients determined using the wire method of the resistive chamber and the reference (perfectly conductive) chamber, respectively.

The expansion coefficients V_1 and $V_1^{(m)}$ in the formula are determined as follows:

$$\left[\frac{A_0^{(0)}}{2w} + \frac{jkC_0^{(0)}\,\langle J(z)\rangle}{2\pi Z_0}\right]V_1 + \sum_{n=1}^{\infty}\frac{kC_0^{(0)}\left\langle J^{(n)}(z)\right\rangle}{2\pi wZ_0}V_1^{(n)} = -C_0^{(0)}\,\langle\alpha(z)\rangle\,, \tag{28}$$

$$\frac{jkC_0^{(m)}\,\langle\langle J(z)\rangle\rangle_m}{2\pi Z_0}V_1 + \sum_{n=1}^{\infty}\left[\delta_{n,m}A_0^{(n)} + \frac{kC_0^{(m)}\left\langle\left\langle J^{(n)}(z)\right\rangle\right\rangle_m}{2\pi wZ_0}\right]V_1^{(n)} = -C_0^{(m)}\,\langle\langle\alpha(z)\rangle\rangle_m\,, \tag{29}$$

where

$$\langle\alpha\rangle = \frac{I_0}{2\pi d}\frac{\sin kw}{kw}, \tag{30}$$

$$\langle\langle\alpha\rangle\rangle_m = -\frac{I_0}{2\pi d}\frac{k((-1)^m e^{-jkw} - e^{jkw})}{j(k^2 - \frac{m^2\pi^2}{4w^2})}, \tag{31}$$

$$\langle J(z)\rangle = -\frac{2\pi}{wd}\sum_{s=0}^{\infty}\frac{\alpha_s}{(k^2 - \frac{i_s^2}{d^2})} - \frac{\pi}{w^2 d}\sum_{s=0}^{\infty}\frac{\alpha_s(e^{-j\sqrt{k^2-\frac{i_s^2}{d^2}}(2w)} - 1)}{j(k^2 - \frac{i_s^2}{d^2})^{\frac{3}{2}}}, \tag{32}$$

$$\left\langle J^{(m)}(z)\right\rangle = \sum_{s=0}^{\infty}\frac{\pi\alpha_s(1+(-1)^m)(1 - e^{-j\sqrt{k^2-\frac{i_s^2}{d^2}}2w})}{wd\sqrt{k^2 - \frac{i_s^2}{d^2}}(k^2 - \frac{i_s^2}{d^2} - \frac{m^2\pi^2}{4w^2})}, \tag{33}$$

$$\langle\langle J(z)\rangle\rangle_m = \sum_{s=0}^{\infty}\frac{\alpha_s\pi j(1+(-1)^m)(e^{-j2\sqrt{k^2-\frac{i_s^2}{d^2}}w} - 1)}{wd(k^2 - \frac{i_s^2}{d^2} - \frac{m^2\pi^2}{4w^2})\sqrt{k^2 - \frac{i_s^2}{d^2}}}, \tag{34}$$

$$\left\langle\left\langle J^{(n)}(z)\right\rangle\right\rangle_m = \begin{cases} \sum_{s=0}^{\infty} \frac{2\pi\alpha_s(1+(-1)^{n+m})\sqrt{k^2-\frac{i_s^2}{d^2}}(1-(-1)^n e^{-j2\sqrt{k^2-\frac{i_s^2}{d^2}}w})}{d(k^2-\frac{i_s^2}{d^2}-\frac{m^2\pi^2}{4w^2})(k^2-\frac{i_s^2}{d^2}-\frac{n^2\pi^2}{4w^2})}, \text{for } n \neq m, \\ \sum_{s=0}^{\infty} \frac{4\pi\alpha_s\sqrt{k^2-\frac{i_s^2}{d^2}}(1-(-1)^m e^{-j2\sqrt{k^2-\frac{i_s^2}{d^2}}w})}{d(k^2-\frac{i_s^2}{d^2}-\frac{m^2\pi^2}{4w^2})^2} \\ + \sum_{s=0}^{\infty} \frac{j4\pi w\alpha_s}{d(\frac{m^2\pi^2}{4w^2}-k^2+\frac{i_s^2}{d^2})}, \text{for } n = m, \end{cases} \tag{35}$$

$$\alpha_s = \frac{J_0^2[\frac{\rho_w i_s}{d}]}{J_0^2[\frac{\rho_w i_s}{d}] - J_0^2[i_s]}, \text{for } s \geq 1, \tag{36}$$

$$\alpha_0 = \frac{1}{2\log[\frac{d}{\rho_w}]}, \tag{37}$$

$$i_0 \equiv 0, \tag{38}$$

$$\mu_m = \sqrt{\frac{m^2\pi^2}{4w^2} - k^2\tilde{\epsilon}}, \tag{39}$$

$$\tilde{\epsilon} = \frac{\sigma_c Z_0}{jk} + 1, \tag{40}$$

$$A_0^{(m)} = \mu_m a(I_0'(\mu_m d)K_0(\mu_m a) - I_0(\mu_m a)K_0'(\mu_m d)), \tag{41}$$

$$C_0^{(m)} = -\frac{jZ_0\mu_m^2 a(I_0(\mu_m a)K_0(\mu_m d) - I_0(\mu_m d)K_0(\mu_m a))}{k\tilde{\epsilon}}, \tag{42}$$

$$I_0^{(m)} = \frac{jka\tilde{\epsilon}(I_0'(\mu_m d)K_0'(\mu_m a) - I_0'(\mu_m a)K_0'(\mu_m d))}{Z_0}, \tag{43}$$

and

$$K_0^{(m)} = \mu_m a(I_0'(\mu_m a)K_0(\mu_m a) - I_0(\mu_m a)K_0'(\mu_m a)). \tag{44}$$

Especially when $m = 0$, the transfer coefficients $A_0^{(m)}, C_0^{(m)}, I_0^{(m)}$, and $K_0^{(m)}$ are rewritten as

$$A_0^{(0)} = -\frac{\pi\kappa_{cer} d(Y_1(\kappa_{cer} d)J_0(\kappa_{cer} a) - J_1(\kappa_{cer} d)Y_0(\kappa_{cer} a))}{2}, \tag{45}$$

$$C_0^{(0)} = j\frac{\pi\kappa_{cer}^2 aZ_0(-Y_0(\kappa_{cer} d)J_0(\kappa_{cer} a) + J_0(\kappa_{cer} d)Y_0(\kappa_{cer} a))}{2\tilde{\epsilon}k}, \tag{46}$$

$$I_0^{(0)} = -\frac{j\tilde{\epsilon}k\pi a(Y_1(\kappa_{cer} d)J_1(\kappa_{cer} a) - J_1(\kappa_{cer} d)Y_1(\kappa_{cer} a))}{2Z_0}, \tag{47}$$

and

$$K_0^{(0)} = -\frac{\pi\kappa_{cer} d(-Y_0(\kappa_{cer} d)J_1(\kappa_{cer} a) + J_0(\kappa_{cer} d)Y_1(\kappa_{cer} a))}{2}, \tag{48}$$

where

$$\kappa_{cer} = k\sqrt{(\frac{\sigma_c Z_0}{jk} + 1)}. \tag{49}$$

All expansion coefficients V_1 and $V_1^{(m)}$ are obtained by solving Eqs. (28)–(29) for any m.

3.2. *Comparison between theoretical and simulation results of transmission coefficient* $S_{21}^w/S_{21}^{w(\mathrm{ref})}$

In this subsection, we compare the theoretical results of $S_{21}^w/S_{21}^{w(\mathrm{ref})}$ with the simulation results obtained using the wire method. The parameters were selected as follows (unless specified otherwise): the inner radius and the outer radius of the chamber were set to $d = 5$ mm and $a = 11$ mm, respectively. The radius of the wire was set to $\rho_w = 10$ μm. The total length of the resistive chamber was set to $g = 100$ mm. Given that the first zero point i_1 of the function $Y_0(x) - Y_0(x\rho_w/d)/J_0(x\rho_w/d)J_0(x)$ is about 2.68, the upper limit of frequency is below about 26 GHz under the present setup.

The T-Solver module of Microwave Studio in CST Studio Suite 2018 [30] was used to calculate the S-parameters of a coaxial structure composed of wires and metal chambers. The Solver is different from that adopted to the waveguide method in Sect. 2.1. In general, in the case of resistive materials, the mesh size must be sufficiently smaller than the skin depth. In Microwave Studio, the S-parameters were calculated using the technique of surface impedance [34] by adopting "lossy metal" as the ingredient of the resistive chamber with high conductivity.

Figure 9 shows a comparison between the theoretical results of $S_{21}^w/S_{21}^{w(\mathrm{ref})}$ (red •) (based on Eqs. (24) and (25)) and the simulation results of $S_{21}^w/S_{21}^{w(\mathrm{ref})}$ (blue □) (obtained using T-Solver) for $\sigma_c = 5.9 \times 10^7$ S/m. They are in good agreement. Therefore, the validity of the theoretical formulae (Eqs. (24) and (25)) is proven for the high-conductivity case.

To further investigate whether the theoretical results reproduce the simulation ones, let us intentionally reduce the conductivity to ensure a sufficiently small mesh size compared to the skin depth. In the case, "normal metal" is selected as the ingredient of the resistive chamber in the simulations.

We considered three separate chambers with three different conductivities. The first two cases were the constant and pure real conductivities, $\sigma_c = 1$ S/m and $\sigma_c = 3$ S/m, and the third case was the frequency-dependent complex conductivity, σ_{D} (see Eq. (22)) with $\omega_p = 0.146$ THz and $\tau = 10.6$ ps. To prepare for the discussion about the resistive-wall impedance in Sect. 4, we discuss how the simulation results converge as a function of the total mesh number N_{mesh}. Figure 10 shows the results of $\sigma_c = 1$ S/m (top left), $\sigma_c = 3$ S/m (top right), and $\sigma_c = \sigma_{\mathrm{D}}$ with $\omega_p = 0.146$ THz and $\tau = 10.6$ ps (bottom left) for different numbers of meshes. The red • and blue □ lines show the results for $N_{\mathrm{mesh}} = 33\,000\,000$ and $N_{\mathrm{mesh}} = 100\,000\,000$, respectively. The solid, dashed, and dotted lines show the real parts, imaginary parts, and absolute values of the transmission coefficients $S_{21}^w/S_{21}^{w(\mathrm{ref})}$, respectively. The convergence of the simulation results was checked in this way.

Now let us compare the theoretical results with the simulation results in the case of $S_{21}^w/S_{21}^{w(\mathrm{ref})}$. Figure 11 illustrates the theoretical (red •) and simulation (blue □) results of $S_{21}^w/S_{21}^{w(\mathrm{ref})}$ for three different resistive chambers. The upper-left, upper-right, and lower-left panels show the results for $\sigma_c = 1$ S/m, $\sigma_c = 3$ S/m, and $\sigma_c = \sigma_{\mathrm{D}}$ (see Eq. (22)) with $\omega_p = 0.146$ THz and $\tau = 10.6$ ps, respectively. The solid, dashed, and dotted lines show the real parts, imaginary parts, and absolute values of the transmission coefficients $S_{21}^w/S_{21}^{w(\mathrm{ref})}$, respectively. In all three cases, the simulation results were well reproduced by the theoretical results. Once again, the validity of the theoretical formulae (Eqs. (24) and (25)) is proven, this time for the low-conductivity cases.

Finally, let us move to the transmission coefficients $S_{21}^w/S_{21}^{w(\mathrm{ref})}$ at the THz region. To this end, the parameters were specifically set to $\rho_w = 0.5$ μm, $g = 300$ μm, $d = 40$ μm, and $a = 60$ μm. The upper limit of frequency was increased to about 3.3 THz in this setup. Hence, the dimension of the chamber radius becomes the same order of magnitude as that of the waveguide utilized by the

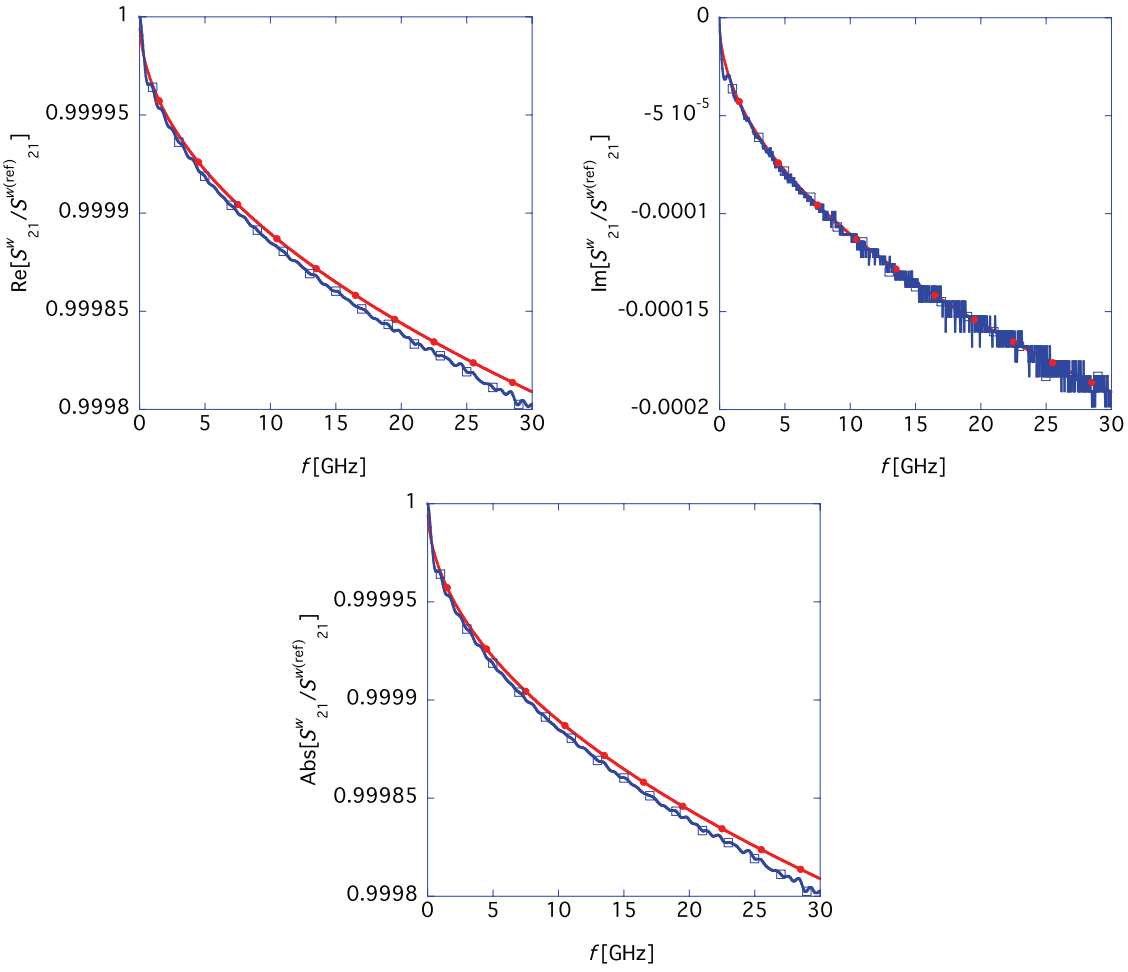

Fig. 9. Transmission coefficient $S_{21}^{w}/S_{21}^{w(\mathrm{ref})}$ for $\sigma_c = 5.9 \times 10^7$ S/m, $g = 100$ mm, $\rho_w = 10$ μm, $d = 5$mm, and $a = 11$ mm. The red • and blue □ lines denote the theoretical and simulation results, respectively. The upper-left, upper-right, and lower-left panels represent the real parts, imaginary parts, and absolute values of the transmission coefficients $S_{21}^{w}/S_{21}^{w(\mathrm{ref})}$, respectively.

waveguide method in Sect. 2.3. The conductivity σ_c was 187.566 S/m so we could use the "normal metal" option as an ingredient of the resistive chamber. The conductivity of real metal could be considerably lower in the THz region.

Figure 12 shows the theoretical (red •) and simulation (blue □) results of $S_{21}^{w}/S_{21}^{w(\mathrm{ref})}$. The simulation results are reproduced by the theoretical ones, even in the THz region. Now we have confirmed that the present theory of the transmission coefficient based on the wire method can reproduce the simulation results for any conductivity and frequency region.

4. Longitudinal resistive-wall beam impedance

The resistive-wall beam coupling impedances of a resistive chamber have been evaluated based on S-matrices measured with the wire method by using the standard log-formula [12]:

$$Z_L^w = -2Z_c \log \frac{S_{21}^w}{S_{21}^{w(\mathrm{ref})}}. \tag{50}$$

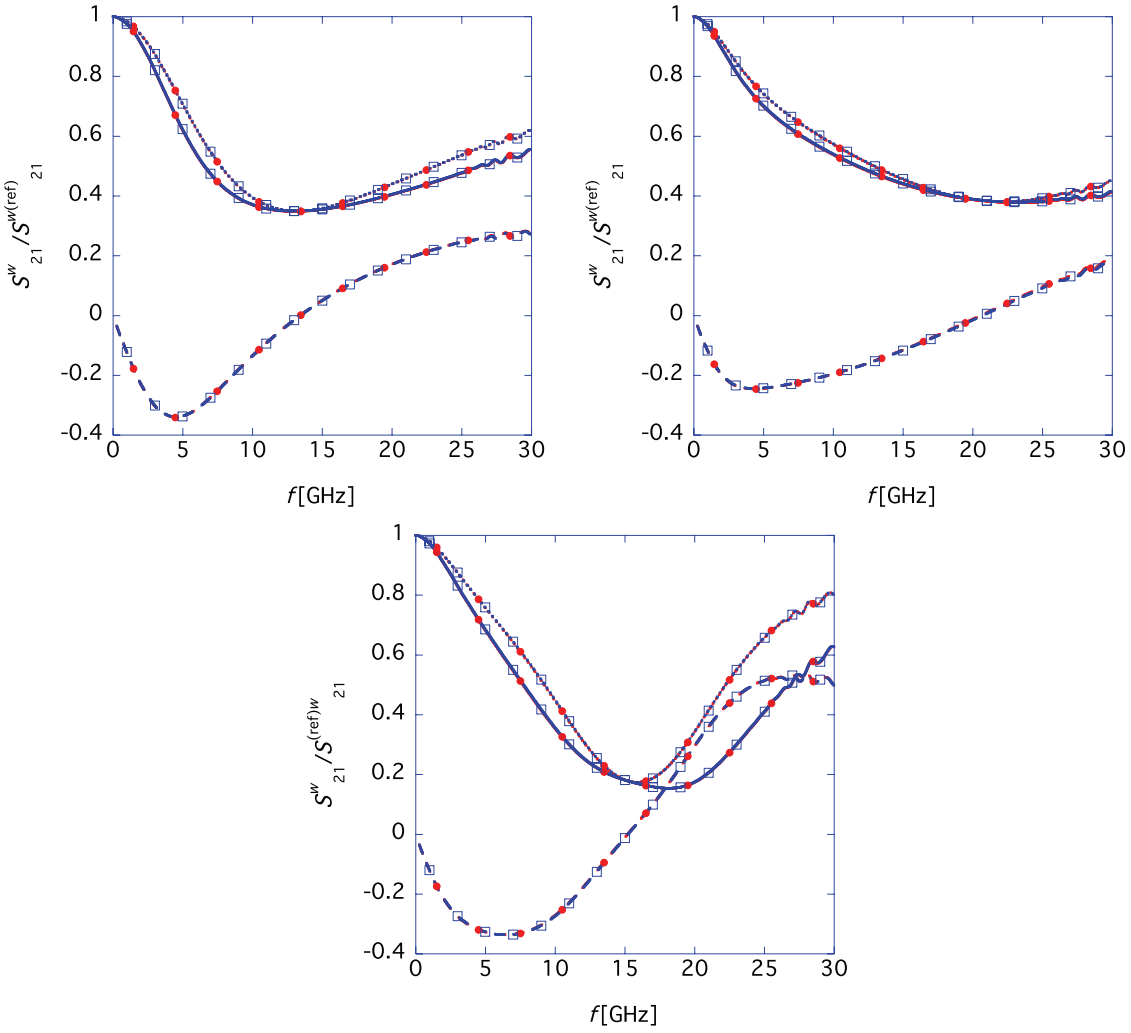

Fig. 10. Dependence of $S^w_{21}/S^{w(\mathrm{ref})}_{21}$ on mesh number N_{mesh} for chambers of $\sigma_c = 1$ S/m (top left), $\sigma_c = 3$ S/m (top right), and $\sigma_c = \sigma_{\mathrm{D}}$ (see Eq. (22)) with $\omega_p = 0.146$ THz and $\tau = 10.6$ ps (bottom left). The red • and blue □ lines represent the results for $N_{\mathrm{mesh}} = 33\,000\,000$ and $N_{\mathrm{mesh}} = 100\,000\,000$, respectively. The solid, dashed, and dotted lines represent the real parts, imaginary parts, and absolute values of the transmission coefficients $S^w_{21}/S^{w(\mathrm{ref})}_{21}$, respectively.

One "big" question is how accurately this measured impedance Z^w_L represents the real resistive-wall impedance for a beam (we call it the "resistive-wall beam impedance Z_L"). To this end, we present theoretical formulae for the resistive-wall beam impedance Z_L in the following subsection. Then, we compare the resistive-wall impedance Z^w_L by using the wire method with the theoretical resistive-wall beam impedance Z_L in the final subsection.

4.1. The theoretical resistive-wall impedance for a relativistic beam

Once the frequency dependence of the (complex) conductivity is known, the resistive-wall beam impedance Z_L can be calculated analytically. The resistive-wall beam impedances [3] of an infinitely long multi-layered chamber have been analytically studied by many researchers [4,14–27]. Basically, it is a 2D problem, and can be solved by the field-matching technique [35].

Simulations of the resistive-wall beam impedance are quite difficult because the mesh size needs to be sufficiently small compared to the skin depth. In our experience, the Wake Solver of CST Studio

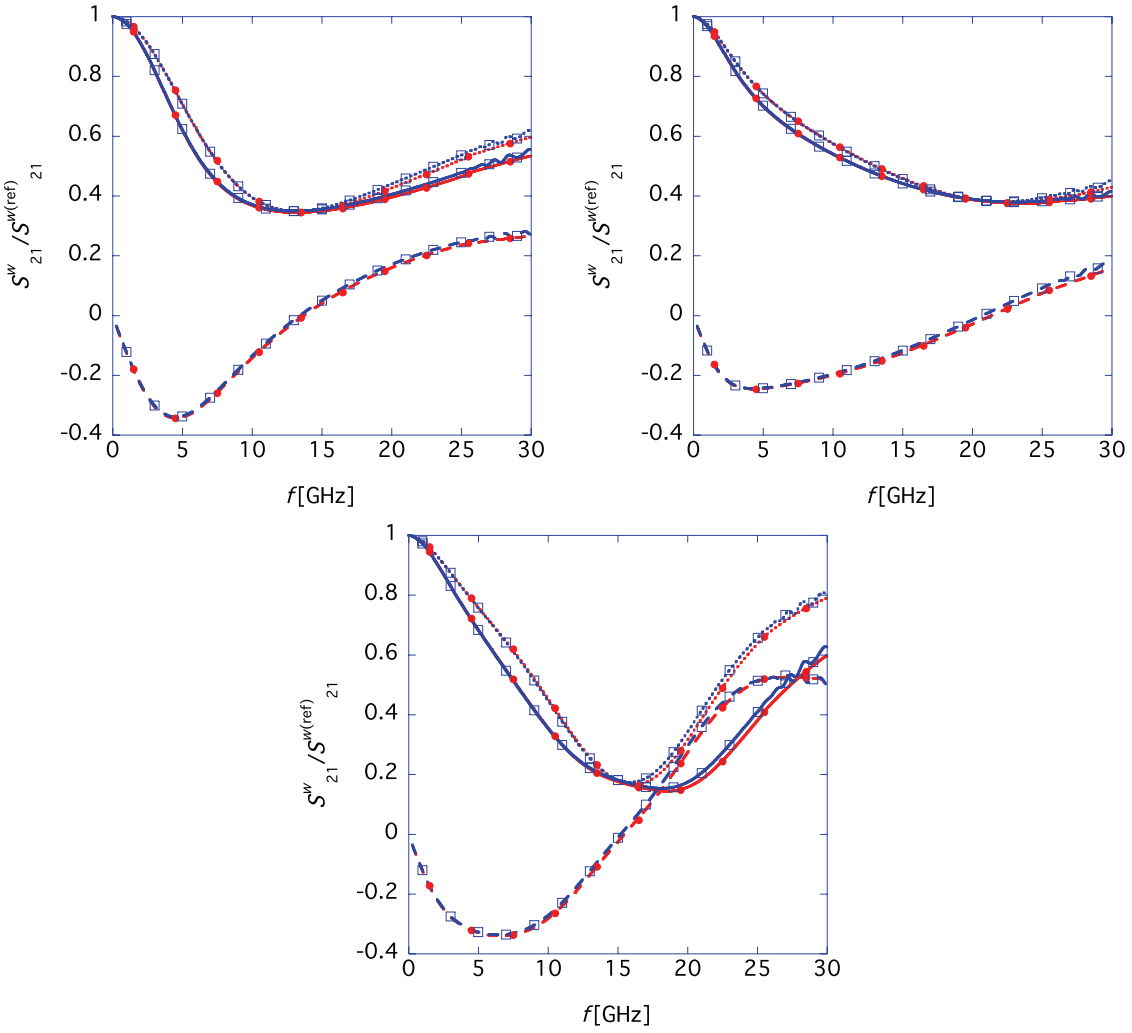

Fig. 11. Theoretical (red •) and simulation (blue □) results of transmission coefficients $S^w_{21}/S^{w(\mathrm{ref})}_{21}$. The upper-left, upper-right, and lower-left panels show the results for $\sigma_c = 1$ S/m, $\sigma_c = 3$ S/m, and $\sigma_c = \sigma_{\mathrm{D}}$ (see Eq. (22)) with $\omega_p = 0.146$ THz and $\tau = 10.6$ ps, respectively. The solid, dashed, and dotted lines represent the real parts, imaginary parts, and absolute values of the transmission coefficients $S^w_{21}/S^{w(\mathrm{ref})}_{21}$, respectively.

seems not to be able to simulate the resistive-wall beam impedance accurately, even if we utilize "lossy metal" as the ingredient, to which the surface impedance technique is applied by neglecting the induction term in the Maxwell–Ampère equation [4].

Instead, let us analytically investigate the characteristic behavior of the resistive-wall beam impedance by taking the simplest case; namely, a single layered chamber is covered over a perfectly conductive chamber (see Appendix D). We will see that the correct formula for the resistive-wall beam impedance cannot be obtained by neglecting the induction term in the Maxwell–Ampère equation under a certain condition.

The rigorous formula for the resistive-wall beam impedance for a relativistic beam is given by

$$\frac{Z_L}{g} = \frac{\left(K_0(\nu a) I_0(\nu d) - I_0(\nu a) K_0(\nu d)\right)\frac{1}{2\pi d}}{-\frac{(\sigma_c + j\omega\epsilon_0)(K_0(\nu a)I_1(\nu d) + I_0(\nu a)K_1(\nu d))}{\nu} + \frac{jkd(K_0(\nu a)I_0(\nu d) - I_0(\nu a)K_0(\nu d))}{2Z_0}}, \tag{51}$$

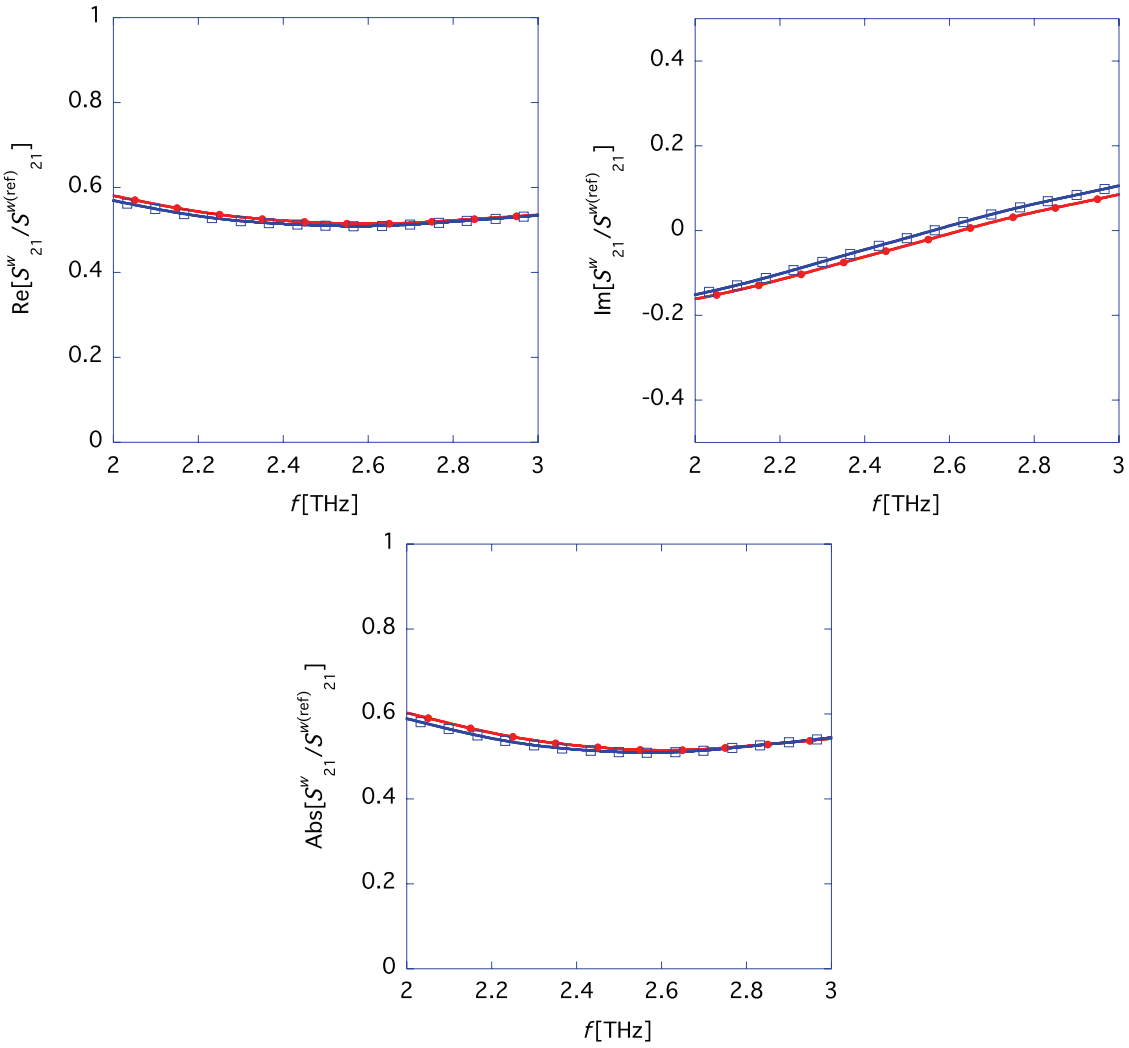

Fig. 12. Theoretical (red •) and simulation (blue □) results of transmission coefficients $S_{21}^{w}/S_{21}^{w(\mathrm{ref})}$, where $\sigma_c = 187.566$ S/m, $g = 300$ μm, $d = 40$ μm, $a = 60$ μm, and $\rho_w = 0.5$ μm. The upper-left, upper-right, and lower-left panels represent the real parts, imaginary parts, and absolute values of the results, respectively.

where

$$\nu = \sqrt{jkZ_0\sigma_c}, \tag{52}$$

$$k = \frac{\omega}{c}, \tag{53}$$

while the approximate one neglecting the induction term is given by

$$\frac{Z_L}{g} = \frac{\left(K_0\left(\nu_{no}a\right)I_0\left(\nu_{no}d\right) - I_0\left(\nu_{no}a\right)K_0\left(\nu_{no}d\right)\right)\frac{1}{2\pi d}}{-\frac{\sigma_c\left(K_0(\nu_{no}a)I_1(\nu_{no}d)+I_0(\nu_{no}a)K_1(\nu_{no}d)\right)}{\nu_{no}} + \frac{jkd\left(K_0(\nu_{no}a)I_0(\nu_{no}d)-I_0(\nu_{no}a)K_0(\nu_{no}d)\right)}{2Z_0}}, \tag{54}$$

where

$$\nu_{no} = \sqrt{k^2 + jkZ_0\sigma_c}. \tag{55}$$

Figure 13 shows the rigorous formula (51) as a function of frequency, where $\sigma_c = 5.9 \times 10^7$ S/m, $d = 5$ mm, and $a = 11$ mm. The black and brown lines show the real and imaginary parts of the

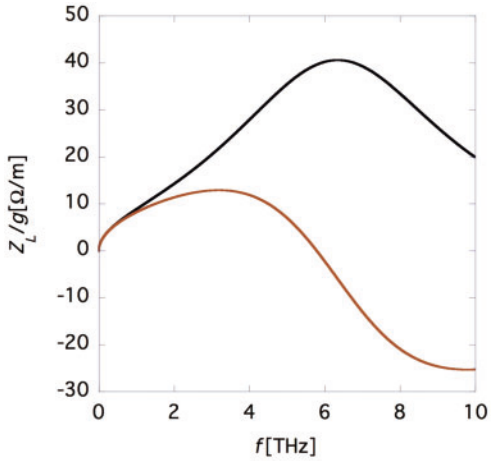

Fig. 13. Theoretical result of the longitudinal resistive-wall beam impedance Z_L per unit length, where $\sigma_c = 5.9 \times 10^7$ S/m, $d = 5$ mm, and $a = 11$ mm. The black and brown lines denote the real and imaginary parts of the impedance, respectively.

impedance, respectively. The formula (51) reproduces the conventional formula for the resistive-wall beam impedance at low frequency [10]:

$$\frac{Z_L}{g} = Z_0 \sqrt{\frac{2\omega}{cZ_0\sigma_c}} \frac{(1+j)}{4\pi d}. \tag{56}$$

In this example, the real part of the impedance has a peak at around 6 THz, and then goes down in proportion to the inverse of the frequency [23,24]. A typical explanation of this behavior is as follows. The Maxwell–Ampère equation is given by

$$\epsilon_0 \frac{\partial \vec{E}}{\partial t} + \vec{J} = \mathrm{rot}\vec{H}, \tag{57}$$

where $\vec{J}$ is the electric current density. Assuming that electromagnetic fields have a time dependence of $e^{j\omega t}$, Eq. (57) can be written inside a conductive material as

$$(j\epsilon_0\omega + \sigma_c)\vec{E} = \nabla \times \vec{H}. \tag{58}$$

For the frequency range of $\sigma_c \lesssim \epsilon_0\omega$, the induction term $\epsilon_0 \partial\vec{E}/\partial t$ starts to dominate the current density term $\vec{J}$. At the frequency range $\epsilon_0\omega \gg \sigma_c$, the conductivity term contributes little to the Maxwell equations. As a result, the conductive material behaves almost like a vacuum at very high frequencies. The electromagnetic fields can now freely propagate away from the chamber and thus the longitudinal impedance diminishes.

However, the critical frequency $\sigma_c/2\pi\epsilon_0$, at which the conductive term and the induction one become comparable, is around a few EHz for $\sigma_c = 5.9 \times 10^7$ S/m. Moreover, the mountain-shaped curve of the longitudinal impedance (see Fig. 13) is already known, even under the approximation ($\sigma_c \gg \epsilon_0\omega$) [19]. Therefore, the above explanation is not good enough to explain the mountain-shaped curve of the impedance.

We can derive a formula for the peak frequency of the longitudinal impedance, as follows. When the induction term in the Maxwell–Ampère equation can be neglected, namely $\sigma_c \gg \epsilon_0\omega$, the

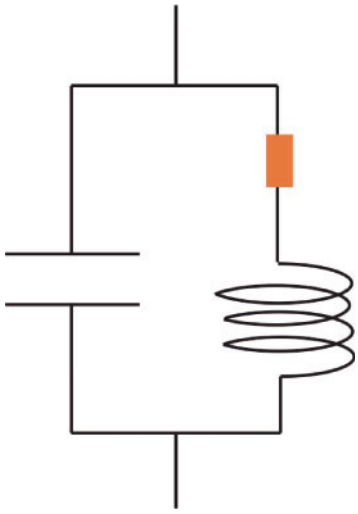

Fig. 14. The equivalent electrical circuit for Z_L.

resistive-wall beam impedance of a conductive material with "infinite" thickness is much simplified as

$$Z_L = \frac{1}{\left[\frac{(1+j\frac{\epsilon_0\omega}{\sigma_c})}{\frac{(1+j)}{2\pi d}\frac{\omega\mu_0}{2}\sqrt{\frac{2}{\mu_0\omega\sigma_c}}g} + j\epsilon_0\omega\frac{\pi d^2}{g}\right]}. \tag{59}$$

This means that Z_L is equivalent to the parallel circuit shown in Fig. 14.

The peak frequency f_R at the real part of the longitudinal impedance is thus given by

$$f_R = \frac{c}{\pi(\frac{d^2}{Z_0\sigma_c})^{\frac{1}{3}}}. \tag{60}$$

It is about 9 THz for $\sigma_c = 5.9 \times 10^7$ S/m and $d = 5$ mm, and is comparable to the more rigorous result shown in Fig. 13 including the induction term.

Just for a rough estimate of the impedance, the approximate formula (54) without the induction term may be enough. However, if the chamber radius d satisfies the condition

$$\frac{c}{\pi(\frac{d^2}{Z_0\Re[\sigma_c]})^{\frac{1}{3}}} \gtrsim \frac{\max[\Re[\sigma_c], \Im[\sigma_c]]}{2\pi\epsilon_0}, \tag{61}$$

the induction term starts to play an important role in evaluating the impedances, and we have to use the more precise formula (51) for an accurate estimate of the impedance at the frequency.

One example is shown in Fig. 15, where we use the Drude conductivity model (Eq. (22) with $\tau = 3.72$ ps and $\omega_p = 6.83$ THz [36]); the outer radius of the resistive chamber is fixed to $a = 11$ mm and the inner radius d is chosen as a free parameter. The upper, middle, and lower panels show the results with $d = 1$ mm, $d = 2$ mm, and $d = 4$ mm, respectively [37,38]. The black lines show the rigorous results by the formula (51), while the brown lines are based on the approximate formula (54). The results reveal that, as the chamber radius d increases, the peak frequency becomes lower and the agreement becomes better between the rigorous formula and the approximate one.

This can be understood as follows. In this case, the frequency satisfying the equation

$$f = \frac{\max[\Re[\sigma_c], \Im[\sigma_c]]}{2\pi\epsilon_0}, \tag{62}$$

is 0.368 THz, while the frequencies satisfying the equation

$$f = \frac{c}{\pi(\frac{d^2}{Z_0 \Re[\sigma_c]})^{\frac{1}{3}}}, \tag{63}$$

are 0.245 THz for $d = 1$ mm, 0.185 THz for $d = 2$ mm, and 0.139 THz for $d = 4$ mm, respectively. Hence, the peak frequency is lowered by increasing the chamber radius d. Furthermore, comparing those frequencies with 0.368 THz, we find that the condition (61) becomes more satisfied as the chamber radius d becomes smaller. That is why the discrepancy between the rigorous formula and the approximate one becomes more remarkable for a smaller chamber radius d. Needless to say, in the frequency region

$$f > \frac{\max[\Re[\sigma_c], \Im[\sigma_c]]}{2\pi\epsilon_0}, \tag{64}$$

the induction term plays an important role in describing the impedances, regardless of the value of radius d.

As this example indicates, it is preferable to check whether the resistive chamber satisfies the condition (61) at a given frequency, for an accurate estimate of the resistive-wall beam impedance Z_L, especially when simulation studies can be performed by neglecting the induction term.

4.2. Comparison between theoretical and simulation results of resistive-wall impedance

Now we compare the resistive-wall impedance Z_L^w obtained using the wire method with the theoretical resistive-wall beam impedance Z_L. Figure 16 represents one such example for a highly conductive chamber ($\sigma_c = 5.9 \times 10^7$ S/m, $\rho_w = 10$ μm, $d = 5$ mm, and $a = 11$ mm), with the analytical results of Z_L^w (red) (based on Eqs. (24), (25), and (50)), simulation results of Z_L^w (purple) obtained using the T-Solver and Eq. (50), and theoretical results of resistive-wall beam impedance Z_L (black) (Eq. (51)). This result demonstrates that they are in good agreement. In particular, the agreement between the analytical results of Z_L^w (red) and the theoretical beam impedance Z_L (black) is perfect.

Next, we investigate whether the mountain-shaped curve in the theoretical resistive-wall beam impedances Z_L can be reproduced accurately by the resistive-wall impedances Z_L^w by using the wire method and lowering the conductivity of the chamber (refer to Eq. (60)). Figure 17 shows the analytical results of Z_L^w (red), simulation results of Z_L^w (blue), and theoretical results of resistive-wall beam impedance Z_L (black) for three different resistive chambers. The upper-left, upper-right, and lower-left panels show the results for $\sigma_c = 1$ S/m, $\sigma_c = 3$ S/m, and $\sigma_c = \sigma_{\mathrm{D}}$, respectively, where σ_{D} follows the Drude model (22) for the frequency-dependent complex conductivity with $\omega_p = 0.146$ THz and $\tau = 10.6$ ps. The solid and dashed lines show the real and imaginary parts of the impedances, respectively. The mountain-shaped curves can be observed in all three cases. While the agreement between the analytical (red) and the simulation (blue) results of Z_L^w, which converge sufficiently as shown in Fig. 10 at this mesh size, is relatively good, their behaviors are distinguishably different from the theoretical beam impedance Z_L (black). This result indicates the accuracy limit in the evaluation of the resistive-wall impedance with lower conductivity using the wire method and the log-formula (50).

The log-formula for distributed impedances is obtained by perturbation theory for small impedance and a thin wire limit [13]. Figure 18 represents the analytical result of Z_L^w (blue) for $\rho_w = 0.1$ μm and that (red) for $\rho_w = 10$ μm and the theoretical result of beam impedance Z_L (black), where

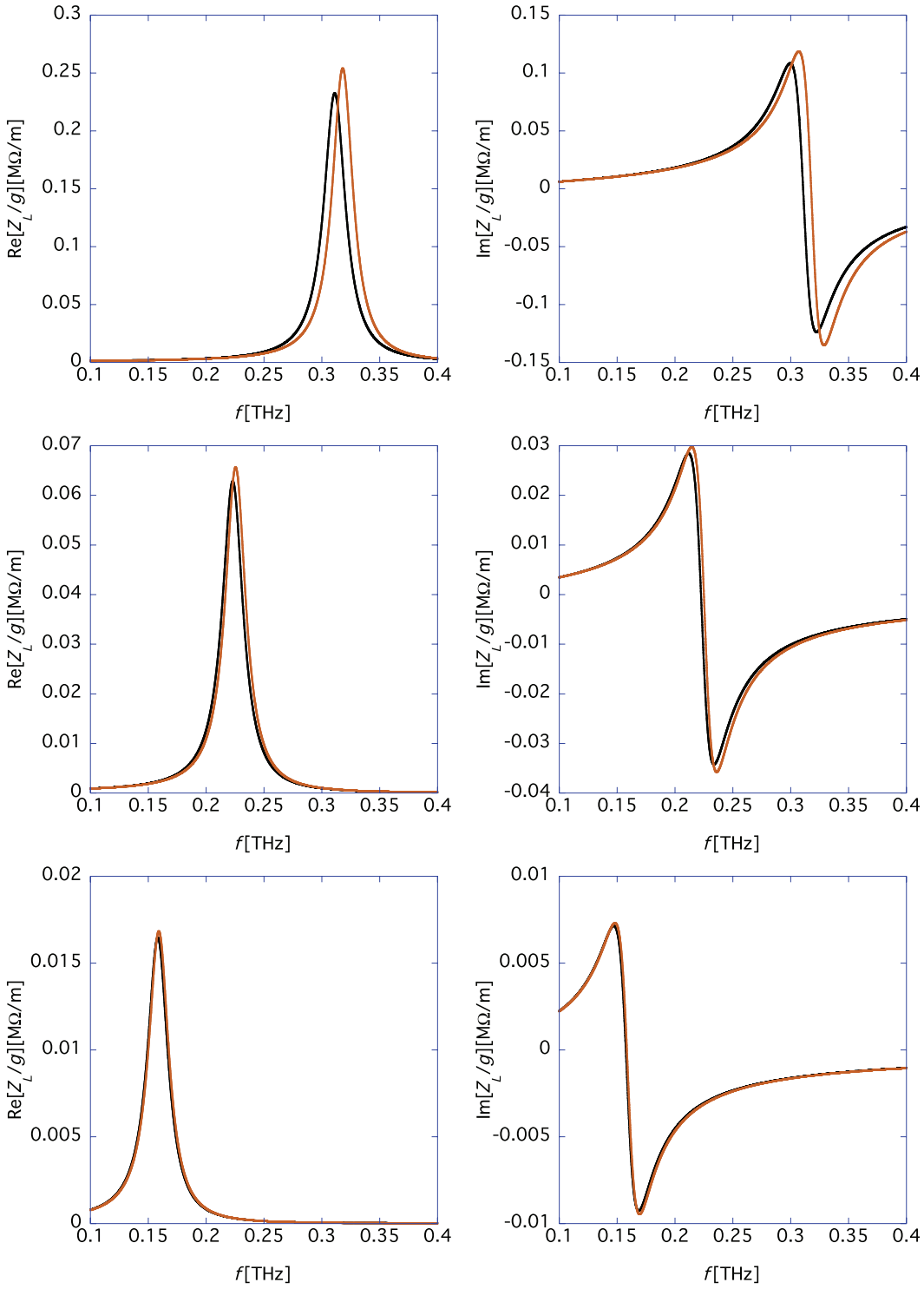

Fig. 15. Theoretical results of longitudinal impedance per unit length from 0.1 THz to 0.4 THz for chambers with $d = 1$ mm (top), $d = 2$ mm (middle), and $d = 4$ mm (bottom), respectively, where the complex conductivity is given by Eq. (22) with $\tau = 3.72$ ps and $\omega_p = 6.83$ THz. The black and brown lines show the resistive-wall beam impedances with and without the induction term, respectively.

$\sigma_c = 1$ S/m. The result illustrates that Z_L^w approaches Z_L as the wire radius ρ_w becomes smaller, which demonstrates that the boundary condition due to the wire significantly deforms the impedance Z_L^w from the beam impedance Z_L with low conductivity.

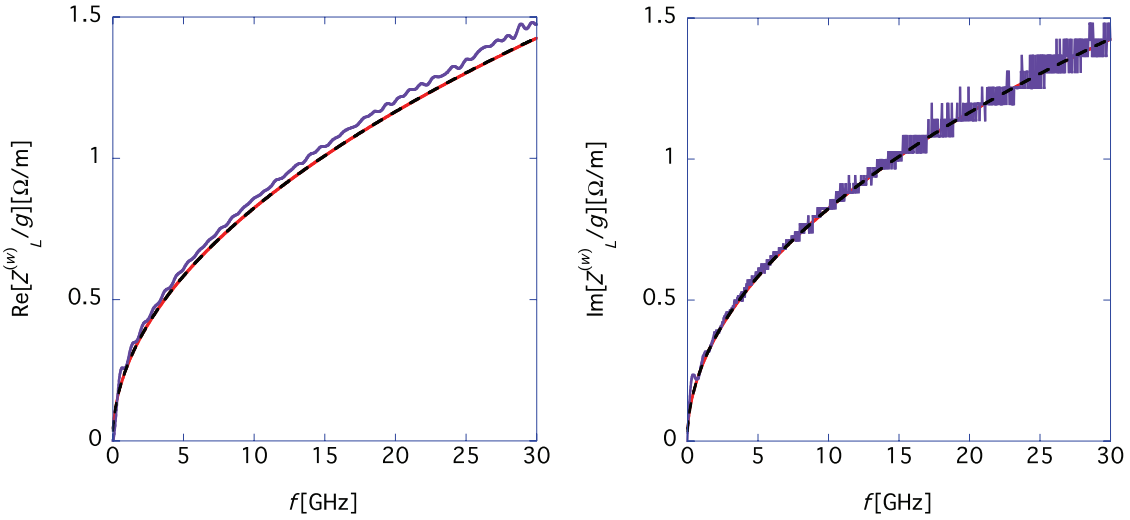

Fig. 16. Analytical result (red) of Z_L^w, simulation result (purple) of Z_L^w, and theoretical result of beam impedance (black) Z_L, respectively, where $\sigma_c = 5.9 \times 10^7$ S/m, $\rho_w = 10$ μm, $d = 5$ mm, and $a = 11$ mm. The left and right panels represent the real and imaginary parts of the impedances, respectively.

These exercises led us to the following conclusions:

(1) Measurements of S-matrices by using the wire method and the constructed resistive-wall impedance Z_L^w by using the log-formula (50) provide an overall well-behaved resistive-wall beam impedance Z_L. The agreement between the resistive-wall impedance Z_L^w and the resistive-wall beam impedance Z_L is good for higher conductivity, while the accuracy of the wire method is limited for lower conductivity.
(2) For evaluating the accuracy of the resistive-wall beam impedance Z_L, we should first find the frequency dependence of the complex conductivity of the resistive chamber by comparing the measured S-matrices with the theoretical ones obtained using complex conductivity σ_c as a fitting parameter.
(3) Then, we can construct the resistive-wall beam impedance Z_L by using the obtained frequency dependence of complex conductivity σ_c and Eq. (51), instead of using the log-formula (50).

Besides the resistive-wall beam impedance, the surface roughness of the chambers can contribute to the total beam impedances at high frequency [39]. Accordingly, this effect should be taken into account from the beam impedance and beam instability points of view.

5. Discussions about some intrinsic errors of the measurement setup of the wire method

These calculated scattering matrices $S_{21}^w/S_{21}^{w(\mathrm{ref})}$ or the resistive-wall impedance Z_L^w in the wire method are based on the assumption that the measurement devices are perfectly fabricated and aligned, and the wire is perfectly positioned at the center of the devices. In reality, there may be a gap between the central cylinder and the sandwiching chambers, or the wire may have a droop, which would deform the characteristic impedance for the setup. The surface roughness on the chambers can modulate the measurement results in the THz region.

Here, let us consider a prescription evaluating the contributions of the setup errors to the measured scattering matrices $S_{21}^w/S_{21}^{w(\mathrm{ref})}$, or the resistive-wall impedances Z_L^w, and finding the requirements

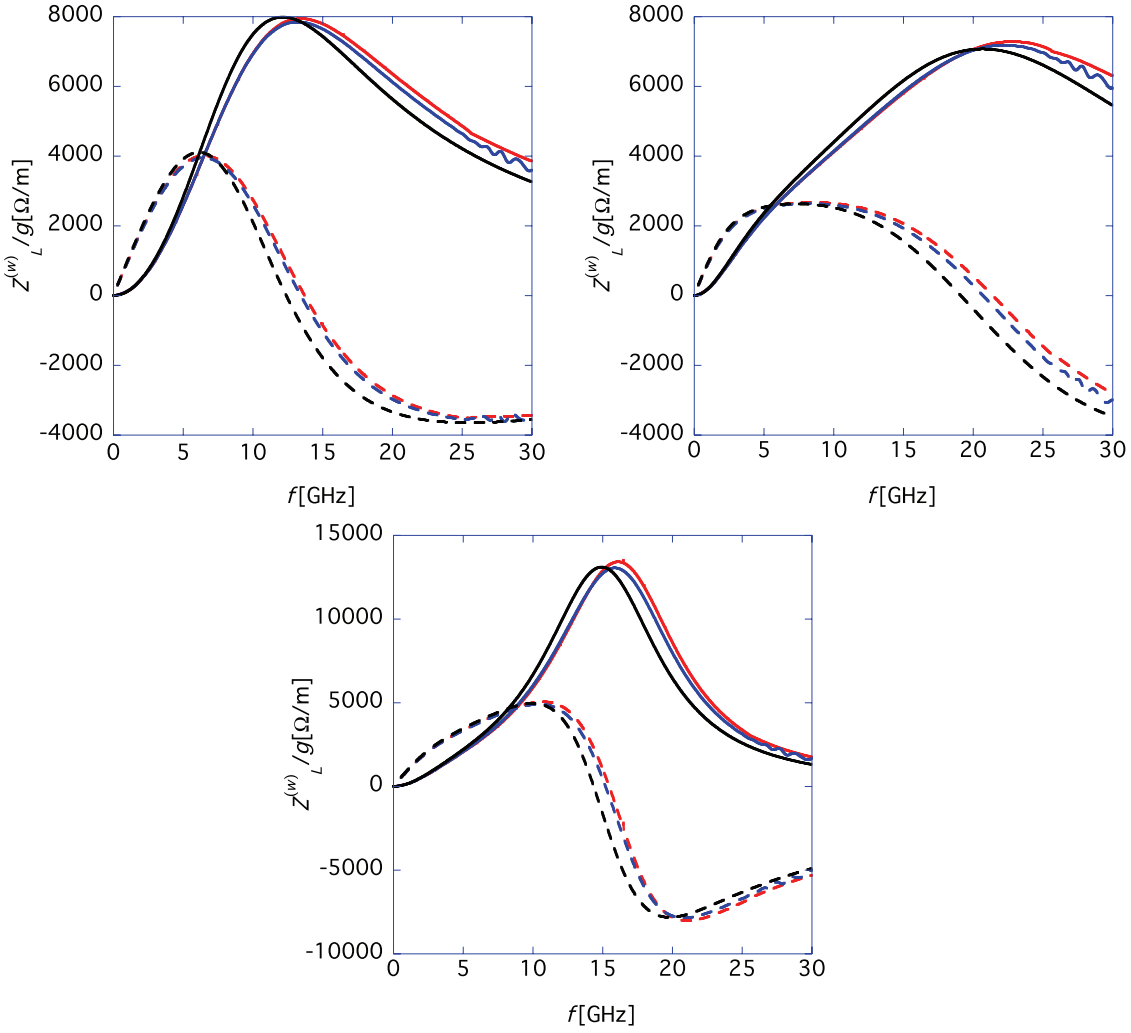

Fig. 17. Analytical result (red) of Z_L^w, simulation result (blue) of Z_L^w, and theoretical result of beam impedance (black) Z_L, respectively. The upper-left, upper-right, and lower-left panels represent the results in the case of $\sigma_c = 1$ S/m, $\sigma_c = 3$ S/m, and $\sigma_c = \sigma_D$ (see Eq. (22)) with $\omega_p = 0.146$ THz and $\tau = 10.6$ ps, respectively. For all cases, the parameters are chosen as $\rho_w = 10$ μm, $d = 5$ mm, and $a = 11$ mm. The solid and dashed lines represent the real and imaginary parts of the impedance, respectively.

of the setup for the precise measurements toward the THz region by simulation approaches. To save excessive memory and CPU time, let us confine the total length of the setup to 200 μm, and consider a short resistive material with $g = 10$ μm and $\sigma_c = 187.566$ S/m in the THz region, sandwiched between 95 μm long aluminum chambers, with the other parameters set to $\rho_w = 0.5$ μm, $d = 40$ μm, and $a = 60$ μm as in Fig. 12. Aluminum is well described by the Drude model (22), where $\omega_p = 23.2$ pHz and $\tau = 1.1$ fs [40]. The huge conductivity of aluminum $|\sigma_c| \sim 10^6$ S/m at 2 THz enables us to approximate the aluminum chambers by perfectly conductive chambers. The device under test is typically called a resistive insert [41], not a resistive chamber. We calculate the reference scattering matrix $S_{21}^{w(\mathrm{ref})}$ by replacing only the device under test (the resistive insert) with the perfectly conductive short reference ring. In other words, the respective sandwiching chambers for the resistive insert are identical to those for the reference ring including the surface roughness, when the scattering matrices S_{21}^w and $S_{21}^{w(\mathrm{ref})}$ are calculated.

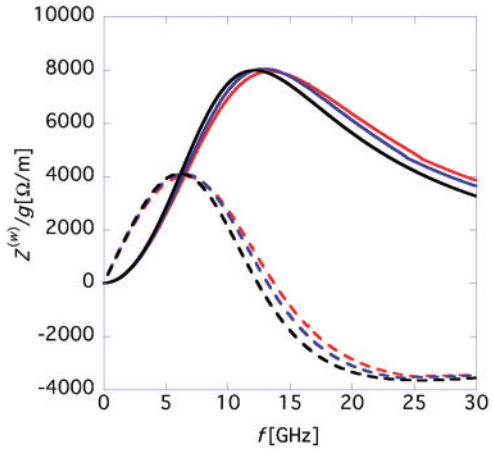

Fig. 18. Analytical result of Z_L^w (blue) for $\rho_w = 0.1$ μm, that (red) for $\rho_w = 10$ μm, and theoretical result of beam impedance (black) Z_L, respectively, where $\sigma_c = 1$ S/m, $d = 5$ mm, and $a = 11$ mm. The solid and dashed lines represent the real and imaginary parts of the impedance, respectively.

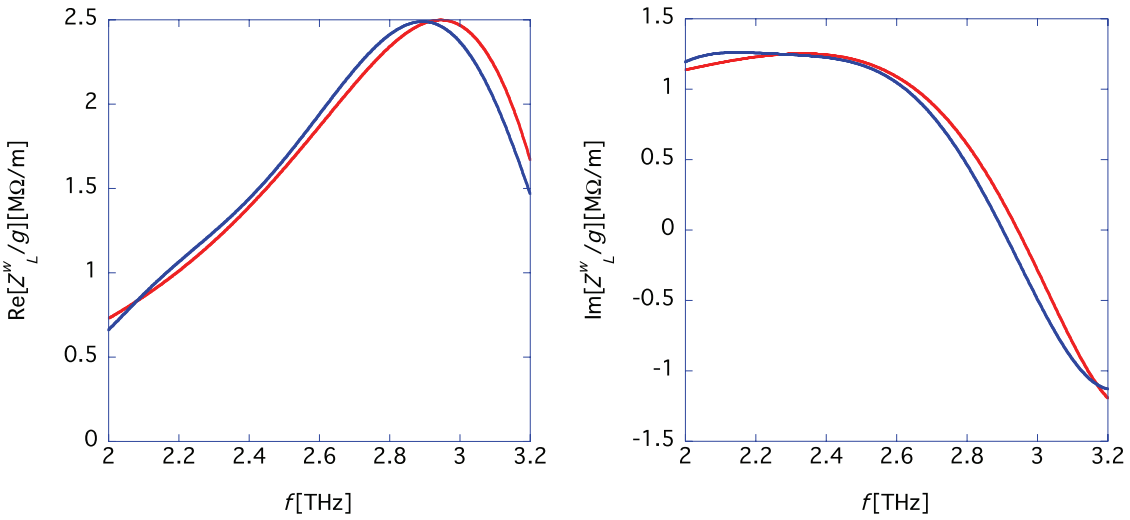

Fig. 19. Analytical result (red) of Z_L^w and simulation result (blue) of Z_L^w, respectively, for the resistive insert, where $\sigma_c = 187.566$ S/m, $g = 10$ μm, $d = 40$ μm, $a = 60$ μm, and $\rho_w = 0.5$ μm. The left and right panels represent the real and imaginary parts of the impedance, respectively.

First, let us compare the analytical with the simulation results of "the resistive-wall insert impedance" Z_L^w with $g = 10$ μm, where we assume that the chambers are perfectly fabricated with smooth surfaces, and the positions of the central ring, the sandwiching chambers, and the wire are perfectly aligned. The analytical and simulation results are denoted by the red and blue lines in Fig. 19, respectively.

For comparison, Fig. 20 shows "the resistive-wall chamber impedance" Z_L^w with $g = 300$ μm, obtained by converting $S_{21}^w/S_{21}^{w(\mathrm{ref})}$ in Fig. 12 to the resistive-wall impedances Z_L^w via Eq. (50). The red and blue lines denote the analytical and simulation results, respectively.

In Figs. 19 and 20, the order of magnitude of the impedances per unit length is around MΩ/m in these ideal cases. We find that a change in the length g produces a difference in the impedances between both results, which means that the analytical results successfully reproduce the simulation

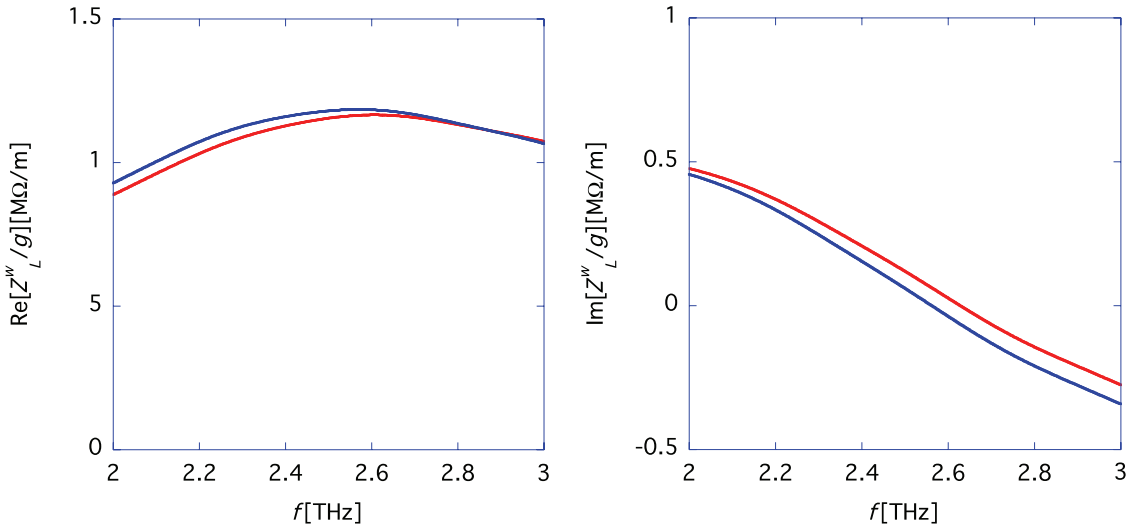

Fig. 20. Analytical result (red) of Z_L^w and simulation result (blue) of Z_L^w, respectively, where $\sigma_c = 187.566$ S/m, $g = 300$ μm, $d = 40$ μm, $a = 60$ μm, and $\rho_w = 0.5$ μm. The left and right panels represent the real and imaginary parts of the impedances, respectively.

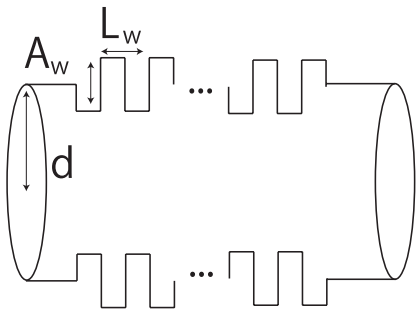

Fig. 21. A schematic of the corrugated wall on a chamber surface.

results for any length of g. Nevertheless, as in the results in the THz region by the waveguide method (see Fig. 6), a slight discrepancy is seen between the analytical and simulation results.

Here, let us consider how the ideal results are deformed due to the intrinsic errors of the measurement setup. Figure 21 represents a schematic of 2D corrugation structures, modeling the surface roughness on chambers. The dimensions are specified by two parameters: L_w and A_w.

For simplicity, let us consider a perfectly conductive tiny chamber with a corrugated wall. By letting a beam pass through the chamber, we can find the dependence of the parameters L_w and A_w on the corrugated wall beam impedance Z_L [39]. The simulation was done by using the 2D simulation code ABCI [42]. The results are shown in Fig. 22, where the black, brown, blue, red, and green lines show the results with $L_w = A_w = 0.200$ μm, $L_w = A_w = 0.100$ μm, $L_w = A_w = 0.050$ μm, $L_w = A_w = 0.025$ μm, and $L_w = A_w = 0.005$ μm, respectively. The results suggest that the contribution of the surface roughness to the real part of the resistive-insert impedance Z_L^w with $\sigma_c = 187.566$ S/m is made negligibly small, while that to the imaginary part becomes less than about 0.2% for the ideal result of impedance shown in Fig. 19, by reducing the corrugation parameters (L_w and A_w) below 0.100 μm against the inner radius $d = 40$ μm.

In order to demonstrate the expectation, let us move back to the 3D simulation for the wire method, where the surface roughness is taken into consideration both for the resistive insert and the

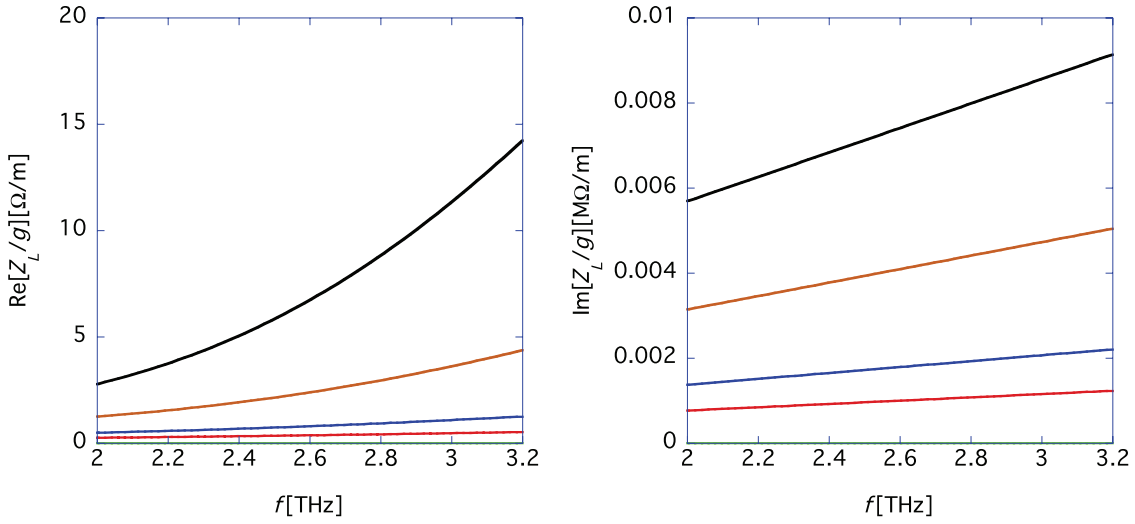

Fig. 22. The parameter dependence on the beam impedance Z_L for a perfectly conductive chamber with corrugated wall, and $d = 40$ μm. The black, brown, blue, red, and green lines show the results with $L_w = A_w = 0.200$ μm, $L_w = A_w = 0.100$ μm, $L_w = A_w = 0.050$ μm, $L_w = A_w = 0.025$ μm, and $L_w = A_w = 0.005$ μm, respectively. Notice that the vertical scales are different for the real (left) and imaginary (right) parts of the impedance.

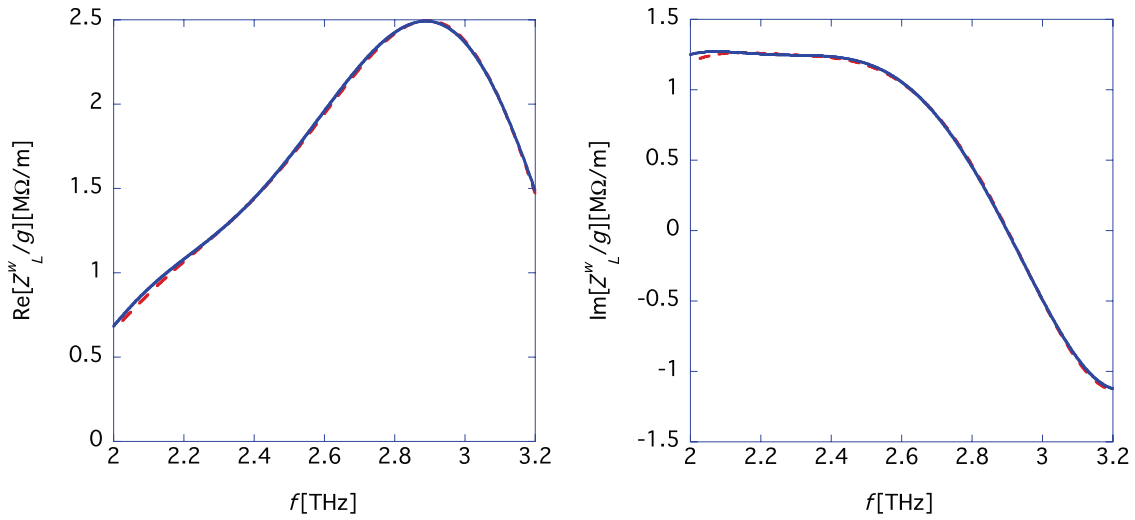

Fig. 23. The impedance Z_L^w with (red dashed) and without (blue) the effect of surface roughness with $L_w = A_w = 0.100$ μm on the chambers.

sandwiching chambers. The simulation results are shown in Fig. 23. The red and blue lines denote Z_L^w with and without the effects of surface roughness. To obtain the red line, the only corrugated resistive insert is replaced by the perfectly conductive reference ring with a smooth inner surface, when we calculate the reference scattering matrix $S_{21}^{w(\mathrm{ref})}$. As expected, the difference between both results is negligible compared to that between the analytical and simulation results shown in Fig. 19. The results indicate that the surface roughness with $L_w = A_w = 0.100$ μm is tolerable, if the sandwiching chambers are shared in both the measurements of S_{21}^w and $S_{21}^{w(\mathrm{ref})}$.

Finally, let us intentionally misalign the positions of the resistive insert and two sandwiching chambers up to 0.100 μm, retaining the surface roughness with $L_w = A_w = 0.100$ μm. Based

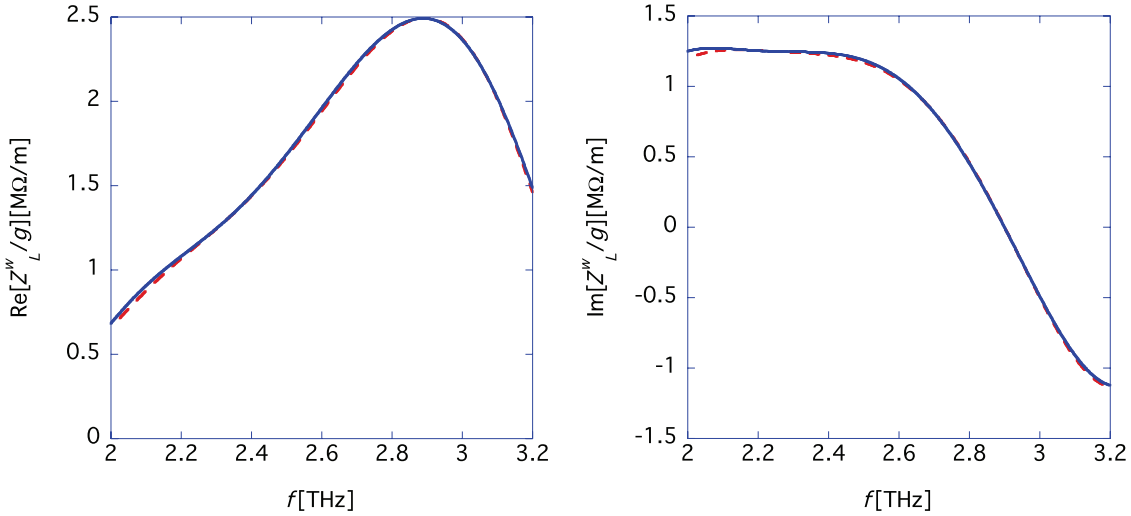

Fig. 24. The impedance Z_L^w with (red dashed) and without (blue) the effects of surface roughness and the misalignment of the positions of the chambers. The surface roughness is specified by $L_w = A_w = 0.100$ μm, and the misalignment errors are assumed to be 0.100 μm.

on the current simulation analysis, the misalignment shifts the characteristic impedance by about 0.1% from the ideal value. The simulation result is shown in Fig. 24, where the red and blue lines represent Z_L^w with and without the setup errors, respectively. We find that the difference between both results is tolerable even in the THz region by making both the amounts of surface roughness and the misalignment errors between the chambers be within 0.100 μm, so long as we deal with the impedance of the resistive insert with $\sigma_c = 187.566$ S/m.

Though the requirement for the setup error in this example may be achievable under the present technology [43,44], it depends on the amount of $|\sigma_c|$ in the THz region of the measured material. The resistive-wall impedance is roughly proportional to $1/\sqrt{\sigma_c}$ [11,41] for the material with higher conductivity. Therefore, if we measure the impedance Z_L^w with the conductivity $|\sigma_c| \gtrsim 10^4$ S/m at THz, the requirements for the measurement setup errors, including the surface roughness on the chambers and the misalignment between the chambers, become more stringent. For this case, Fig. 22 suggests that the errors must be below 0.010 μm or less, which is more challenging to realize.

Thus, when the target conductivity $|\sigma_c|$ is higher than 10^4 S/m at THz, we had better avoid blindly transforming the measured impedance Z_L^w to the conductivity σ_c. Instead, let us measure the surface roughness on the chambers in advance with other methods, e.g., scanning electron microscopy (SEM), energy dispersive spectroscopy (EDS), and atomic force microscopy (AFM) techniques [45]. After that, we should determine the frequency dependence of σ_c by reconstructing the measurements of impedance Z_L^w in combination with the independent measurements of the surface roughness via the simulation approach, as we discussed in Sect. 2.3.

6. Conclusions

The first step to calculating the resistive-wall beam impedance of a resistive chamber is determining the conductivity of the resistive material. The conductivity of the material at a given frequency can be evaluated by measuring the S-matrix of a propagation mode in a waveguide. However, in most cases, only the absolute value of the S-matrix is used for the evaluation, under the assumption that the conductivity is pure real, though both the S-matrix and the conductivity are complex numbers

in general. To evaluate complex conductivity from the measured complex S-matrix, we need a theoretical formula to connect them. To this end, we derived new theoretical formulae for the S-matrix in the TE_{11} and TM_{01} modes in a waveguide (waveguide method) and for a quasi-TEM_{00} mode in a coaxial waveguide (wire method), where complex conductivity was assumed. In all three cases, we confirmed that the theoretical formulae can reproduce the simulated S-matrices by CST Studio Suite 2018 very well for the assumed (constant and frequency-dependent complex) conductivities. Conversely, we can determine the conductivity of a material by using it as a fitting parameter in a comparison of a measured S-matrix with the theoretical formulae. The three independent methods facilitate a triple-check of the accuracy of the measured conductivity.

The standard log-formula (50) is often used to evaluate the resistive-wall beam impedance directly based on S-matrices measured using the wire method. Another method is evaluating the complex conductivity of the material based on the measured S-matrices and inputting it into the theoretical formula (51) for calculation of the resistive-wall beam impedance. We can estimate the accuracy of the standard log-formula by comparing the two results. We find that the standard log-formula reproduces the resistive-wall beam impedance well for the high-conductivity case, while it disagrees quantitatively in the low-conductivity case. For an accurate estimate of the resistive-wall beam impedance, using the theoretical formula (51) with the measured conductivity is preferable.

In the derivation of the above formulae, we have assumed that the outer surface of the resistive chamber is surrounded by a perfectly conductive layer, for simplicity. This approximation is valid in the high-frequency region, where the skin depth is smaller than the chamber width. However, our scheme can be easily generalized for low frequencies by removing the perfectly conductive layer and considering the analytical solutions outside the chamber, satisfying the open boundary conditions [4,11,33].

Acknowledgements

The author would like to thank Prof. Y. H. Chin for useful discussions and for encouraging the author to write this paper, as well as for careful reading of the manuscript.

Appendix A. Derivation of the scattering matrix by the waveguide method

In this appendix, we derive the formulae for the scattering matrix for the TE mode and the TM mode by using the waveguide method. We consider a 2D cylindrical chamber made of a resistive material with conductivity σ_c, whose inner radius is d and outer radius is a. Cylindrical coordinates (ρ, θ, z) are adopted for this description. We assume that the outer surface of the resistive chamber is surrounded by a perfectly conductive layer. All fields are proportional to $e^{j\omega t - j\Gamma z}$, where j is the imaginary unit and ω is the angular frequency. The factor Γ will be determined based on the boundary conditions.

A.1. Derivation of the scattering matrix for the TE_{11} mode in a cylindrical waveguide

First, let us calculate the scattering matrix for the TE_{11} mode, which is the lowest excitation mode in the cylindrical waveguide. The solutions of the Maxwell equations are expressed as

$$H_z = A\left[I_1(\kappa\rho) - \frac{I_1'(\kappa a)}{K_1'(\kappa a)}K_1(\kappa\rho)\right], \tag{A.1}$$

$$E_\theta = -\frac{jA\omega\mu_0}{\kappa}\left[I_1'(\kappa\rho) - \frac{I_1'(\kappa a)}{K_1'(\kappa a)}K_1'(\kappa\rho)\right], \tag{A.2}$$

$$H_\rho = \frac{jA\Gamma}{\kappa}\left[I_1'(\kappa\rho) - \frac{I_1'(\kappa a)}{K_1'(\kappa a)}K_1'(\kappa\rho)\right], \tag{A.3}$$

in the resistive material, and

$$H_z = BJ_1(\Lambda\rho), \tag{A.4}$$

$$E_\theta = -\frac{B\omega\mu_0}{j\sqrt{\frac{\omega^2}{c^2} - \Gamma^2}}J_1'(\Lambda\rho), \tag{A.5}$$

$$H_\rho = \frac{B\Gamma}{j\sqrt{\frac{\omega^2}{c^2} - \Gamma^2}}J_1'(\Lambda\rho), \tag{A.6}$$

in vacuum, where A and B are arbitrary coefficients. The functions $J_n(z)$ and $I_n(z), K_n(z)$ are the Bessel and modified Bessel functions, respectively [29]. The prime of the functions denotes the differential with respect to their arguments. The parameters μ_0 and σ_c are the permeability of vacuum and conductivity of the chamber, respectively. In addition, we define

$$\kappa = \sqrt{\Gamma^2 - \frac{\omega^2}{c^2} + j\omega\mu_0\sigma_c}, \tag{A.7}$$

and

$$\Lambda = \sqrt{\frac{\omega^2}{c^2} - \Gamma^2}. \tag{A.8}$$

The continuous condition of the fields at $\rho = d$ gives

$$A\left[I_1(\kappa d) - \frac{I_1'(\kappa a)}{K_1'(\kappa a)}K_1(\kappa d)\right] - BJ_1(\Lambda d) = 0, \tag{A.9}$$

$$\frac{A}{\kappa}\left[I_1'(\kappa d) - \frac{I_1'(\kappa a)}{K_1'(\kappa a)}K_1'(\kappa d)\right] + \frac{B}{\sqrt{\frac{\omega^2}{c^2} - \Gamma^2}}J_1'(\Lambda d) = 0, \tag{A.10}$$

which provide the eigenvalue condition for Γ:

$$\frac{[I_1(\kappa d) - \frac{I_1'(\kappa a)}{K_1'(\kappa a)}K_1(\kappa d)]J_1'(\Lambda d)}{\sqrt{\frac{\omega^2}{c^2} - \Gamma^2}} + \frac{1}{\kappa}\left[I_1'(\kappa d) - \frac{I_1'(\kappa a)}{K_1'(\kappa a)}K_1'(\kappa d)\right]J_1(\Lambda d) = 0, \tag{A.11}$$

so that Eqs. (A.9) and (A.10) have non-trivial solutions $\Gamma = \Gamma_{n,1}^{\mathrm{TE}}$, for a given frequency. Condition (A.11) is equivalent to Eq. (4) in the text. The lowest $n = 1$ solution corresponds to the TE_{11} mode case. Hereafter, we write $\kappa = \kappa_{1,1}$ corresponding to the lowest root of Eq. (A.11), i.e., $\Gamma_{1,1}^{\mathrm{TE}}$.

For the entire region of the resistive waveguide including the resistive material $0 \le \rho \le a$, the transverse fields of $\mathrm{TE}_{1,1}$ mode are summarized as

$$E_\theta = (B^+e^{-j\Gamma_{1,1}^{\mathrm{TE}}z} + B^-e^{j\Gamma_{1,1}^{\mathrm{TE}}z})\tilde{E}_\theta(\rho,\theta), \tag{A.12}$$

$$H_\rho = -\frac{(B^+e^{-j\Gamma_{1,1}^{\mathrm{TE}}z} - B^-e^{j\Gamma_{1,1}^{\mathrm{TE}}z})}{Z_{\mathrm{TE}_{1,1}}}\tilde{E}_\theta(\rho,\theta), \tag{A.13}$$

and

$$H_z = \frac{1}{Z_0}(B^+ e^{-j\Gamma^{\mathrm{TE}}_{1,1}z} + B^- e^{j\Gamma^{\mathrm{TE}}_{1,1}z})\tilde{H}_z, \tag{A.14}$$

where B^+ and B^- are arbitrary coefficients, $Z_0 = 120\pi\ \Omega$ is the impedance of free space,

$$\begin{aligned}\tilde{E}_\theta(\rho,\theta) = &-j\frac{\omega\mu_0[I_1'(\kappa_{1,1}d) - \frac{I_1'(\kappa_{1,1}a)}{K_1'(\kappa_{1,1}a)}K_1'(\kappa_{1,1}d)]J_1'(\sqrt{\frac{\omega^2}{c^2} - (\Gamma^{\mathrm{TE}}_{1,1})^2}\rho)}{\kappa_{1,1}J_1'(\sqrt{\frac{\omega^2}{c^2} - (\Gamma^{\mathrm{TE}}_{1,1})^2}d)}\\ &+j\frac{\omega\mu_0[I_1'(\kappa_{1,1}d) - \frac{I_1'(\kappa_{1,1}a)}{K_1'(\kappa_{1,1}a)}K_1'(\kappa_{1,1}d)]J_1'(\sqrt{\frac{\omega^2}{c^2} - (\Gamma^{\mathrm{TE}}_{1,1})^2}\rho)}{\kappa_{1,1}J_1'(\sqrt{\frac{\omega^2}{c^2} - (\Gamma^{\mathrm{TE}}_{1,1})^2}d)}\Theta(\rho - d)\\ &-j\frac{\omega\mu_0}{\kappa_{1,1}}[I_1'(\kappa_{1,1}\rho) - \frac{I_1'(\kappa_{1,1}a)}{K_1'(\kappa_{1,1}a)}K_1'(\kappa_{1,1}\rho)]\Theta(\rho - d),\end{aligned} \tag{A.15}$$

$$\begin{aligned}\tilde{H}_z = &Z_0[I_1(\kappa_{1,1}\rho) - \frac{I_1'(\kappa_{1,1}a)}{K_1'(\kappa_{1,1}a)}K_1(\kappa_{1,1}\rho)] - Z_0[I_1(\kappa_{1,1}\rho) - \frac{I_1'(\kappa_{1,1}a)}{K_1'(\kappa_{1,1}a)}K_1(\kappa_{1,1}\rho)]\Theta(\rho - d)\\ &+\frac{Z_0[I_1(\kappa_{1,1}d) - \frac{I_1'(\kappa_{1,1}a)}{K_1'(\kappa_{1,1}a)}K_1(\kappa_{1,1}d)]J_1(\sqrt{\frac{\omega^2}{c^2} - (\Gamma^{\mathrm{TE}}_{1,1})^2}\rho)}{J_1(\sqrt{\frac{\omega^2}{c^2} - (\Gamma^{\mathrm{TE}}_{1,1})^2}d)}\Theta(\rho - d),\end{aligned} \tag{A.16}$$

and

$$Z_{\mathrm{TE}_{1,1}} = \frac{\omega Z_0}{c\Gamma^{\mathrm{TE}}_{1,1}}. \tag{A.17}$$

The step function $\Theta(\rho)$ is defined as

$$\Theta(\rho) = \begin{cases} 1 & \text{for } \rho > 0,\\ \frac{1}{2} & \text{for } \rho = 0,\\ 0 & \text{for } \rho < 0.\end{cases} \tag{A.18}$$

Equations (A.12) and (A.13) lead to new formulae for the scattering matrix:

$$S_{11} = S_{22} = \frac{\frac{1}{Z_{50}^2} - \frac{1}{Z^2_{\mathrm{TE}_{1,1}}}}{\frac{1}{Z_{50}^2} + \frac{1}{Z^2_{\mathrm{TE}_{1,1}}} + \frac{2}{jZ_{50}Z_{\mathrm{TE}_{1,1}}\tan\Gamma^{\mathrm{TE}}_{1,1}g}}, \tag{A.19}$$

and

$$S_{21} = S_{12} = \frac{\frac{2}{jZ_{50}Z_{\mathrm{TE}_{1,1}}\sin\Gamma^{\mathrm{TE}}_{1,1}g}}{\frac{1}{Z_{50}^2} + \frac{1}{Z^2_{\mathrm{TE}_{1,1}}} + \frac{2}{jZ_{50}Z_{\mathrm{TE}_{1,1}}\tan\Gamma^{\mathrm{TE}}_{1,1}g}}, \tag{A.20}$$

by assuming that the waveguide impedance is $Z_{\mathrm{TE}_{1,1}}$, where g is the total length of the waveguide chamber, and both ends of the waveguide are connected to cables with characteristic impedance Z_{50} (which is typically 50 Ω). Equations (A.19) and (A.20) are equivalent to formulae (1) and (2) in the text.

A.2. Formalism of the scattering matrix for the TM_{0n} mode using the waveguide method

Next, we derive the formulae for the scattering matrix for the TM_{0n} mode. Compared to the TE_{11} mode case, it is not straightforward to obtain the formulae for the scattering matrix for this mode in a resistive waveguide. Here, we start with derivation of the waveguide voltage and current for the cylindrical waveguide, following the general formalism in Ref. [46].

The dielectric constant $\epsilon(\rho,\theta)$ and the magnetic permeability μ of the waveguide in the entire region are summarized as

$$\epsilon(\rho,\theta) = \epsilon_0 + \frac{\sigma_c}{j\omega}\Theta(\rho - d), \tag{A.21}$$

$$\mu = \mu_0, \tag{A.22}$$

by using the step function $\Theta(x)$ defined in Eq. (A.18), where ϵ_0 is the dielectric constant of vacuum.

The fields $\vec{E}$ and $\vec{H}$ for the mode are described as

$$\vec{E} = (\tilde{E}_\rho(\rho,\theta)\vec{e}_\rho + \tilde{E}_\theta(\rho,\theta)\vec{e}_\theta)V(z) + Z_0\tilde{E}_z(\rho,\theta)\vec{e}_z I(z), \tag{A.23}$$

and

$$\vec{H} = (\tilde{H}_\rho(\rho,\theta)\vec{e}_\rho + \tilde{H}_\theta(\rho,\theta)\vec{e}_\theta)I(z) + \frac{1}{Z_0}\tilde{H}_z(\rho,\theta)\vec{e}_z V(z), \tag{A.24}$$

by introducing the fields $\tilde{E}_\rho$, $\tilde{E}_\theta$, $\tilde{E}_z$, $\tilde{H}_\rho$, $\tilde{H}_\theta$, $\tilde{H}_z$, the waveguide voltage $V(z)$, and the waveguide current $I(z)$, where $\vec{e}_\rho, \vec{e}_\theta$, and $\vec{e}_z$ are the unit vectors in the ρ-, θ-, and z-directions, respectively.

The Maxwell equation $\nabla \times \vec{E} = -j\omega\mu\vec{H}$ is expressed using their components,

$$\frac{Z_0}{\rho\tilde{E}_\theta(\rho,\theta)}\frac{\partial\tilde{E}_z(\rho,\theta)}{\partial\theta} + j\omega\mu\frac{\tilde{H}_\rho(\rho,\theta)}{\tilde{E}_\theta(\rho,\theta)} = \frac{1}{I(z)}\frac{\partial V(z)}{\partial z}, \tag{A.25}$$

$$\frac{Z_0}{\tilde{E}_\rho(\rho,\theta)}\frac{\partial\tilde{E}_z(\rho,\theta)}{\partial\rho} - j\omega\mu\frac{\tilde{H}_\theta(\rho,\theta)}{\tilde{E}_\rho(\rho,\theta)} = \frac{1}{I(z)}\frac{\partial V(z)}{\partial z}, \tag{A.26}$$

$$\frac{1}{\rho}\frac{\partial}{\partial\rho}(\rho\tilde{E}_\theta(\rho,\theta)) - \frac{1}{\rho}\frac{\partial\tilde{E}_\rho(\rho,\theta)}{\partial\theta} + j\frac{\omega}{c}\tilde{H}_z(\rho,\theta) = 0, \tag{A.27}$$

for $I(z) \neq 0$ and $V(z) \neq 0$, which produces

$$\frac{1}{I(z)}\frac{dV(z)}{dz} = -j\Gamma Z_c', \tag{A.28}$$

$$\nabla \times \tilde{E}_z(\rho,\theta)\vec{e}_z = -j\frac{\omega}{c}(\tilde{H}_\rho(\rho,\theta)\vec{e}_\rho + \tilde{H}_\theta(\rho,\theta)\vec{e}_\theta) + j\Gamma\frac{Z_c'}{Z_0}\vec{e}_z \times (\tilde{E}_\rho(\rho,\theta)\vec{e}_\rho + \tilde{E}_\theta(\rho,\theta)\vec{e}_\theta), \tag{A.29}$$

$$\nabla \times (\tilde{E}_\rho(\rho,\theta)\vec{e}_\rho + \tilde{E}_\theta(\rho,\theta)\vec{e}_\theta) = -j\frac{\omega}{c}\tilde{H}_z(\rho,\theta)\vec{e}_z, \tag{A.30}$$

while the other equation $\nabla \times \vec{H} = j\omega\epsilon\vec{E}$ can be written using their components,

$$\frac{1}{Z_0\rho\tilde{H}_\theta(\rho,\theta)}\frac{\partial\tilde{H}_z(\rho,\theta)}{\partial\theta} - j\omega\epsilon(\rho,\theta)\frac{\tilde{E}_\rho(\rho,\theta)}{\tilde{H}_\theta(\rho,\theta)} = \frac{1}{V(z)}\frac{\partial I(z)}{\partial z}, \tag{A.31}$$

$$\frac{1}{Z_0\tilde{H}_\rho(\rho,\theta)}\frac{\partial\tilde{H}_z(\rho,\theta)}{\partial\rho} + j\omega\epsilon(\rho,\theta)\frac{\tilde{E}_\theta(\rho,\theta)}{\tilde{H}_\rho(\rho,\theta)} = \frac{1}{V(z)}\frac{\partial I(z)}{\partial z}, \tag{A.32}$$

$$\frac{1}{\rho}\frac{\partial}{\partial\rho}(\rho\tilde{H}_\theta(\rho,\theta)) - \frac{1}{\rho}\frac{\partial\tilde{H}_\rho(\rho,\theta)}{\partial\theta} - j\omega\epsilon(\rho,\theta)Z_0\tilde{E}_z(\rho,\theta) = 0, \tag{A.33}$$

for $I(z) \neq 0$ and $V(z) \neq 0$, which provides

$$\frac{1}{V(z)}\frac{\partial I(z)}{\partial z} = -\frac{j\Gamma}{Z_c'}, \tag{A.34}$$

$$\nabla\times\tilde{H}_z\vec{e}_z = j\omega\epsilon(\rho,\theta)Z_0(\tilde{E}_\rho(\rho,\theta)\vec{e}_\rho + \tilde{E}_\theta(\rho,\theta)\vec{e}_\theta) + \frac{j\Gamma Z_0}{Z_c'}\vec{e}_z\times(\tilde{H}_\rho(\rho,\theta)\vec{e}_\rho + \tilde{H}_\theta(\rho,\theta)\vec{e}_\theta), \tag{A.35}$$

$$\nabla\times(\tilde{H}_\rho(\rho,\theta)\vec{e}_\rho + \tilde{H}_\theta(\rho,\theta)\vec{e}_\theta) = j\omega\epsilon(\rho,\theta)Z_0\tilde{E}_z(\rho,\theta)\vec{e}_z, \tag{A.36}$$

where the waveguide impedance Z_c' is introduced formally.

Here, the average power is defined by

$$\begin{aligned} P(z) &= \frac{1}{2}\int d\theta d\rho\rho(E_\rho H_\theta^* - E_\theta H_\rho^*) \\ &= \frac{1}{2}\int d\theta d\rho\rho(\tilde{E}_\rho(\rho,\theta)\tilde{H}_\theta^*(\rho,\theta) - \tilde{E}_\theta(\rho,\theta)\tilde{H}_\rho^*(\rho,\theta))V(z)I^*(z), \end{aligned} \tag{A.37}$$

where "*" denotes a complex conjugate. In the transmission line model, the same average power is given by

$$P(z) = \frac{1}{2}V(z)I^*(z), \tag{A.38}$$

by using the waveguide voltage and the waveguide current. Accordingly, we obtain the requirement for the fields as

$$\int d\theta d\rho\rho(\tilde{E}_\rho(\rho,\theta)\tilde{H}_\theta^*(\rho,\theta) - \tilde{E}_\theta(\rho,\theta)\tilde{H}_\rho^*(\rho,\theta)) = 1. \tag{A.39}$$

By combining Eq. (A.30) with Eq. (A.35), we obtain

$$\begin{aligned} &-\vec{e}_z\times(\tilde{H}_\rho(\rho,\theta)\vec{e}_\rho + \tilde{H}_\theta(\rho,\theta)\vec{e}_\theta) = \tilde{H}_\theta(\rho,\theta)\vec{e}_\rho - \tilde{H}_\rho(\rho,\theta)\vec{e}_\theta \\ &= \frac{1}{j\omega}\frac{Z_c'}{j\Gamma}\left\{\frac{c}{Z_0}\nabla\times[\nabla\times(\tilde{E}_\rho(\rho,\theta)\vec{e}_\rho + \tilde{E}_\theta(\rho,\theta)\vec{e}_\theta)] - \omega^2\epsilon(\rho,\theta)(\tilde{E}_\rho(\rho,\theta)\vec{e}_\rho + \tilde{E}_\theta(\rho,\theta)\vec{e}_\theta)\right\}. \end{aligned} \tag{A.40}$$

Subsequently, by substituting Eq. (A.40) into Eq. (A.39), Eq. (A.39) is rewritten as

$$\begin{aligned} &\frac{1}{j\omega}\frac{Z_c'^*}{j\Gamma^*}\int d\theta d\rho\rho(\tilde{E}_\rho(\rho,\theta)\vec{e}_\rho + \tilde{E}_\theta(\rho,\theta)\vec{e}_\theta)\cdot \\ &\left\{\frac{c}{Z_0}\nabla\times[\nabla\times(\tilde{E}_\rho(\rho,\theta)\vec{e}_\rho + \tilde{E}_\theta(\rho,\theta)\vec{e}_\theta)] - \omega^2\epsilon(\rho,\theta)(\tilde{E}_\rho(\rho,\theta)\vec{e}_\rho + \tilde{E}_\theta(\rho,\theta)\vec{e}_\theta)\right\}^* = 1. \end{aligned} \tag{A.41}$$

Because the original electric field is described by Eq. (A.23), the waveguide voltage $V(z)$ is expressed as

$$V(z) = \frac{1}{j\omega}\frac{Z_c'^*}{j\Gamma^*}\int d\theta d\rho\rho\vec{E}\cdot$$

$$\left\{\frac{c}{Z_0}\nabla\times[\nabla\times(\tilde{E}_\rho(\rho,\theta)\vec{e}_\rho+\tilde{E}_\theta(\rho,\theta)\vec{e}_\theta)]-\omega^2\epsilon(\rho,\theta)(\tilde{E}_\rho(\rho,\theta)\vec{e}_\rho+\tilde{E}_\theta(\rho,\theta)\vec{e}_\theta)\right\}^*. \quad \text{(A.42)}$$

Here, we have used the fact that the right-hand side of Eq. (A.40) has no $\vec{e}_z$-component.

Similarly, by combining Eqs. (A.29) and (A.36), we obtain

$$\vec{e}_z\times(\tilde{E}_\rho(\rho,\theta)\vec{e}_\rho+\tilde{E}_\theta(\rho,\theta)\vec{e}_\theta)=-\tilde{E}_\theta(\rho,\theta)\vec{e}_\rho+\tilde{E}_\rho(\rho,\theta)\vec{e}_\theta$$
$$=\frac{1}{j\omega j\Gamma Z_c'}\left\{\nabla\times[\frac{1}{\epsilon(\rho,\theta)}\nabla\times(\tilde{H}_\rho(\rho,\theta)\vec{e}_\rho+\tilde{H}_\theta(\rho,\theta)\vec{e}_\theta)]-\frac{\omega^2Z_0}{c}(\tilde{H}_\rho(\rho,\theta)\vec{e}_\rho+\tilde{H}_\theta(\rho,\theta)\vec{e}_\theta)\right\}. \quad \text{(A.43)}$$

By substituting Eq. (A.43) into Eq. (A.39), the complex conjugate of Eq. (A.39) is written as

$$\frac{1}{j\omega j\Gamma^* Z_c'^*}\int d\theta d\rho\rho(\tilde{H}_\rho(\rho,\theta)\vec{e}_\rho+\tilde{H}_\theta(\rho,\theta)\vec{e}_\theta)\cdot$$
$$\left\{\nabla\times[\frac{1}{\epsilon(\rho,\theta)}\nabla\times(\tilde{H}_\rho(\rho,\theta)\vec{e}_\rho+\tilde{H}_\theta(\rho,\theta)\vec{e}_\theta)]-\frac{\omega^2Z_0}{c}(\tilde{H}_\rho(\rho,\theta)\vec{e}_\rho+\tilde{H}_\theta(\rho,\theta)\vec{e}_\theta)\right\}^*=1. \quad \text{(A.44)}$$

Finally, the waveguide current $I(z)$ is expressed as

$$I(z)=\frac{1}{j\omega j\Gamma^* Z_c'^*}\int d\theta d\rho\rho\vec{H}\cdot$$
$$\left\{\nabla\times[\frac{1}{\epsilon(\rho,\theta)}\nabla\times(\tilde{H}_\rho(\rho,\theta)\vec{e}_\rho+\tilde{H}_\theta(\rho,\theta)\vec{e}_\theta)]-\frac{\omega^2Z_0}{c}(\tilde{H}_\rho(\rho,\theta)\vec{e}_\rho+\tilde{H}_\theta(\rho,\theta)\vec{e}_\theta)\right\}^*. \quad \text{(A.45)}$$

By partially integrating Eq. (A.44) and using the boundary condition on the surface of the chamber ($E_z=0$), the complex conjugate of Eq. (A.44) produces the waveguide impedance Z_c':

$$Z_c'=\frac{\omega}{\Gamma}\int d\theta d\rho\rho\left[-(\epsilon_0+\frac{j\Re[\sigma_c]+\Im[\sigma_c]}{\omega}\Theta(\rho-d))Z_0^2|\tilde{E}_z|^2+\frac{Z_0}{c}(|\tilde{H}_\rho|^2+|\tilde{H}_\theta|^2)\right], \quad \text{(A.46)}$$

for the mode Γ.

A.2.1. Scattering matrix for the TM_{0n} mode using the waveguide method

The solutions of the Maxwell equations for the TM_{0n} mode in the cylindrical waveguide are generally expressed as

$$E_z=A_{\rm TM}\left[I_0(\kappa\rho)-\frac{I_0(\kappa a)}{K_0(\kappa a)}K_0(\kappa\rho)\right], \quad \text{(A.47)}$$
$$H_\theta=\frac{A_{\rm TM}(\sigma_c+j\omega\epsilon_0)}{\sqrt{\Gamma^2-\frac{\omega^2}{c^2}+j\omega\mu_0\sigma_c}}\left[I_1(\kappa\rho)+\frac{I_0(\kappa a)}{K_0(\kappa a)}K_1(\kappa\rho)\right], \quad \text{(A.48)}$$
$$E_\rho=\frac{A_{\rm TM}j\Gamma}{\sqrt{\Gamma^2-\frac{\omega^2}{c^2}+j\omega\mu_0\sigma_c}}\left[I_1(\kappa\rho)+\frac{I_0(\kappa a)}{K_0(\kappa a)}K_1(\kappa\rho)\right], \quad \text{(A.49)}$$

for the resistive material, and

$$E_z=B_{\rm TM}J_0(\Lambda\rho), \quad \text{(A.50)}$$

$$H_\theta = -\frac{B_{\mathrm{TM}}\omega\epsilon_0}{j\Lambda}J_1(\Lambda\rho), \tag{A.51}$$

$$E_\rho = -\frac{B_{\mathrm{TM}}\Gamma}{j\Lambda}J_1(\Lambda\rho), \tag{A.52}$$

for vacuum, respectively, where A_{TM} and B_{TM} are arbitrary coefficients, and κ and Λ are defined by Eqs. (A.7) and (A.8), respectively,

The continuous condition of the fields at $\rho = d$ gives

$$A_{\mathrm{TM}}[I_0(\kappa d) - \frac{I_0(\kappa a)}{K_0(\kappa a)}K_0(\kappa d)] - B_{\mathrm{TM}}J_0(\Lambda d) = 0, \tag{A.53}$$

and

$$\frac{A_{\mathrm{TM}}(\sigma_c + j\omega\epsilon_0)}{\sqrt{\Gamma^2 - \frac{\omega^2}{c^2} + j\omega\mu_0\sigma_c}}[I_1(\kappa d) + \frac{I_0(\kappa a)}{K_0(\kappa a)}K_1(\kappa d)] + \frac{B_{\mathrm{TM}}\omega\epsilon_0}{j\Lambda}J_1(\Lambda d) = 0, \tag{A.54}$$

which produces

$$\frac{\omega\epsilon_0[I_0(\kappa d) - \frac{I_0(\kappa a)}{K_0(\kappa a)}K_0(\kappa d)]J_1(\Lambda d)}{j\Lambda} + \frac{(\sigma_c + j\omega\epsilon_0)J_0(\Lambda d)[I_1(\kappa d) + \frac{I_0(\kappa a)}{K_0(\kappa a)}K_1(\kappa d)]}{\sqrt{\Gamma^2 - \frac{\omega^2}{c^2} + j\omega\mu_0\sigma_c}} = 0, \tag{A.55}$$

such that Eqs. (A.53) and (A.54) have non-trivial solutions $\Gamma^{\mathrm{TM}}_{n,0}$. The lowest $n = 1$ solution corresponds to the TM_{01} mode case. Especially when $\sigma_c = 0$ S/m, Eq. (A.55) reproduces

$$J_0(\Lambda a) = 0, \tag{A.56}$$

which is the eigenvalue condition for the TM_{0n} mode in a perfectly conductive waveguide with the inner radius a [28].

Hereafter, we write $\kappa = \kappa_{n,0}$, and

$$\Lambda = \Lambda_{\mathrm{TM}} = \left(\frac{\omega^2}{c^2} - (\Gamma^{\mathrm{TM}}_{n,0})^2\right)^{\frac{1}{2}}, \tag{A.57}$$

for the nth root $\Gamma_{n,0}$ of Eq. (A.55). The transverse ($\tilde{E}_\rho, \tilde{H}_\theta$) and the longitudinal ($\tilde{E}_z$) fields are defined as

$$\begin{aligned}\tilde{E}_\rho = &-\frac{cj_{0,n}Z_0\Gamma^{\mathrm{TM}}_{n,0}J_1(\Lambda_{\mathrm{TM}}\rho)}{jZ'_c\Lambda_{\mathrm{TM}}\sqrt{\pi}\omega a^2J_1(j_{0,n})} + \frac{cj_{0,n}Z_0\Gamma^{\mathrm{TM}}_{n,0}J_1(\Lambda_{\mathrm{TM}}\rho)}{jZ'_c\Lambda_{\mathrm{TM}}\sqrt{\pi}\omega a^2J_1(j_{0,n})}\Theta(\rho - d)\\ &- \frac{cj_{0,n}\epsilon_0Z_0\Gamma^{\mathrm{TM}}_{n,0}J_1(\Lambda_{\mathrm{TM}}d)[I_1(\kappa_{n,0}\rho) + \frac{I_0(\kappa_{n,0}a)}{K_0(\kappa_{n,0}a)}K_1(\kappa_{n,0}\rho)]}{Z'_c\sqrt{\pi}a^2J_1(j_{0,n})(\sigma_c + j\omega\epsilon_0)\Lambda_{\mathrm{TM}}[I_1(\kappa_{n,0}d) + \frac{I_0(\kappa_{n,0}a)}{K_0(\kappa_{n,0}a)}K_1(\kappa_{n,0}d)]}\Theta(\rho - d),\end{aligned} \tag{A.58}$$

$$\begin{aligned}\tilde{H}_\theta = &-\frac{j_{0,n}J_1(\Lambda_{\mathrm{TM}}\rho)}{j\Lambda_{\mathrm{TM}}\sqrt{\pi}a^2J_1(j_{0,n})} + \frac{j_{0,n}J_1(\Lambda_{\mathrm{TM}}\rho)}{j\Lambda_{\mathrm{TM}}\sqrt{\pi}a^2J_1(j_{0,n})}\Theta(\rho - d)\\ &- \frac{j_{0,n}J_1(\Lambda_{\mathrm{TM}}d)[I_1(\kappa_{n,0}\rho) + \frac{I_0(\kappa_{n,0}a)}{K_0(\kappa_{n,0}a)}K_1(\kappa_{n,0}\rho)]}{j\Lambda_{\mathrm{TM}}\sqrt{\pi}a^2J_1(j_{0,n})[I_1(\kappa_{n,0}d) + \frac{I_0(\kappa_{n,0}a)}{K_0(\kappa_{n,0}a)}K_1(\kappa_{n,0}d)]}\Theta(\rho - d),\end{aligned} \tag{A.59}$$

$$\tilde{E}_z = \frac{cj_{0,n}J_0(\Lambda_{\rm TM}\rho)}{\sqrt{\pi}\omega a^2 J_1(j_{0,n})} - \frac{cj_{0,n}J_0(\Lambda_{\rm TM}\rho)}{\sqrt{\pi}\omega a^2 J_1(j_{0,n})}\Theta(\rho - d) + \frac{cj_{0,n}J_0(\Lambda_{\rm TM}d)(I_0(\kappa_{n,0}\rho) - \frac{I_0(\kappa_{n,0}a)}{K_0(\kappa_{n,0}a)}K_0(\kappa_{n,0}\rho))}{\sqrt{\pi}\omega a^2 J_1(j_{0,n})(I_0(\kappa_{n,0}d) - \frac{I_0(\kappa_{n,0}a)}{K_0(\kappa_{n,0}a)}K_0(\kappa_{n,0}d))}\Theta(\rho - d), \tag{A.60}$$

such that they are the solutions of Eqs. (A.29) and (A.36), i.e.,

$$\frac{1}{\rho}\frac{\partial}{\partial\rho}(\rho\tilde{H}_\theta) = j\omega\epsilon_0 Z_0\tilde{E}_z, \tag{A.61}$$

$$-\frac{\partial\tilde{E}_z}{\partial\rho} = -j\frac{\omega}{c}\tilde{H}_\theta + j\Gamma\frac{Z_c'}{Z_0}\tilde{E}_\rho. \tag{A.62}$$

By using Eqs. (A.42), (A.45), and (A.46), the waveguide voltage $V(z)$ and the waveguide current $I(z)$ are calculated as

$$V(z) = C_V(B^+_{\rm TM}e^{-j\Gamma^{\rm TM}_{n,0}z} + B^-_{\rm TM}e^{j\Gamma^{\rm TM}_{n,0}z}), \tag{A.63}$$

$$I(z) = C_I(B^+_{\rm TM}e^{-j\Gamma^{\rm TM}_{n,0}z} - B^-_{\rm TM}e^{j\Gamma^{\rm TM}_{n,0}z}), \tag{A.64}$$

where $B^+_{\rm TM}$ and $B^-_{\rm TM}$ are arbitrary coefficients,

$$\tilde{B} = B_{\rm TM}\frac{\sqrt{\pi}\omega a^2 J_1(j_{0,n})}{cj_{0,n}Z_0}, \tag{A.65}$$

$$\begin{aligned}
C_I &= \frac{2\pi\tilde{B}}{\omega\Gamma^{\rm TM*}_{n,0}Z_c'^*}\int_0^a d\rho\rho\tilde{H}_\theta(\rho,\theta)\left[\frac{\partial}{\partial\rho}\frac{1}{\epsilon(\rho,\theta)}\frac{1}{\rho}\frac{\partial}{\partial\rho}\rho\tilde{H}_\theta(\rho,\theta) + \frac{\omega^2 Z_0}{c}\tilde{H}_\theta(\rho,\theta)\right]^* \\
&= \frac{2\pi\tilde{B}}{\omega\Gamma^{\rm TM*}_{n,0}Z_c'^*}\left[\rho\tilde{H}_\theta(\rho,\theta)\frac{1}{\epsilon^*(\rho,\theta)}\frac{1}{\rho}\frac{\partial}{\partial\rho}\rho\tilde{H}^*_\theta(\rho,\theta)\Big|_0^a\right. \\
&\quad \left. + \int_0^a d\rho\left(-\frac{\partial\rho\tilde{H}_\theta(\rho,\theta)}{\partial\rho}\frac{1}{\epsilon^*(\rho,\theta)}\frac{1}{\rho}\frac{\partial}{\partial\rho}\rho\tilde{H}^*_\theta(\rho,\theta) + \rho\tilde{H}_\theta(\rho,\theta)\frac{\omega^2 Z_0}{c}\tilde{H}^*_\theta(\rho,\theta)\right)\right] \\
&= \frac{2j^2_{0,n}\tilde{B}}{\omega\Gamma^{\rm TM*}_{n,0}Z_c'^* a^4 J_1^2(j_{0,n})}\left\{-\frac{cZ_0(\Im[\Lambda_{\rm TM}dJ_0(\Lambda^*_{\rm TM}d)J_1(\Lambda_{\rm TM}d)] - \frac{\omega^2\Im[\Lambda^*_{\rm TM}dJ_0(\Lambda^*_{\rm TM}d)J_1(\Lambda_{\rm TM}d)]}{c^2|\Lambda_{\rm TM}|^2})}{\Im[\Lambda^2_{\rm TM}]}\right. \\
&\quad - \frac{|J_1(\Lambda_{\rm TM}d)|^2}{(\epsilon_0 - \frac{\sigma^*_c}{j\omega})|I_1(\kappa_{n,0}d) + \frac{I_0(\kappa_{n,0}a)}{K_0(\kappa_{n,0}a)}K_1(\kappa_{n,0}d)|^2} \\
&\quad \times\left(\frac{\Im[\kappa_{n,0}aI_0(\kappa^*_{n,0}a)I_1(\kappa_{n,0}a) - \kappa_{n,0}dI_0(\kappa^*_{n,0}d)I_1(\kappa_{n,0}d)]}{\Im[\kappa^2_{n,0}]}\right. \\
&\quad - 2\Re\left[\frac{\frac{I_0(\kappa^*_{n,0}a)}{K_0(\kappa^*_{n,0}a)}(\kappa_{n,0}aI_1(\kappa_{n,0}a)K_0(\kappa^*_{n,0}a) + \kappa^*_{n,0}aI_0(\kappa_{n,0}a)K_1(\kappa^*_{n,0}a))}{(\kappa^2_{n,0} - \kappa^{*2}_{n,0})}\right. \\
&\quad \left.\left.\left.\left. - \frac{\frac{I_0(\kappa^*_{n,0}a)}{K_0(\kappa^*_{n,0}a)}(\kappa_{n,0}dI_1(\kappa_{n,0}d)K_0(\kappa^*_{n,0}d) + \kappa^*_{n,0}dI_0(\kappa_{n,0}d)K_1(\kappa^*_{n,0}d))}{(\kappa^2_{n,0} - \kappa^{*2}_{n,0})}\right]\right.\right.\right.
\end{aligned}$$

$$
\left.-\frac{|I_0(\kappa_{n,0}a)|^2\Im[\kappa_{n,0}aK_0(\kappa_{n,0}^*a)K_1(\kappa_{n,0}a)-\kappa_{n,0}dK_0(\kappa_{n,0}^*d)K_1(\kappa_{n,0}d)]}{|K_0(\kappa_{n,0}a)|^2\Im[\kappa_{n,0}^2]}\right)
$$

$$
+\frac{\omega^2 Z_0|J_1(\Lambda_{\rm TM}d)|^2}{c|\Lambda_{\rm TM}|^2|I_1(\kappa_{n,0}d)+\frac{I_0(\kappa_{n,0}a)}{K_0(\kappa_{n,0}a)}K_1(\kappa_{n,0}d)|^2}
$$

$$
\times\left(\frac{\Im[\kappa_{n,0}aI_1(\kappa_{n,0}^*a)I_2(\kappa_{n,0}a)-\kappa_{n,0}dI_1(\kappa_{n,0}^*d)I_2(\kappa_{n,0}d)]}{\Im[\kappa_{n,0}^2]}\right.
$$

$$
+2\Re\left[\frac{\frac{I_0(\kappa_{n,0}^*a)}{K_0(\kappa_{n,0}^*a)}(\kappa_{n,0}aI_2(\kappa_{n,0}a)K_1(\kappa_{n,0}^*a)+\kappa_{n,0}^*aI_1(\kappa_{n,0}a)K_2(\kappa_{n,0}^*a))}{(\kappa_{n,0}^2-\kappa_{n,0}^{*2})}\right.
$$

$$
\left.\left.-\frac{\frac{I_0(\kappa_{n,0}^*a)}{K_0(\kappa_{n,0}^*a)}(\kappa_{n,0}dI_2(\kappa_{n,0}d)K_1(\kappa_{n,0}^*d)+\kappa_{n,0}^*dI_1(\kappa_{n,0}d)K_2(\kappa_{n,0}^*d))}{(\kappa_{n,0}^2-\kappa_{n,0}^{*2})}\right]\right.
$$

$$
\left.\left.+\frac{|I_0(\kappa_{n,0}a)|^2\Im[\kappa_{n,0}^*(aK_0(\kappa_{n,0}^*a)K_1(\kappa_{n,0}a)-dK_0(\kappa_{n,0}^*d)K_1(\kappa_{n,0}d)])}{|K_0(\kappa_{n,0}a)|^2\Im[\kappa_{n,0}^2]}\right)\right\}, \tag{A.66}
$$

$$
\begin{aligned}
C_V &= \tilde{B}\left[\frac{2\pi\omega\epsilon_0 Z_c' Z_c'^*}{\Gamma_{n,0}^{*TM}}\int_0^d d\rho\rho|\tilde{E}_\rho|^2+\frac{2\pi\omega(\epsilon_0-\frac{\sigma_c^*}{j\omega})Z_c' Z_c'^*}{\Gamma_{n,0}^{*TM}}\int_d^a d\rho\rho|\tilde{E}_\rho|^2\right]\\
&= \tilde{B}\frac{2j_{0,n}^2|\Gamma_{n,0}^{\rm TM}|^2}{a^4J_1^2(j_{0,n})\Gamma_{n,0}^{*TM}|\Lambda_{\rm TM}|^2}\left[\frac{cZ_0\Im[\Lambda_{\rm TM}^*dJ_0(\Lambda_{\rm TM}^*d)J_1(\Lambda_{\rm TM}d)]}{\omega\Im[\Lambda_{\rm TM}^2]}\right.\\
&\quad+\frac{\omega(\epsilon_0-\frac{\sigma_c^*}{j\omega})|J_1(\Lambda_{\rm TM}d)|^2}{|\sigma_c+j\omega\epsilon_0|^2|I_1(\kappa_{n,0}d)+\frac{I_0(\kappa_{n,0}a)}{K_0(\kappa_{n,0}a)}K_1(\kappa_{n,0}d)|^2}\\
&\quad\times\left\{\frac{\Im[\kappa_{n,0}aI_1(\kappa_{n,0}^*a)I_2(\kappa_{n,0}a)-\kappa_{n,0}dI_1(\kappa_{n,0}^*d)I_2(\kappa_{n,0}d)]}{\Im[\kappa_{n,0}^2]}\right.\\
&\quad-2\Re\left[\frac{a\frac{I_0(\kappa_{n,0}a)}{K_0(\kappa_{n,0}a)}(\kappa_{n,0}^*I_2(\kappa_{n,0}^*a)K_1(\kappa_{n,0}a)+\kappa_{n,0}I_1(\kappa_{n,0}^*a)K_2(\kappa_{n,0}a))}{(\kappa_{n,0}^2-\kappa_{n,0}^{*2})}\right.\\
&\quad\left.-\frac{d\frac{I_0(\kappa_{n,0}a)}{K_0(\kappa_{n,0}a)}(\kappa_{n,0}^*I_2(\kappa_{n,0}^*d)K_1(\kappa_{n,0}d)+\kappa_{n,0}I_1(\kappa_{n,0}^*d)K_2(\kappa_{n,0}d))}{(\kappa_{n,0}^2-\kappa_{n,0}^{*2})}\right]\\
&\quad\left.\left.+\frac{|I_0(\kappa_{n,0}a)|^2\Im[\kappa_{n,0}^*(aK_0(\kappa_{n,0}^*a)K_1(\kappa_{n,0}a)-dK_0(\kappa_{n,0}^*d)K_1(\kappa_{n,0}d)])}{|K_0(\kappa_{n,0}a)|^2\Im[\kappa_{n,0}^2]}\right\}\right],
\end{aligned} \tag{A.67}
$$

$$
\begin{aligned}
Z_c' &= \frac{\omega}{\Gamma_{n,0}^{\rm TM}}\int d\theta d\rho\rho\left[-\left(\epsilon_0+\frac{j\sigma_c^*}{\omega}\Theta(\rho-d)\right)Z_0^2|\tilde{E}_z|^2+\frac{Z_0}{c}|\tilde{H}_\theta|^2\right]\\
&= \frac{2j_{0,n}^2c^2Z_0^2}{\omega\Gamma_{n,0}^{\rm TM}a^4J_1^2(j_{0,n})}\left\{-\frac{\Im[\Lambda_{\rm TM}dJ_0(\Lambda_{\rm TM}^*d)J_1(\Lambda_{\rm TM}d)]}{cZ_0\Im[\Lambda_{\rm TM}^2]}+\frac{\omega^2\Im[\Lambda_{\rm TM}^*dJ_0(\Lambda_{\rm TM}^*d)J_1(\Lambda_{\rm TM}d)]}{c^3Z_0|\Lambda_{\rm TM}|^2\Im[\Lambda_{\rm TM}^2]}\right.
\end{aligned}
$$

$$
\begin{aligned}
&- \left(\epsilon_0 + \frac{j\sigma_c^*}{\omega}\right) \frac{|J_0(\Lambda_{\mathrm{TM}} d)|^2}{|I_0(\kappa_{n,0} d) - \frac{I_0(\kappa_{n,0} a)}{K_0(\kappa_{n,0} a)} K_0(\kappa_{n,0} d)|^2} \\
&\times \left\{ \frac{\Im[\kappa_{n,0} a I_0(\kappa_{n,0}^* a) I_1(\kappa_{n,0} a) - \kappa_{n,0} d I_0(\kappa_{n,0}^* d) I_1(\kappa_{n,0} d)]}{\Im[\kappa_{n,0}^2]} \right. \\
&- 2\Re\left[\frac{I_0(\kappa_{n,0} a)}{K_0(\kappa_{n,0} a)} \left(- \frac{a(\kappa_{n,0}^* I_1(\kappa_{n,0}^* a) K_0(\kappa_{n,0} a) + \kappa_{n,0} I_0(\kappa_{n,0}^* a) K_1(\kappa_{n,0} a))}{(\kappa_{n,0}^2 - \kappa_{n,0}^{*2})} \right.\right. \\
&\left.\left. + \frac{d(\kappa_{n,0}^* I_1(\kappa_{n,0}^* d) K_0(\kappa_{n,0} d) + \kappa_{n,0} I_0(\kappa_{n,0}^* d) K_1(\kappa_{n,0} d))}{(\kappa_{n,0}^2 - \kappa_{n,0}^{*2})} \right) \right] \\
&\left. - \frac{|I_0(\kappa_{n,0} a)|^2 \Im[\kappa_{n,0}(a K_0(\kappa_{n,0}^* a) K_1(\kappa_{n,0} a) - d K_0(\kappa_{n,0}^* d) K_1(\kappa_{n,0} d))]}{|K_0(\kappa_{n,0} a)|^2 \Im[\kappa_{n,0}^2]} \right\} \\
&+ \frac{\omega^2 |J_1(\Lambda_{\mathrm{TM}} d)|^2}{c^3 Z_0 |\Lambda_{\mathrm{TM}}|^2 |I_1(\kappa_{n,0} d) + \frac{I_0(\kappa_{n,0} a)}{K_0(\kappa_{n,0} a)} K_1(\kappa_{n,0} d)|^2} \\
&\times \left\{ \frac{\Im[\kappa_{n,0} a I_1(\kappa_{n,0}^* a) I_2(\kappa_{n,0} a) - \kappa_{n,0} d I_1(\kappa_{n,0}^* d) I_2(\kappa_{n,0} d)]}{\Im[\kappa_{n,0}^2]} \right. \\
&+ 2\Re\left[\frac{I_0(\kappa_{n,0} a)}{K_0(\kappa_{n,0} a)} \left(- \frac{a(\kappa_{n,0}^* I_2(\kappa_{n,0}^* a) K_1(\kappa_{n,0} a) + \kappa_{n,0} I_1(\kappa_{n,0}^* a) K_2(\kappa_{n,0} a))}{(\kappa_{n,0}^2 - \kappa_{n,0}^{*2})} \right.\right. \\
&\left.\left. + \frac{d(\kappa_{n,0}^* I_2(\kappa_{n,0}^* d) K_1(\kappa_{n,0} d) + \kappa_{n,0} I_1(\kappa_{n,0}^* d) K_2(\kappa_{n,0} d))}{(\kappa_{n,0}^2 - \kappa_{n,0}^{*2})} \right) \right] \\
&\left. + \frac{|I_0(\kappa_{n,0} a)|^2 \Im[\kappa_{n,0}^*(a K_0(\kappa_{n,0}^* a) K_1(\kappa_{n,0} a) - d K_0(\kappa_{n,0}^* d) K_1(\kappa_{n,0} d))]}{|K_0(\kappa_{n,0} a)|^2 \Im[\kappa_{n,0}^2]} \right\} \Bigg\}, \qquad \text{(A.68)}
\end{aligned}
$$

and $j_{0,n}$ is the nth zero of the Bessel function $J_0(z)$.

In the above derivation, we use the following formulae [29]:

$$
\begin{aligned}
\frac{\partial \rho \tilde{H}_\theta}{\partial \rho} &= - \frac{j_{0,n} \rho J_0(\Lambda_{\mathrm{TM}} \rho)}{j\sqrt{\pi} a^2 J_1(j_{0,n})} + \frac{j_{0,n} \rho J_0(\Lambda_{\mathrm{TM}} \rho)}{j\sqrt{\pi} a^2 J_1(j_{0,n})} \Theta(\rho - d) \\
&\quad - \frac{j_{0,n} J_1(\Lambda_{\mathrm{TM}} d) \rho [I_0(\kappa_{n,0} \rho) - \frac{I_0(\kappa_{n,0} a)}{K_0(\kappa_{n,0} a)} K_0(\kappa_{n,0} \rho)]}{j\sqrt{\pi} a^2 J_1(j_{0,n}) [I_1(\kappa_{n,0} d) + \frac{I_0(\kappa_{n,0} a)}{K_0(\kappa_{n,0} a)} K_1(\kappa_{n,0} d)]} \Theta(\rho - d), \qquad \text{(A.69)} \\
\frac{1}{\epsilon^*(\rho, \theta)} \frac{1}{\rho} \frac{\partial \rho \tilde{H}_\theta^*}{\partial \rho} &= \left(\frac{1}{\epsilon_0} - \frac{1}{\epsilon_0} \Theta(\rho - d) + \frac{1}{(\epsilon_0 - \frac{\sigma_c^*}{j\omega})} \Theta(\rho - d) \right) \\
&\quad \times \left(\frac{j_{0,n} J_0(\Lambda_{\mathrm{TM}}^* \rho)}{j\sqrt{\pi} a^2 J_1(j_{0,n})} - \frac{j_{0,n} J_0(\Lambda_{\mathrm{TM}}^* \rho)}{j\sqrt{\pi} a^2 J_1(j_{0,n})} \Theta(\rho - d) \right. \\
&\quad \left. + \frac{j_{0,n} J_1(\Lambda_{\mathrm{TM}}^* d) [I_0(\kappa_{n,0}^* \rho) - \frac{I_0(\kappa_{n,0}^* a)}{K_0(\kappa_{n,0}^* a)} K_0(\kappa_{n,0}^* \rho)]}{j\sqrt{\pi} a^2 J_1(j_{0,n}) [I_1(\kappa_{n,0}^* d) + \frac{I_0(\kappa_{n,0}^* a)}{K_0(\kappa_{n,0}^* a)} K_1(\kappa_{n,0}^* d)]} \Theta(\rho - d) \right), \qquad \text{(A.70)}
\end{aligned}
$$

$$\frac{1}{\epsilon(\rho,\theta)} = \frac{1}{\epsilon_0} - \frac{1}{\epsilon_0}\Theta(\rho-d) + \frac{1}{(\epsilon_0+\frac{\sigma_c}{j\omega})}\Theta(\rho-d), \tag{A.71}$$

$$\int_0^d dzzJ_1(\Lambda_{\rm TM}z)J_1(\Lambda^*_{\rm TM}z) = \frac{\Im[\Lambda^*_{\rm TM}dJ_0(\Lambda^*_{\rm TM}d)J_1(\Lambda_{\rm TM}d)]}{\Im[\Lambda^2_{\rm TM}]}, \tag{A.72}$$

$$\int_d^a dzzI_1(\kappa_{n,0}z)I_1(\kappa^*_{n,0}z) = \frac{\Im[\kappa_{n,0}aI_1(\kappa^*_{n,0}a)I_2(\kappa_{n,0}a) - \kappa_{n,0}dI_1(\kappa^*_{n,0}d)I_2(\kappa_{n,0}d)]}{\Im[\kappa^2_{n,0}]}, \tag{A.73}$$

$$\begin{aligned}\int_d^a dzzI_1(\kappa_{n,0}z)K_1(\kappa^*_{n,0}z) = &\frac{a(\kappa_{n,0}I_2(\kappa_{n,0}a)K_1(\kappa^*_{n,0}a) + \kappa^*_{n,0}I_1(\kappa_{n,0}a)K_2(\kappa^*_{n,0}a))}{(\kappa^2_{n,0}-\kappa^{*2}_{n,0})}\\ &- \frac{d(\kappa_{n,0}I_2(\kappa_{n,0}d)K_1(\kappa^*_{n,0}d) + \kappa^*_{n,0}I_1(\kappa_{n,0}d)K_2(\kappa^*_{n,0}d))}{(\kappa^2_{n,0}-\kappa^{*2}_{n,0})},\end{aligned} \tag{A.74}$$

$$\begin{aligned}\int_d^a dzzI_1(\kappa^*_{n,0}z)K_1(\kappa_{n,0}z) = &-\frac{a(\kappa^*_{n,0}I_2(\kappa^*_{n,0}a)K_1(\kappa_{n,0}a) + \kappa_{n,0}I_1(\kappa^*_{n,0}a)K_2(\kappa_{n,0}a))}{(\kappa^2_{n,0}-\kappa^{*2}_{n,0})}\\ &+ \frac{d(\kappa^*_{n,0}I_2(\kappa^*_{n,0}d)K_1(\kappa_{n,0}d) + \kappa_{n,0}I_1(\kappa^*_{n,0}d)K_2(\kappa_{n,0}d))}{(\kappa^2_{n,0}-\kappa^{*2}_{n,0})},\end{aligned} \tag{A.75}$$

$$\int_d^a dzzK_1(\kappa_{n,0}z)K_1(\kappa^*_{n,0}z) = \frac{\Im[\kappa^*_{n,0}(aK_0(\kappa^*_{n,0}a)K_1(\kappa_{n,0}a) - dK_0(\kappa^*_{n,0}d)K_1(\kappa_{n,0}d)])}{\Im[\kappa^2_{n,0}]}, \tag{A.76}$$

$$\int_0^d dzzJ_0(\Lambda_{\rm TM}z)J_0(\Lambda^*_{\rm TM}z) = \frac{\Im[\Lambda_{\rm TM}dJ_0(\Lambda^*_{\rm TM}d)J_1(\Lambda_{\rm TM}d)]}{\Im[\Lambda^2_{\rm TM}]}, \tag{A.77}$$

$$\int_d^a d\rho\rho I_0(\kappa_{n,0}\rho)I_0(\kappa^*_{n,0}\rho) = \frac{\Im[\kappa_{n,0}aI_0(\kappa^*_{n,0}a)I_1(\kappa_{n,0}a)]}{\Im[\kappa^2_{n,0}]} - \frac{\Im[\kappa_{n,0}dI_0(\kappa^*_{n,0}d)I_1(\kappa_{n,0}d)]}{\Im[\kappa^2_{n,0}]}, \tag{A.78}$$

$$\begin{aligned}\int_d^a d\rho\rho I_0(\kappa_{n,0}\rho)K_0(\kappa^*_{n,0}\rho) = &\frac{a(\kappa_{n,0}I_1(\kappa_{n,0}a)K_0(\kappa^*_{n,0}a) + \kappa^*_{n,0}I_0(\kappa_{n,0}a)K_1(\kappa^*_{n,0}a))}{(\kappa^2_{n,0}-\kappa^{*2}_{n,0})}\\ &- \frac{d(\kappa_{n,0}I_1(\kappa_{n,0}d)K_0(\kappa^*_{n,0}d) + \kappa^*_{n,0}I_0(\kappa_{n,0}d)K_1(\kappa^*_{n,0}d))}{(\kappa^2_{n,0}-\kappa^{*2}_{n,0})},\end{aligned} \tag{A.79}$$

$$\begin{aligned}\int_d^a d\rho\rho K_0(\kappa_{n,0}\rho)I_0(\kappa^*_{n,0}\rho) = &-\frac{a(\kappa^*_{n,0}I_1(\kappa^*_{n,0}a)K_0(\kappa_{n,0}a) + \kappa_{n,0}I_0(\kappa^*_{n,0}a)K_1(\kappa_{n,0}a))}{(\kappa^2_{n,0}-\kappa^{*2}_{n,0})}\\ &+ \frac{d(\kappa^*_{n,0}I_1(\kappa^*_{n,0}d)K_0(\kappa_{n,0}d) + \kappa_{n,0}I_0(\kappa^*_{n,0}d)K_1(\kappa_{n,0}d))}{(\kappa^2_{n,0}-\kappa^{*2}_{n,0})},\end{aligned} \tag{A.80}$$

$$\int_d^a d\rho\rho K_0(\kappa_{n,0}\rho)K_0(\kappa^*_{n,0}\rho) = -\frac{\Im[\kappa_{n,0}aK_0(\kappa^*_{n,0}a)K_1(\kappa_{n,0}a)]}{\Im[\kappa^2_{n,0}]} + \frac{\Im[\kappa_{n,0}dK_0(\kappa^*_{n,0}d)K_1(\kappa_{n,0}d)]}{\Im[\kappa^2_{n,0}]}, \tag{A.81}$$

$$J_\nu(z^*) = J^*_\nu(z), \tag{A.82}$$

$$I_\nu(z^*) = I^*_\nu(z), \tag{A.83}$$

and

$$K_\nu(z^*) = K^*_\nu(z). \tag{A.84}$$

Finally, we obtain the scattering matrix for the TM_{0n} mode by using the waveguide method as

$$S_{11} = S_{22} = \frac{\left(\frac{1}{Z_{50}^2} - \frac{C_I^2}{C_V^2}\right)}{\frac{1}{Z_{50}^2} + \frac{C_I^2}{C_V^2} + \frac{2C_I}{C_V Z_{50} j \tan \Gamma_{n,0}^{\mathrm{TM}} g}}, \tag{A.85}$$

and

$$S_{21} = S_{12} = \frac{\frac{2C_I}{C_V Z_{50} j \sin \Gamma_{n,0}^{\mathrm{TM}} g}}{\frac{1}{Z_{50}^2} + \frac{C_I^2}{C_V^2} + \frac{2C_I}{C_V Z_{50} j \tan \Gamma_{n,0}^{\mathrm{TM}} g}}, \tag{A.86}$$

where we assume that the resistive waveguide with longitudinal length g is sandwiched between cables with the characteristic impedance Z_{50}. Equations.(A.85) and (A.86) are equivalent to Eqs. (9) and (10) in the text.

Appendix B. Derivation of formulae for the transmission coefficient S_{21}^w using the wire method

In this appendix, we derive the formulae for the transmission coefficient S_{21}^w by using the wire method. A perfectly conductive single wire with radius ρ_w is stretched out at the center of the chamber with inner radius d, and the current I_0 is driven through the wire. The device under test (resistive chamber) with the length $2w(= g)$ is sandwiched between perfectively conductive chambers [11,33]. The thickness of the chambers is $a - d$. We assume that the perfectly conductive wall covers the outer surface ($\rho = a$) of the chambers.

Because the longitudinal electric field E_z should be zero on the surface of the wire, the solutions in vacuum are described by the Neumann function $Y_n(x)$ in combination with the Bessel function $J_n(x)$. They are expressed as [47]

$$E_z(\rho, z) = \int_{-\infty}^{\infty} dq e^{-jqz} A(q) \frac{Y_0\left(\sqrt{k^2-q^2}\rho\right) - \frac{Y_0\left(\sqrt{k^2-q^2}\rho_w\right)}{J_0\left(\sqrt{k^2-q^2}\rho_w\right)} J_0\left(\sqrt{k^2-q^2}\rho\right)}{Y_0\left(\sqrt{k^2-q^2}d\right) - \frac{Y_0\left(\sqrt{k^2-q^2}\rho_w\right)}{J_0\left(\sqrt{k^2-q^2}\rho_w\right)} J_0\left(\sqrt{k^2-q^2}d\right)}, \tag{B.1}$$

$$H_\theta(\rho, z) = j\frac{k}{Z_0} \int_{-\infty}^{\infty} dq e^{-jqz} \frac{A(q)\left[Y_1\left(\sqrt{k^2-q^2}\rho\right) - \frac{Y_0\left(\sqrt{k^2-q^2}\rho_w\right)}{J_0\left(\sqrt{k^2-q^2}\rho_w\right)} J_1\left(\sqrt{k^2-q^2}\rho\right)\right]}{\sqrt{k^2-q^2}\left(Y_0\left(\sqrt{k^2-q^2}d\right) - \frac{Y_0\left(\sqrt{k^2-q^2}\rho_w\right)}{J_0\left(\sqrt{k^2-q^2}\rho_w\right)} J_0\left(\sqrt{k^2-q^2}d\right)\right)} + \frac{I_0}{2\pi\rho} e^{-jkz}, \tag{B.2}$$

$$E_\rho(\rho, z) = -\frac{Z_0}{jk}\frac{\partial H_\theta}{\partial z}, \tag{B.3}$$

where the factor $e^{j\omega t}$ is omitted, $k = \omega/c$, $Z_0 = 120\pi\ \Omega$, and $A(q)$ is the expansion coefficient. Here, the poles are above the real axis for $q < 0$ and below the real axis for $q > 0$.

Because E_z on the inner surface of the two perfectly conductive chambers sandwiching the resistive chamber should be zero, the expansion coefficient $A(q)$ should satisfy the following relation [11,33]:

$$\int_{-\infty}^{\infty} dq\, A(q) e^{-jqz} = \begin{cases} \frac{V_1}{2w} + \frac{\sum_{m=1}^{\infty} V_1^{(m)} \cos\frac{m\pi(z+w)}{2w}}{w}, & \text{for } -w < z < w, \\ 0, & \text{otherwise,} \end{cases} \tag{B.4}$$

where V_1 is the voltage on the inner surface of the resistive chamber at $\rho = d$, and $V_1^{(m)}$ are the higher-order expansion coefficients. Consequently, the original expansion coefficient $A(q)$ is rewritten by using the new expansion coefficients V_1 and $V_1^{(m)}$ as

$$A(q) = \frac{V_1}{2\pi}\frac{\sin qw}{qw} + \sum_{m=1}^{\infty} \frac{V_1^{(m)}((-1)^m e^{jqw} - e^{-jqw})q}{j2\pi w(q^2 - \frac{m^2\pi^2}{4w^2})}. \tag{B.5}$$

Substituting Eq. (B.5) into Eqs. (B.1)–(B.2), we obtain

$$E_z(\rho,z) = \int_{-\infty}^{\infty} dq e^{-jqz} \times \frac{\left[\frac{V_1}{2\pi}\frac{\sin qw}{qw} + \sum_{m=1}^{\infty} \frac{V_1^{(m)}((-1)^m e^{jqw} - e^{-jqw})q}{j2\pi w(q^2 - \frac{m^2\pi^2}{4w^2})}\right]\left[Y_0\left(\sqrt{k^2-q^2}\rho\right) - \frac{Y_0\left(\sqrt{k^2-q^2}\rho_w\right)}{J_0\left(\sqrt{k^2-q^2}\rho_w\right)} J_0\left(\sqrt{k^2-q^2}\rho\right)\right]}{\left[Y_0\left(\sqrt{k^2-q^2}d\right) - \frac{Y_0\left(\sqrt{k^2-q^2}\rho_w\right)}{J_0\left(\sqrt{k^2-q^2}\rho_w\right)} J_0\left(\sqrt{k^2-q^2}d\right)\right]}, \tag{B.6}$$

$$H_\theta(\rho,z) = j\frac{k}{Z_0}\int_{-\infty}^{\infty} dq e^{-jqz} \frac{\frac{V_1}{2\pi}\frac{\sin qw}{qw}\left[Y_1\left(\sqrt{k^2-q^2}\rho\right) - \frac{Y_0\left(\sqrt{k^2-q^2}\rho_w\right)}{J_0\left(\sqrt{k^2-q^2}\rho_w\right)} J_1\left(\sqrt{k^2-q^2}\rho\right)\right]}{\sqrt{k^2-q^2}\left[Y_0\left(\sqrt{k^2-q^2}d\right) - \frac{Y_0\left(\sqrt{k^2-q^2}\rho_w\right)}{J_0\left(\sqrt{k^2-q^2}\rho_w\right)} J_0\left(\sqrt{k^2-q^2}d\right)\right]}$$
$$+ j\frac{k}{Z_0}\sum_{m=1}^{\infty}\int_{-\infty}^{\infty} dq e^{-jqz} \frac{\frac{V_1^{(m)}((-1)^m e^{jqw} - e^{-jqw})q}{j2\pi w(q^2 - \frac{m^2\pi^2}{4w^2})}\left[Y_1\left(\sqrt{k^2-q^2}\rho\right) - \frac{Y_0\left(\sqrt{k^2-q^2}\rho_w\right)}{J_0\left(\sqrt{k^2-q^2}\rho_w\right)} J_1\left(\sqrt{k^2-q^2}\rho\right)\right]}{\sqrt{k^2-q^2}\left[Y_0\left(\sqrt{k^2-q^2}d\right) - \frac{Y_0\left(\sqrt{k^2-q^2}\rho_w\right)}{J_0\left(\sqrt{k^2-q^2}\rho_w\right)} J_0\left(\sqrt{k^2-q^2}d\right)\right]}$$
$$+ \frac{I_0}{2\pi\rho}e^{-jkz}, \tag{B.7}$$

$$E_\rho(\rho,z) = j\int_{-\infty}^{\infty} dq e^{-jqz} \frac{q\frac{V_1}{2\pi}\frac{\sin qw}{qw}\left[Y_1\left(\sqrt{k^2-q^2}\rho\right) - \frac{Y_0\left(\sqrt{k^2-q^2}\rho_w\right)}{J_0\left(\sqrt{k^2-q^2}\rho_w\right)} J_1\left(\sqrt{k^2-q^2}\rho\right)\right]}{\sqrt{k^2-q^2}\left[Y_0\left(\sqrt{k^2-q^2}d\right) - \frac{Y_0\left(\sqrt{k^2-q^2}\rho_w\right)}{J_0\left(\sqrt{k^2-q^2}\rho_w\right)} J_0\left(\sqrt{k^2-q^2}d\right)\right]}$$
$$+ \sum_{m=1}^{\infty}\int_{-\infty}^{\infty} dq e^{-jqz} \frac{\frac{V_1^{(m)}((-1)^m e^{jqw} - e^{-jqw})q^2}{2\pi w(q^2 - \frac{m^2\pi^2}{4w^2})}\left[Y_1\left(\sqrt{k^2-q^2}\rho\right) - \frac{Y_0\left(\sqrt{k^2-q^2}\rho_w\right)}{J_0\left(\sqrt{k^2-q^2}\rho_w\right)} J_1\left(\sqrt{k^2-q^2}\rho\right)\right]}{\sqrt{k^2-q^2}\left[Y_0\left(\sqrt{k^2-q^2}d\right) - \frac{Y_0\left(\sqrt{k^2-q^2}\rho_w\right)}{J_0\left(\sqrt{k^2-q^2}\rho_w\right)} J_0\left(\sqrt{k^2-q^2}d\right)\right]}$$
$$+ \frac{I_0 Z_0}{2\pi\rho}e^{-jkz}. \tag{B.8}$$

The voltage $V(z)$ at z between the wire and the outer chamber is calculated as

$$V(z) = -j\int_{-\infty}^{\infty} dq e^{-jqz}\frac{q\frac{V_1}{2\pi}\frac{\sin qw}{qw}}{(k^2-q^2)} - \sum_{m=1}^{\infty}\int_{-\infty}^{\infty} dq e^{-jqz}\frac{V_1^{(m)}((-1)^m e^{jqw}-e^{-jqw})q^2}{2\pi w(q^2-\frac{m^2\pi^2}{4w^2})(k^2-q^2)} + \frac{I_0 Z_0}{2\pi}e^{-jkz}\log[\frac{d}{\rho_w}], \tag{B.9}$$

while the current $I_z(z)$ at z on the wire is calculated as

$$\begin{aligned} I_z(z) = {} & \frac{kV_1}{2wZ_0\log[\frac{d}{\rho_w}]}\int_{-\infty}^{\infty} dq\frac{e^{-jqz}(e^{jqw}-e^{-jqw})}{q(q^2-k^2)} \\ & - \frac{kV_1}{wZ_0}\int_{-\infty}^{\infty} dq\frac{e^{-jqz}(e^{jqw}-e^{-jqw})}{q}\sum_{l=1}^{\infty}\frac{J_0(i_l)J_0(i_l\frac{\rho_w}{d})}{(q^2-k^2+\frac{i_l^2}{d^2})(J_0^2(i_l)-J_0^2(i_l\frac{\rho_w}{d}))} \\ & + \frac{k}{wZ_0\log[\frac{d}{\rho_w}]}\sum_{m=1}^{\infty}\int_{-\infty}^{\infty} dq e^{-jqz}\frac{V_1^{(m)}((-1)^m e^{jqw}-e^{-jqw})q}{(q^2-\frac{m^2\pi^2}{4w^2})(q^2-k^2)} \\ & - \frac{2k}{wZ_0}\sum_{m=1}^{\infty}\int_{-\infty}^{\infty} dq e^{-jqz}\frac{V_1^{(m)}((-1)^m e^{jqw}-e^{-jqw})q}{(q^2-\frac{m^2\pi^2}{4w^2})}\sum_{l=1}^{\infty}\frac{J_0(i_l)J_0(i_l\frac{\rho_w}{d})}{(q^2-k^2+\frac{i_l^2}{d^2})(J_0^2(i_l)-J_0^2(i_l\frac{\rho_w}{d}))} \\ & + I_0 e^{-jkz}, \end{aligned} \tag{B.10}$$

by using the formulae (see Appendix C)

$$J_0(z)Y_1(z) - J_1(z)Y_0(z) = -\frac{2}{\pi z}, \tag{B.11}$$

$$\begin{aligned} \frac{1}{J_0(z\frac{\rho_w}{d})(Y_0(z)-\frac{Y_0(z\frac{\rho_w}{d})}{J_0(z\frac{\rho_w}{d})}J_0(z))} = {} & \frac{\pi}{2\log[\frac{d}{\rho_w}]} - \sum_{l=1}^{\infty}\frac{\pi J_0(i_l)J_0(i_l\frac{\rho_w}{d})}{(J_0^2(i_l)-J_0^2(i_l\frac{\rho_w}{d}))} \\ & + \sum_{l=1}^{\infty}\frac{i_l^2\pi J_0(i_l)J_0(i_l\frac{\rho_w}{d})}{(-z^2+i_l^2)(J_0^2(i_l)-J_0^2(i_l\frac{\rho_w}{d}))}, \end{aligned} \tag{B.12}$$

where i_l is the zero of the function $Y_0(x) - Y_0(x\rho_w/d)/J_0(x\rho_w/d)J_0(x)$.

As a regularization parameter, we introduce the total length of the three chambers together as L, where we assume $L/2 \gg w$. By using Eqs. (B.9) and (B.10), $V(\mp L/2)$ and $I_z(\mp L/2)$ are simplified as

$$\begin{aligned} V(\mp\frac{L}{2}) = {} & \mp e^{-jk\frac{L}{2}}\frac{V_1\sin kw}{2kw} - j\sum_{m=1,m\neq\tilde{n}}^{\infty}\frac{V_1^{(m)}((-1)^m e^{-jk(\frac{L}{2}\pm w)} - e^{-jk(\frac{L}{2}\mp w)})k}{2w(\frac{\tilde{n}^2\pi^2}{4w^2}-\frac{m^2\pi^2}{4w^2})} \\ & \mp \frac{e^{-jk\frac{L}{2}}V_1^{(\tilde{n})}[(-1)^{\tilde{n}}e^{\mp j\frac{\tilde{n}\pi}{2}} + e^{\pm j\frac{\tilde{n}\pi}{2}}]}{4} + \frac{I_0 Z_0}{2\pi}e^{\pm jk\frac{L}{2}}\log[\frac{d}{\rho_w}], \end{aligned} \tag{B.13}$$

for $k = \tilde{n}\pi/2w$,

$$V(\mp\frac{L}{2}) = \mp e^{-jk\frac{L}{2}}\frac{V_1\sin kw}{2kw} - j\sum_{m=1}^{\infty}\frac{V_1^{(m)}((-1)^m e^{-jk(\frac{L}{2}\pm w)} - e^{-jk(\frac{L}{2}\mp w)})k}{2w(k^2-\frac{m^2\pi^2}{4w^2})} + \frac{I_0 Z_0}{2\pi}e^{\pm jk\frac{L}{2}}\log[\frac{d}{\rho_w}], \tag{B.14}$$

for $k \neq \tilde{n}\pi/2w$, and

$$I_z(\mp\frac{L}{2}) = \frac{\pi V_1 \sin kw}{kwZ_0 \log[\frac{d}{\rho_w}]} e^{-jk\frac{L}{2}} \pm j\frac{\pi k}{wZ_0 \log[\frac{d}{\rho_w}]} \sum_{m=1,m\neq\tilde{n}}^{\infty} V_1^{(m)} \frac{e^{-jk\frac{L}{2}}((-1)^m e^{\mp jkw} - e^{\pm jkw})}{(k^2 - \frac{m^2\pi^2}{4w^2})} + \frac{\pi V_1^{(\tilde{n})} e^{-jk\frac{L}{2}}[(-1)^{\tilde{n}} e^{\mp jkw} + e^{\pm jkw}]}{2Z_0 \log[\frac{d}{\rho_w}]} + I_0 e^{\pm jk\frac{L}{2}}, \tag{B.15}$$

for $(k = \tilde{n}\pi/2w) \cap (k < i_1/d)$ and the large-L limit,

$$I_z(\mp\frac{L}{2}) = \frac{\pi V_1 \sin kw}{kwZ_0 \log[\frac{d}{\rho_w}]} e^{-jk\frac{L}{2}} \pm j\frac{\pi k e^{-jk\frac{L}{2}}}{wZ_0 \log[\frac{d}{\rho_w}]} \sum_{m=1}^{\infty} V_1^{(m)} \frac{((-1)^m e^{\mp jkw} - e^{\pm jkw})}{(k^2 - \frac{m^2\pi^2}{4w^2})} + I_0 e^{\pm jk\frac{L}{2}}, \tag{B.16}$$

for $(k \neq \tilde{n}\pi/2w) \cap (k < i_1/d)$ and the large-L limit, where $\tilde{n}$ is an arbitrary positive integer.

Now the transmission coefficient S_{21}^w is calculated as

$$S_{21}^w = \lim_{L\to\infty} \frac{2V(L/2)}{V(-L/2) + I_z(-L/2)Z_c}, \tag{B.17}$$

where the characteristic impedance Z_c is given by

$$Z_c = \frac{Z_0}{2\pi} \log \frac{d}{\rho_w}. \tag{B.18}$$

Especially when the resistive chamber (the device under test) is replaced by the perfectly conductive chamber, the transmission coefficient is calculated as

$$S_{21}^{w(\mathrm{ref})} = e^{-jkL}. \tag{B.19}$$

Concretely, we obtain the formulae for the ratio of the transmission coefficients $S_{21}^w/S_{21}^{w(\mathrm{ref})}$ as

$$\frac{S_{21}^w}{S_{21}^{w(\mathrm{ref})}} = \frac{\frac{V_1 \sin kw}{2kw} - j\sum_{m=1}^{\infty} \frac{V_1^{(m)}((-1)^m e^{jkw} - e^{-jkw})k}{2w(k^2 - \frac{m^2\pi^2}{4w^2})} + I_0 Z_c}{Z_c I_0}, \tag{B.20}$$

for $(k \neq \tilde{n}\pi/2w) \cap (k < i_1/d)$, and

$$\frac{S_{21}^w}{S_{21}^{w(\mathrm{ref})}} = \frac{\frac{V_1 \sin kw}{2kw} - j\sum_{m=1,m\neq\tilde{n}}^{\infty} \frac{V_1^{(m)}((-1)^m e^{jkw} - e^{-jkw})k}{2w(\frac{\tilde{n}^2\pi^2}{4w^2} - \frac{m^2\pi^2}{4w^2})} + \frac{V_1^{(\tilde{n})}[(-1)^{\tilde{n}} e^{j\frac{\tilde{n}\pi}{2}} + e^{-j\frac{\tilde{n}\pi}{2}}]}{4} + I_0 Z_c}{Z_c I_0}, \tag{B.21}$$

for $(k = \tilde{n}\pi/2w) \cap (k < i_1/d)$, which is equivalent to formulae (24) and (25) in the text.

The expansion coefficients V_1 and $V_1^{(m)}$ in the formulae are determined using the boundary condition of E_z on $\rho = a$, which is expressed as

$$\left[\frac{A_0^{(0)}}{2w} + \frac{jkC_0^{(0)}\langle J(z)\rangle}{2\pi Z_0}\right] V_1 + \sum_{n=1}^{\infty} \frac{kC_0^{(0)}\langle J^{(n)}(z)\rangle}{2\pi wZ_0} V_1^{(n)} = -C_0^{(0)}\langle \alpha(z)\rangle, \tag{B.22}$$

$$\frac{jkC_0^{(m)}\langle\langle J(z)\rangle\rangle_m}{2\pi Z_0} V_1 + \sum_{n=1}^{\infty} \left[\delta_{n,m}A_0^{(n)} + \frac{kC_0^{(m)}\langle\langle J^{(n)}(z)\rangle\rangle_m}{2\pi wZ_0}\right] V_1^{(n)} = -C_0^{(m)}\langle\langle \alpha(z)\rangle\rangle_m, \tag{B.23}$$

where

$$\langle \alpha \rangle = \frac{I_0}{2\pi d} \frac{\sin kw}{kw}, \tag{B.24}$$

$$\langle \langle \alpha \rangle \rangle_m = -\frac{I_0}{2\pi d} \frac{k((-1)^m e^{-jkw} - e^{jkw})}{j(k^2 - \frac{m^2\pi^2}{4w^2})}, \tag{B.25}$$

$$\langle J(z) \rangle = -\frac{2\pi}{wd} \sum_{s=0}^{\infty} \frac{\alpha_s}{(k^2 - \frac{i_s^2}{d^2})} - \frac{\pi}{w^2 d} \sum_{s=0}^{\infty} \frac{\alpha_s (e^{-j\sqrt{k^2 - \frac{i_s^2}{d^2}}(2w)} - 1)}{j(k^2 - \frac{i_s^2}{d^2})^{\frac{3}{2}}}, \tag{B.26}$$

$$\left\langle J^{(m)}(z) \right\rangle = \sum_{s=0}^{\infty} \frac{\pi \alpha_s (1 + (-1)^m)(1 - e^{-j\sqrt{k^2 - \frac{i_s^2}{d^2}} 2w})}{wd\sqrt{k^2 - \frac{i_s^2}{d^2}}(k^2 - \frac{i_s^2}{d^2} - \frac{m^2\pi^2}{4w^2})}, \tag{B.27}$$

$$\langle \langle J(z) \rangle \rangle_m = \sum_{s=0}^{\infty} \frac{\alpha_s \pi j (1 + (-1)^m)(e^{-j2\sqrt{k^2 - \frac{i_s^2}{d^2}} w} - 1)}{wd(k^2 - \frac{i_s^2}{d^2} - \frac{m^2\pi^2}{4w^2})\sqrt{k^2 - \frac{i_s^2}{d^2}}}, \tag{B.28}$$

$$\left\langle \left\langle J^{(n)}(z) \right\rangle \right\rangle_m = \begin{cases} \sum_{s=0}^{\infty} \frac{2\pi\alpha_s (1 + (-1)^{n+m}) \sqrt{k^2 - \frac{i_s^2}{d^2}} (1 - (-1)^n e^{-j2\sqrt{k^2 - \frac{i_s^2}{d^2}} w})}{d(k^2 - \frac{i_s^2}{d^2} - \frac{m^2\pi^2}{4w^2})(k^2 - \frac{i_s^2}{d^2} - \frac{n^2\pi^2}{4w^2})}, \text{for } n \neq m, \\ \sum_{s=0}^{\infty} \frac{4\pi\alpha_s \sqrt{k^2 - \frac{i_s^2}{d^2}} (1 - (-1)^m e^{-j2\sqrt{k^2 - \frac{i_s^2}{d^2}} w})}{d(k^2 - \frac{i_s^2}{d^2} - \frac{m^2\pi^2}{4w^2})^2} \\ + \sum_{s=0}^{\infty} \frac{j4\pi w \alpha_s}{d(\frac{m^2\pi^2}{4w^2} - k^2 + \frac{i_s^2}{d^2})}, \text{for } n = m, \end{cases} \tag{B.29}$$

$$\alpha_s = \frac{J_0^2[\frac{\rho_w i_s}{d}]}{J_0^2[\frac{\rho_w i_s}{d}] - J_0^2[i_s]}, \text{for } s \geq 1, \tag{B.30}$$

$$\alpha_0 = \frac{1}{2\log[\frac{d}{\rho_w}]}, \tag{B.31}$$

and

$$i_0 \equiv 0. \tag{B.32}$$

Here,

$$\alpha(z) = \frac{I_0}{2\pi d} e^{-jkz}, \tag{B.33}$$

$$J(z) = \int_{-\infty}^{\infty} e^{-jqz} \frac{\left[Y_1\left(\sqrt{k^2 - q^2} d\right) - \frac{Y_0\left(\sqrt{k^2 - q^2}\rho_w\right)}{J_0\left(\sqrt{k^2 - q^2}\rho_w\right)} J_1\left(\sqrt{k^2 - q^2} d\right) \right]}{\sqrt{k^2 - q^2} \left[Y_0\left(\sqrt{k^2 - q^2} d\right) - \frac{Y_0\left(\sqrt{k^2 - q^2}\rho_w\right)}{J_0\left(\sqrt{k^2 - q^2}\rho_w\right)} J_0\left(\sqrt{k^2 - q^2} d\right) \right]} \frac{\sin qw}{qw} dq, \tag{B.34}$$

$$J^{(m)}(z) = \int_{-\infty}^{\infty} dq e^{-jqz} \times \frac{((-1)^m e^{jqw} - e^{-jqw})q \left[Y_1\left(\sqrt{k^2-q^2}d\right) - \frac{Y_0\left(\sqrt{k^2-q^2}\rho_w\right)}{J_0\left(\sqrt{k^2-q^2}\rho_w\right)} J_1\left(\sqrt{k^2-q^2}d\right) \right]}{(q^2 - \frac{m^2\pi^2}{4w^2})\sqrt{k^2-q^2} \left[Y_0\left(\sqrt{k^2-q^2}d\right) - \frac{Y_0\left(\sqrt{k^2-q^2}\rho_w\right)}{J_0\left(\sqrt{k^2-q^2}\rho_w\right)} J_0\left(\sqrt{k^2-q^2}d\right) \right]}, \quad \text{(B.35)}$$

and the brackets in Eqs. (B.24)–(B.29) are defined as

$$\langle \cdots \rangle \equiv \frac{1}{2w} \int_{-w}^{w} dz \cdots, \quad \text{(B.36)}$$

$$\langle\langle \cdots \rangle\rangle_m \equiv \int_{-w}^{w} dz \cos\frac{m\pi(z+w)}{2w} \cdots. \quad \text{(B.37)}$$

Here, $A_0^{(0)}, C_0^{(0)}, A_0^{(m)}$, and $C_0^{(m)}$ with positive integer m, which are determined using the solutions of the Maxwell equations in the case of a resistive material with conductivity σ_c, are the transfer coefficients that transfer the fields on the inner surface ($\rho = d$) to the outer surface ($\rho = a$) of the resistive material (device under test). All expansion coefficients V_1 and $V_1^{(m)}$ are obtained by solving Eqs. (B.22)–(B.23) for any m.

Before concluding this appendix, let us derive concrete forms of the transfer coefficients [11]. Because the resistive material is sandwiched between perfectly conductive chambers, the monopole mode fields in the material expand according to sinusoidal functions as

$$E_z = \frac{1}{2w}\tilde{\tilde{E}}_z^{(0)} + \frac{1}{w}\sum_{m=1}^{\infty} \cos\frac{m\pi(z+w)}{2w}\tilde{\tilde{E}}_z^{(m)}, \quad \text{(B.38)}$$

and

$$H_\theta = \frac{1}{2w}\tilde{\tilde{H}}_\theta^{(0)} + \frac{1}{w}\sum_{m=1}^{\infty} \cos\frac{m\pi(z+w)}{2w}\tilde{\tilde{H}}_\theta^{(m)}. \quad \text{(B.39)}$$

Substituting them into the Maxwell equations

$$\mathrm{rot}\vec{E} = -\frac{\partial \vec{B}}{\partial t} = -\mu_0\frac{\partial \vec{H}}{\partial t} = -jkZ_0\vec{H}, \quad \text{(B.40)}$$

$$\mathrm{rot}\vec{H} = \sigma_c\vec{E} + \frac{\partial \vec{D}}{\partial t} = (\frac{\sigma_c Z_0}{jk} + 1)\frac{jk}{Z_0}\vec{E} \equiv \tilde{\epsilon} j\omega\epsilon_0\vec{E}, \quad \text{(B.41)}$$

the solutions of Eqs. (B.38) and (B.39) are given as

$$\tilde{\tilde{E}}_z^{(m)} = \tilde{\Gamma}_0 I_0(\mu_m\rho) + \Gamma_0 K_0(\mu_m\rho), \quad \text{(B.42)}$$

$$\tilde{\tilde{H}}_\theta^{(m)} = \frac{jk\tilde{\epsilon}}{Z_0\mu_m}[\tilde{\Gamma}_0 I_0'(\mu_m\rho) + \Gamma_0 K_0'(\mu_m\rho)], \quad \text{(B.43)}$$

where $\tilde{\Gamma}_0$ and Γ_0 are arbitrary coefficients and

$$\mu_m = \sqrt{\frac{m^2\pi^2}{4w^2} - k^2\tilde{\epsilon}}. \quad \text{(B.44)}$$

Using these solutions, the fields on $\rho = d$ are transferred to those on $\rho = a$ as

$$\begin{pmatrix} \tilde{\tilde{E}}_z^{(m)}(a) \\ \tilde{\tilde{H}}_\theta^{(m)}(a) \end{pmatrix} = \mathcal{M}_0(a,d) \begin{pmatrix} \tilde{\tilde{E}}_z^{(m)}(d) \\ \tilde{\tilde{H}}_\theta^{(m)}(d) \end{pmatrix}, \tag{B.45}$$

where

$$\mathcal{M}_0(a,d) = \begin{pmatrix} A_0^{(m)} & C_0^{(m)} \\ I_0^{(m)} & K_0^{(m)} \end{pmatrix}, \tag{B.46}$$

which are given by

$$A_0^{(m)} = \mu_m a(I_0'(\mu_m d)K_0(\mu_m a) - I_0(\mu_m a)K_0'(\mu_m d)), \tag{B.47}$$

$$C_0^{(m)} = -\frac{jZ_0\mu_m^2 a(I_0(\mu_m a)K_0(\mu_m d) - I_0(\mu_m d)K_0(\mu_m a))}{k\tilde{\epsilon}}, \tag{B.48}$$

$$I_0^{(m)} = \frac{jka\tilde{\epsilon}(I_0'(\mu_m d)K_0'(\mu_m a) - I_0'(\mu_m a)K_0'(\mu_m d))}{Z_0}, \tag{B.49}$$

and

$$K_0^{(m)} = \mu_m a(I_0'(\mu_m a)K_0(\mu_m a) - I_0(\mu_m a)K_0'(\mu_m a)). \tag{B.50}$$

Especially when $m = 0$, they are rewritten as

$$A_0^{(0)} = -\frac{\pi\kappa_{cer} d(Y_1(\kappa_{cer} d)J_0(\kappa_{cer} a) - J_1(\kappa_{cer} d)Y_0(\kappa_{cer} a))}{2}, \tag{B.51}$$

$$C_0^{(0)} = j\frac{\pi\kappa_{cer}^2 aZ_0(-Y_0(\kappa_{cer} d)J_0(\kappa_{cer} a) + J_0(\kappa_{cer} d)Y_0(\kappa_{cer} a))}{2\tilde{\epsilon}k}, \tag{B.52}$$

$$I_0^{(0)} = -\frac{j\tilde{\epsilon}k\pi a(Y_1(\kappa_{cer} d)J_1(\kappa_{cer} a) - J_1(\kappa_{cer} d)Y_1(\kappa_{cer} a))}{2Z_0}, \tag{B.53}$$

$$K_0^{(0)} = -\frac{\pi\kappa_{cer} d(-Y_0(\kappa_{cer} d)J_1(\kappa_{cer} a) + J_0(\kappa_{cer} d)Y_1(\kappa_{cer} a))}{2}, \tag{B.54}$$

where

$$\kappa_{cer} = \sqrt{k^2\tilde{\epsilon}}. \tag{B.55}$$

Appendix C. Expansion formulae for the Bessel and Neumann functions

The Bessel and Neumann functions are related as follows:

$$\frac{1}{J_0(z\frac{\rho_w}{d})(Y_0(z) - \frac{Y_0(z\frac{\rho_w}{d})}{J_0(z\frac{\rho_w}{d})}J_0(z))} = \frac{\pi}{2\log[\frac{d}{\rho_w}]} - \sum_{l=1}^{\infty}\left[1 - \frac{i_l^2}{(-z^2 + i_l^2)}\right]\frac{\pi J_0(i_l)J_0(i_l\frac{\rho_w}{d})}{(J_0^2(i_l) - J_0^2(i_l\frac{\rho_w}{d}))}, \tag{C.1}$$

$$-\frac{(Y_1(z) - \frac{Y_0(z\frac{\rho_w}{d})}{J_0(z\frac{\rho_w}{d})}J_1(z))}{z(Y_0(z) - \frac{Y_0(z\frac{\rho_w}{d})}{J_0(z\frac{\rho_w}{d})}J_0(z))} = \frac{1}{z^2\log[\frac{d}{\rho_w}]} + \sum_{i=1}^{\infty}\frac{2J_0^2(i_l\frac{\rho_w}{d})}{(i_l^2 - z^2)(J_0^2(i_l) - J_0^2(i_l\frac{\rho_w}{d}))}, \tag{C.2}$$

where i_l is the lth zero of

$$Y_0(i_l) - \frac{Y_0(i_l\frac{\rho_w}{d})}{J_0(i_l\frac{\rho_w}{d})}J_0(i_l) = 0. \tag{C.3}$$

We prove the above formulae as follows. Consider the following form of the integral

$$\frac{1}{2\pi j}\oint \frac{d\zeta}{(\zeta^2-z^2)\zeta J_0(\zeta\frac{\rho_w}{d})(Y_0(\zeta)-\frac{Y_0(\zeta\frac{\rho_w}{d})}{J_0(\zeta\frac{\rho_w}{d})}J_0(\zeta))}, \tag{C.4}$$

where $-\pi < arg(\zeta) < \pi$. The integrand has no cut, because the following relationship is satisfied:

$$Y_0(\zeta e^{jm\pi})-\frac{Y_0(\zeta\frac{\rho_w}{d}e^{jm\pi})}{J_0(\zeta\frac{\rho_w}{d}e^{jm\pi})}J_0(\zeta e^{jm\pi}) = Y_0(\zeta)-\frac{Y_0(\zeta\frac{\rho_w}{d})}{J_0(\zeta\frac{\rho_w}{d})}J_0(\zeta). \tag{C.5}$$

Thus, the integration contour is selected as a circle around the origin with infinite radius. Because the summation of all contributions to the integral from the poles tends to zero, Eq. (C.4) is rewritten as

$$-\frac{1}{z^2J_0(z\frac{\rho_w}{d})(Y_0(z)-\frac{Y_0(z\frac{\rho_w}{d})}{J_0(z\frac{\rho_w}{d})}J_0(z))} = -\frac{\pi}{z^2 2\log[\frac{d}{\rho_w}]}-\sum_{l=1}^{\infty}\frac{\pi J_0(i_l)J_0(i_l\frac{\rho_w}{d})}{(-z^2+i_l^2)(J_0^2(i_l)-J_0^2(i_l\frac{\rho_w}{d}))}, \tag{C.6}$$

which is identical to Eq. (C.1) (see Eq. (B.12)), where we use Eq. (C.3).

Similarly, consider the following form of the integral:

$$\frac{1}{2\pi j}\oint \frac{d\zeta(Y_1(\zeta)-\frac{Y_0(\zeta\frac{\rho_w}{d})}{J_0(\zeta\frac{\rho_w}{d})}J_1(\zeta))}{(\zeta^2-z^2)(Y_0(\zeta)-\frac{Y_0(\zeta\frac{\rho_w}{d})}{J_0(\zeta\frac{\rho_w}{d})}J_0(\zeta))}. \tag{C.7}$$

By utilizing the relationship

$$Y_1(\zeta e^{jm\pi})-\frac{Y_0(\zeta e^{jm\pi})}{J_0(\zeta e^{jm\pi})}J_1(\zeta e^{jm\pi}) = e^{-jm\pi}[Y_1(\zeta)-\frac{Y_0(\zeta)}{J_0(\zeta)}J_1(\zeta)], \tag{C.8}$$

we finally obtain

$$-\frac{(Y_1(z)-\frac{Y_0(z\frac{\rho_w}{d})}{J_0(z\frac{\rho_w}{d})}J_1(z))}{z(Y_0(z)-\frac{Y_0(z\frac{\rho_w}{d})}{J_0(z\frac{\rho_w}{d})}J_0(z))} = \frac{1}{z^2\log[\frac{d}{\rho_w}]}+\sum_{i=1}^{\infty}\frac{2J_0^2(i_l\frac{\rho_w}{d})}{(i_l^2-z^2)(J_0^2(i_l)-J_0^2(i_l\frac{\rho_w}{d}))}. \tag{C.9}$$

Appendix D. Longitudinal resistive-wall impedance by a beam

General solutions (especially E_z, H_θ) for $m = 0$ are expressed as

$$E_z = E_z^S + A(k)e^{-jkz}I_0\left(\bar{k}\rho\right), \tag{D.1}$$

$$H_\theta = H_\theta^S + \frac{j\beta\gamma}{Z_0}A(k)e^{-jkz}I_1\left(\bar{k}\rho\right), \tag{D.2}$$

in the vacuum chamber ($0 < \rho < d$) and

$$E_z = e^{-jkz}C_1(k)(I_0(\nu_1\rho)-\frac{I_0(\nu_1 a)}{K_0(\nu_1 a)}K_0(\nu_1\rho)), \tag{D.3}$$

$$H_\theta = \frac{(\sigma_c+j\omega\epsilon_0)}{\nu_1}e^{-jkz}C_1(k)(I_1(\nu_1\rho)+\frac{I_0(\nu_1 a)}{K_0(\nu_1 a)}K_1(\nu_1\rho)), \tag{D.4}$$

in the resistive material with the conductivity σ_c ($d < \rho < a$), where $A(k)$ and $C_1(k)$ are arbitrary coefficients, $\bar{k} = k/\gamma$ and $\nu_1 = \sqrt{k^2/\gamma^2 + jk\beta Z_0\sigma_c}$.

The coefficients are determined by the boundary condition as

$$-A(k)I_0\left(\bar{k}d\right) + C_1(k)(I_0\left(\nu_1 d\right) - \frac{I_0\left(\nu_1 a\right)}{K_0\left(\nu_1 a\right)}K_0\left(\nu_1 d\right)) = \frac{jkcZ_0 I_0(\bar{k}r_b)}{2\pi\gamma^2}K_0(\bar{k}d), \tag{D.5}$$

$$-\frac{j\beta\gamma}{Z_0}I_1\left(\bar{k}d\right)A(k) + \frac{(\sigma_c + j\omega\epsilon_0)}{\nu_1}(I_1\left(\nu_1 d\right) + \frac{I_0\left(\nu_1 a\right)}{K_0\left(\nu_1 a\right)}K_1\left(\nu_1 d\right))C_1(k) = \frac{\beta kcI_0(\bar{k}r_b)}{2\pi\gamma}K_1(\bar{k}d). \tag{D.6}$$

The coupling impedance Z_L is defined as the average of the longitudinal electric field (normalized by the beam current) over the beam cross-section. For a pencil beam, we obtain

$$Z_L = -\frac{jZ_0 k}{2\beta\pi}\left(\frac{K_0(\bar{k}d)}{\gamma^2 I_0(\bar{k}d)} + \frac{2\pi A(k)}{jkcZ_0}\right)g, \tag{D.7}$$

where g is the ring circumference.

For a relativistic beam, we obtain

$$\frac{Z_L}{g} = \frac{\left(K_0\left(\nu a\right)I_0\left(\nu d\right) - I_0\left(\nu a\right)K_0\left(\nu d\right)\right)\frac{1}{2\pi d}}{-\frac{(\sigma_c + j\omega\epsilon_0)(K_0(\nu a)I_1(\nu d) + I_0(\nu a)K_1(\nu d))}{\nu} + \frac{jkd(K_0(\nu a)I_0(\nu d) - I_0(\nu a)K_0(\nu d))}{2Z_0}}, \tag{D.8}$$

where $\nu = \sqrt{jkZ_0\sigma_c}$.

References

[1] http://home.cern/topics/large-hadron-collider
[2] http://www.esrf.eu/
[3] A. W. Chao, *Physics of Collective Beam Instabilities in High Energy Accelerators* (Wiley, New York, 1993).
[4] Y. Shobuda and Y. H. Chin, Prog. Theor. Exp. Phys. **2017**, 123G01 (2017).
[5] https://www.psi.ch/sls/
[6] https://www.psi.ch/useroffice/accelerator-status
[7] E. Koukovini Platia, High frequency effects of impedances and coatings in the CLIC damping rings, *Ph.D. Thesis* 6661, École Polytechnique Fédérale de Lausanne (2015).
[8] E. Koukovini-Platia, G. Rumolo, and C. Zannini, Phys. Rev. Accel. Beams **20**, 011002 (2017).
[9] M. D. Janezic and J.A. Jargon IEEE Microw. Guid. Wave Lett., **9**, 76 (1999).
[10] F. Caspers, Bench measurements, in *Handbook of Accelerator Physics and Engineering*, eds. A. W. Chao and M. Tigner (World Scientific, Singapore, 1999), Chap. 7, p. 570.
[11] Y. Shobuda, Y. H. Chin, and K. Takata, Phys. Rev. ST Accel. Beams **17**, 091001 (2014).
[12] L. S. Walling, D. E. McMurry, D. V. Neuffer, and H. A. Thiessen, Nucl. Instrum. Meth. A **281**, 433 (1989).
[13] H. Hahn, Phys. Rev. ST Accel. Beams **3**, 122001 (2000).
[14] A. Burov and V. Lebedev, Proc. 8th European Particle Accelerator Conf., p. 1455 (2002). (Available at: http://accelconf.web.cern.ch/AccelConf/e02/papers/WEPRI022.pdf.)
[15] Y. Shobuda and K. Yokoya, Phys. Rev. E **66**, 056501 (2002).
[16] E. Métral, *Transverse resistive wall impedance from very low to very high frequencies*, CERN-AB-2005-084 (2005). (Available at: https://cds.cern.ch/record/895805?ln=ja.)
[17] E. Métral, B. Zotter, and B. Salvant, Proc. PAC07, p. 4216 (2007). (Available at: http://accelconf.web.cern.ch/AccelConf/p07/papers/FRPMN075.pdf.)
[18] N. Mounet and E. Métral, Proc. IPAC2010, p. 2039 (2010).(Available at: http://accelconf.web.cern.ch/AccelConf/IPAC10/papers/tupd050.pdf.)
[19] K. Yokoya, Part. Accel. **41**, 221 (1993).
[20] R. Gluckstern and B. Zotter, Phys. Rev. ST Accel. Beams **4**, 024402 (2001).

[21] A. M. Al-Khateeb, R. W. Hasse, O. Boine-Frankenheim, W. M. Daqa, and I. Hofmann, Phys. Rev. ST Accel. Beams **10**, 064401 (2007).
[22] F. Roncarolo, F. Caspers, T. Kroyer, E. Métral, N. Mounet, B. Salvant, and B. Zotter, Phys. Rev. ST Accel. Beams **12**, 084401 (2009).
[23] M. Ivanyan, E. Laziev, V. Tsakanov, A. Vardanyan, S. Heifets, and A. Tsakanian, Phys. Rev. ST Accel. Beams, **11**, 084001 (2008).
[24] M. Ivanyan, A. Grigoryan, V. Tsakanov, and M. Dehler, Proc. PAC09, p.4616 (2009). (Available at: https://accelconf.web.cern.ch/accelconf/pac2009/papers/fr5rfp038.pdf.)
[25] K. M. Hock and A. Wolski, Nucl. Instrum. Meth. A **657**, 94 (2011).
[26] E. Koukovini-Platia, G. Rumolo, and C. Zannini, Proc. IPAC2014, p. 2384 (2014). (Available at: http://accelconf.web.cern.ch/AccelConf/IPAC2014/papers/wepme050.pdf.)
[27] N. Mounet, *ImpedanceWake2D*. (Available at: http://impedance.web.cern.ch/impedance/Codes/ImpedanceWake2D/user_manual_todate.txt.)
[28] R. E. Collin, *Foundations for Microwave Engineering* (McGraw-Hill, New York, 1992).
[29] F. W. Olver, Bessel functions of integer order, in *Handbook of Mathematical Functions: With Formulas, Graphs, and Mathematical Tables*, eds. M. Abramowitz and I. A. Stegum (Dover, New York, 1970), Chap. 9, p. 355.
[30] CST Studio Suite. (Available at: https://www.cst.com.)
[31] N. W. Ashcroft and N. D. Mermin, *Solid State Physics* (Saunders, Philadelphia, PA, 1976).
[32] M. Dressel and M. Scheffler, Ann. Phys. **15**, 535 (2006).
[33] Y. Shobuda, Y. H. Chin, and K. Takata, Phys. Rev. ST Accel. Beams **10**, 044403 (2007).
[34] S. A. Schelkunoff, Bell Syst. Tech. J. **17**, 17 (1938).
[35] B. W. Zotter and S. A. Kheifets, *Impedances and Wakes in High-Energy Particle Accelerators* (World Scientific, Singapore, 1998).
[36] H. Xin, L. Wang, and D. Carnahan, IEEE MTT-S Int. Microwave Symp., p. 1181 (2007).
[37] Y. Shobuda and Y. H. Chin, Phys. Rev. Accel. Beams **19**, 094201 (2016).
[38] K. Bane and G. Stupakov, Proc. PAC05, p. 3390 (2005). (Available at: http://epaper.kek.jp/p05/papers/rppe057.pdf.)
[39] G. V. Stupakov, AIP Conf. Proc. **581**, 141 (2001).
[40] M. G. Blaber, M. D. Arnold, and M. J. Ford, J. Phys. Chem. C **113**, 3041 (2009).
[41] Y. Shobuda, Y. H. Chin, and K. Takata, Phys. Rev. ST Accel. Beams **12**, 094401 (2009).
[42] Y. H. Chin, *User's guide for ABCI version 9.4 (azimuthal beam cavity interaction) and introducing the ABCI Windows application package*, KEK Report No. 2005-06 (2005). (Available at: http://abci.kek.jp/abci.htm.)
[43] G. Stupakov, R. E. Thomson, D. Walz, and R. Carr, Phys. Rev. ST Accel. Beams **2**, 060701 (1999).
[44] U. Ellenberger et al., J. Phys.: Conf. Ser. **425**, 072005 (2013).
[45] J. Scifo et al., arXiv:1801.03823 [physics.acc-ph] [Search INSPIRE].
[46] J. R. Brews, IEEE Trans. Electron Devices **33**, 1356 (1986).
[47] R. L. Gluckstern and R. Li, Part. Accel. **29**, 159 (1990).